Galaxies, Cosmology and Gravitation:
On Escaping Galaxy Clusters in Accelerating Universes

by

Alejo Stark

A dissertation submitted in partial fulfillment
of the requirements for the degree of
Doctor of Philosophy
(Astronomy and Astrophysics)
in The University of Michigan
2018

Doctoral Committee:

Associate Professor Christopher J. Miller, Chair
Professor August E. Evrard
Associate Professor Dragan Huterer
Professor Mario Mateo

Alejo Stark
alejo@umich.edu
ORCID iD: 0000-0001-5783-2797

Dedicated to the Kinross prison rebels.
Paraphrasing comrade George Jackson,
"...even while I am *escaping*, I will be looking for a weapon...."

Por una ciencia que sea de abajo y a la izquierda.

ACKNOWLEDGMENTS

How do we even begin to acknowledge the myriad of relations that made, in one way or another, this dissertation possible? For one, we can begin by affirming that even though this work bears the name of a single author, the processes and determinations that made this work possible will always exceed the single name, that is, will always escape the loneliness of individual authorship–of bourgeois individualism. We can also affirm that to acknowledge and take account of all the relations that made this work possible is an impossible task. Nonetheless, we accept this impossible task, knowing fully well that we will fail in the attempt.

Primero, antes que nada, antes que todo, gracias a mi madre, Patricia. Gracias por haber tenido el deseo y la convicción de parirme y traerme a este mundo, a pesar de todas las dificultades que eso implicaba. Gracias por tu garra, gracias por enseñarme a luchar, gracias por tu amor infinito. Sé que este doctorado, esta tesis, nos ha separado y parece ser que esa distancia, con cada día que pasa, se expande a un paso acelerado. Espero poder devolverte, mamá, todo el amor y cariño que me brindás. Gracias a mi padre, Carlos. Gracias pá por tu elección de criarme, de acogerme cuando solo tenia un par de años de edad, gracias por tu vision y tu coraje de hacer el "viaje" (ese "borrón y cuenta nueva" como le solías decir), gracias por irme a buscar a Hialeah High School y al community college con empanadas, gracias por tu amor y compromiso incondicional. Gracias a mi Abuela Lidia por seguir luchando por su salud y por siempre mantenerme bien alimentado. Gracias a mi Abuelo tanguero (y ahora "meme-ero," por todo lo que mandás por WhatsApp), el "último romántico", Oscar, por haberme inculcado mi primera pasión en la vida, la de los aviones, que algo tiene que ver con la física. Gracias a Jorge por tu apoyo en todos estos años, por los viajes, los partidos de pool, y los lindos momentos que a veces se nos olvidan. La mudanza y los primeros meses en Michigan no hubiesen sido posible sin tu ayuda. Gracias a mi familia en su conjunto por todo su esfuerzo para que de algúna manera ó otra siempre tenga un plato de comida y techo bajo el que dormir, es decir, por crear una situación que me deje enfocarme casi exclusivamente en mis estudios. Nada de esto hubiese sido posible sin ustedes. Gracias. Los quiero mucho.

Needless to say, this dissertation would have never been possible without the support of friends and loved ones that made Ann Arbor a livable place for me.

Gracias a la familia Pous-Bowler (Fede, Iris, Jenny, y Luna) por dejarme ser parte de su familia. Gracias por "la tertulia," y las infinitas reuniones en esa casa de "el arbol" que funciona como cierto anclaje de la memoria para tantos de nosotros. Gracias por cultivar ese hogar que ha dado lugar a tantas fiestas de cumpleaños, a la visita de Ruben, y también a la celebración de la defensa de esta misma tesis. Gracias por crear y mantener ese espacio de encuentro. Jenny, desde el primer día que te conocí, entendí que tu pasión era la mía. Que tu búsqueda continúa, nace de una incomodidad, de una inquietud de lo que significa vivir en un mundo que no es vivible. Gracias por seguir pensando y luchando para que otro mundo sea posible. Fede, gracias por dejarme que te taladre tantas veces el oído, de política, de "rollos académicos", de lo que sea, y por tus precisiones al respecto. Gracias también por hacer posible de acercarme a pensar lo carcelario también en el campo de estudios culturales latinoamericanos. Gracias a los dos por escucharme y apoyarme en tantas decisiones claves. En tratar de volcar en estas páginas lo que siento por ustedes se me escapan las palabras. Me siento como Luna cuando trata de explicar algo pero las palabras no le llegan–el tema es que sus expresiones no son traducibles. Lo único que les quiero decir es: gracias.

Gracias al Fede por haberme presentado al pibe de Villa Adelina, el gran Matias Be-ve-ri-no-tti. Gracias hermano, por haberme bancado tantas (tantas) veces, en tantas situaciones distintas, en diferentes registros emocionales e intelectuales (ó como se le diga). Como por ejemplo, en esa noche en el hospital (cuando deliraba que me querían operar el lóbulo frontal y que era un complot del estado), en grupos de lectura, ó en tantas charlas de café. Gracias por estar siempre dispuesto a eso, a escuchar, charlar, y apoyarme (aguantarme?) en tantas instancias que no puedo elaborar en estas paginas, pero que llevo en mi corazón. Gracias por los viajes (por los que pasaron y por los que vendrán), gracias por los mates, y las (casi) infinitas carcajadas en la que parecíamos dos pelotudos riendose por una boludez. No será Messi pero tiene un aire.... Desde ya te pido perdón, porque en estos agradecimientos seguro encontrarás a más de una falta de ortografía. Es imposhiiible! En fin, gracias. Te quiero mucho chabón!

Gracias al Matias conocí al Sergio. Gracias Sergio por creer que un astrofísico marxiano que estudió Africana Studies tiene algo que contribuir al pensamiento (es decir, gracias por no hacerle caso al Heidegger en pensar que los físicos no piensan, que la wea es pura onticidad, digamos). Fuera de joda, gracias por tu “advising,” por tu generosidad de lectura, de conversa, de compartir un cafe ó lo que sea. Como sabes, es la razón por la cual decidí quedarme acá. Gracias también por los pases de gol. Tanto dentro y afuera de la cancha. Por muchos goles más. Gracias también por elegir a la Marlene como compañera de vida, que siempre es tan cariñosa y acogedora conmigo.

Gracias a Juan Leal, que siempre con calma está ahí para aportar un consejo y palabra de apoyo. Gracias por llevarme tantas veces a jugar a la pelota sin pedir nada a cambio. Gracias por escucharme y tambien aceptar mi perdón cuando nos hemos desencontrado. Gracias por las mudanzas y el compañerismo que muchas veces se pasa por alto. Espero poder apoyarte en estos meses que vienen. Se que va a estar todo bien.

Gracias a Claudio, Raisa, la Sofi, y el Pablito, que en estos últimos meses también me han hecho, junto al Juan, algo así como un tío más. Gracias por apoyarme y entenderme en estos últimos pasos que di para terminar esta tesis, por las lecciones de historia del Partido Comunista Chileno y todas las otras weas po weon. Por muchas weas mas!

I cannot think of the work of this dissertation without thinking of the love and compañerismo of Eduarda Lira da Silva Nabuco de Araujo (“Duda”) who accompanied me in my move to Michigan and was always there in the often rocky first years of graduate student life. Thank you for listening to me and supporting me in critical times. Thank you for sacrificing so much in making the many trips to and fro to spend a few days together. Thank you for taking care of me in Rio when it felt like the whole world came crushing down on us. Thank you for getting me that strawberry milkshake and those chicken fingers during finals. I know that this dissertation at times took a toll on our relationship, and for that, I can only say that I am sorry. I still have much to learn from your cleverness and constant sense of joy of life. Lastly, you should know that I tried including the “plot” you made (with Microsoft Paint) but I just couldn’t figure out where. Um grande beijo para você.

This dissertation would have not been possible without the continued support and love of my brothers, friends, and comrades in the Department of Astronomy, Bryan Terrazas and Tom Rice. Simply put, I would not have finished, nor started, this dissertation without you all. Bryan, thank you for your passion and initiative in taking us to NSBP, thank you for meticulously reading and correcting (time and again) my NSF GFRP application. Thank you Tom for the late night homework sessions (and the subsequent 7am morning breakfasts) and thank you for teaching me how to code. Thank you both for your friendship and being there through moments of pain, sorrow, frustration, and celebration.

The work of this dissertation would also not have been possible without the love and support of friend-comrades that made the Ann Arbor bubble explode, and in so doing, allowed me to breathe and live beyond the often circuitous and self-referential entanglements of university "life."

First of all, thank you to the friend-comrades of Ann Arbor Alliance for Black Lives/Ann Arbor to Ferguson, especially Austin, Brian, Dan, Donald, Jackie, Hedieh, Mar, Mary, Rebecca and Sasha for continuing to struggle to make the world anew. That is, for continuing to struggle for a world in which Black Lives Matter, for a world in which Aura Rain Rosser could have lived her life, could have been free to do as she willed–to paint, to cook, and to love. Thank you to Rebecca, for your insistence on and your continued fight for life, all of which is a source of inspiration for me and others. Thank you to Mar for being there for my defense and supporting me on those last steps – it means more than I am able to express in these pages. Thank you to Donald, for your continued insistence on "a concrete analysis of a concrete situation," and on being "history makers, not history followers." Last but not least, Jackie, thank you for your extraordinary commitment and devotion to the struggle, which is an example for many of us, though we oftentimes fall short.

Thanks to my comrades of Rustbelt Abolition Radio, "a. Maria", David Langstaff (flankflaf), Kaif Syed (with some news you may have missed), Nelson Andres Stockdill (aka "NAS"), and our newest member (!) Catalina Rios. We often forget that transformation entails an act of creation, an act of affirmation. Thank you to all of you for attempting to make that happen every month. As insignificant as this may seem at times, remember that a single spark can start a prairie fire. I would like to especially thank Ayana for having the vision and creativity of getting this whole thing started in the "right" moment. Thank you also for your tremendous support and unwavering commitment in ensuring my well-being in the past year, and for even reading (and providing corrections for) parts of the introduction of this dissertation. Your energy and independence of thought and action is an example to follow–even if sometimes its hard for you to realize this about yourself.

Thank you to my friends, comrades, and colleagues of the marxisms collective, who for at least two years have agreed to meet in the impossible-to-find rooms of West Hall to discuss Marx's Capital, the Zapatista's Hydra book, or whatever we were reading at the time. These meetings with you all radically transformed the space of the astronomy department for me, and in more ways than one, made that space more livable, and therefore, also made this dissertation possible. Thank you to Hedieh, Peter Linebaugh, Peter Solenberger, Dan Nemser, John Ware, Jackie, Ayana, Gavin, Sarika, and the many many people that are/have been part of the marxisms collective. Thanks, especially, to Brian Whitener for being one of the people who made this group possible. Thank you Brian for continuously making spaces, opening "cracks" as the zapatista metaphor goes, in the walls of the university to make struggle–both within it and beyond it–possible. Thank you for all your advice and support throughout this thesis and in my transition. Thank you also to Gavin for willing to co-coordinate the marxisms collective with me–thank you for your advise, friendship, advocacy and support in getting the group started and going in these past few months as I wrapped up this dissertation.

Thanks to my Lansing comrades, Duncan, Zoe, Peter, and Steph, for cheering me on in these past few months, as well as for coming all the way to Ann Arbor for my defense, and of course, for the soccer games (when are we playing again?). Thank you also to the many friend-comrades in Michigan (and beyond) who have supported me, in one way or another, throughout this process: Amanda Armstrong-Price, Liat Ben-Moshe, Katy Clark, Jeff Clark, Julian Francis-Park, Eduardo García, Tony Khalid, Lenora Knowles, Leo Kosloff, Momo, Verónica López, Linda Quiquivix, Bruno Renero-Hannan, Matias Saidel, Soiber, and many others who will have to excuse me for not getting a chance of mentioning them in these pages.

Lastly, I would like to thank a friend-comrade who, mostly from afar, inspired many of us to struggle within the boundaries of that thing we call the astro/physics community. Thank you, Chanda, for your advise in a critical juncture of my life and your continued support from afar. Your brilliance and persistence is an inspiration to us all.

Also, thanks to my Michigan Abolition and Prisoner Solidarity comrades. You know who you are. Remember that, as this dissertation shows, it is easier to escape in an accelerating universe–and that the universe is already accelerating. Fire to the prisons. Freedom for the prisoners.

I would have never gotten to Michigan, much less written this thesis, without all the mentors and teachers that accompanied me throughout my years as a joint Physics and Africana Studies major at Brown University. In particular, I would like to thank my physics mentor and advisor, Savvas Koushiappas, for teaching me the basics of astrophysics and cosmology both inside and outside of the classroom, as well as for all his patience and support in my first steps as a "researcher." Thank you to Ian Dell'Antonio for teaching me general relativity, also for trusting me enough to become a grader for the class a year (or so) after, and for answering my questions about the so called “twin paradox.” I also owe my first steps as a researcher to the tutelage and support of Michael Gladders at the University of Chicago–thank you Mike for your encouragement and continued support. Last, but not least, I would like to thank the entire Africana Studies department at Brown – in particular, Anthony Bogues, Anani Dzidzienyo, Keisha-Khan Perry, Francoise Hamlin, and Corey D.B. Walker– for inviting me in and creating a “home away from home” during my time at Brown, which was critical during my time there. In particular, I would like to thank the mentorship of Anani Dzidzienyo. Thank you, Anani, for your help in rough times and for the charlas in the cold Providence winters, muito obrigado. Last but not least, thank you Keisha-Khan for your advocacy and support both at Brown and beyond. Thank you, Keisha-Khan, for being not only a brilliant scholar but also an extraordinary mentor.

Before Brown University, in a little room in Little Havana, I often met with other undocumented youth as we plotted how we were going to change the world. I would not have gotten to Michigan, nor Brown, without their support throughout my two years in Miami Dade community college (MDC). Much gratitude to all my hermanos, hermanas, hermanoas, of FLIC/SWER: Subhash Kateel, Gaby Pacheco, Jose Luis Marantes, Isabel Sousa-Rodriguez, Felipe Sousa-Rodriguez, Carlos Roa, and Maria Rodriguez, and so many others who made it possible for so many undocumented youth, like myself, to afford out-of-state tuition and complete my studies at MDC. Our struggle to melt the petrifying ice of deportation and detention, which continues to this day, also made it possible for myself and so many others to live and organize without the paralyzing fear of retribution. Last, but certainly not least, none of this would have been possible without the love, support and commitment of Meagan Patrick. Thank you Meggie. These few words cannot do justice to your commitment.

Before Miami Dade College, I learned the basics of physics at Hialeah High School. I owe much to my first physics teachers– Hiram Lopez and Jose Fernandez– who taught me the fundamentals of physics in class, after school, and during lunch–in a high school whose bathrooms, more often than not, lacked both toilet papers and soap.

Thank you, also, to the many of you in my “new department” for supporting me in this transition and trusting that I had something to contribute to that thing we call “the humanities”: Gavin Arnall, Desiree Gerner, George Hoffmann, Cristina Moreiras-Menor, Daniel Nemser, Ana Sabau, Gustavo Verdesio, Sergio Villalobos-Ruminott, and Gareth Williams.

In the Department of Astronomy, I would like to thank the administrative team for your help throughout these years– especially to Brian Cox for making sure I was signed up for my classes every semester and ensuring that my labor was paid for. I would also like to specially thank two faculty members, Eric Bell and Emily Rauscher, who have who have, more than once, lend me their ear in the hallways of West Hall or in cafes, to grapple with the challenges and limitations of transforming that bubble we call the University of Michigan.

Finally, I would also like to extend my gratitude to my thesis committee– Christopher J. Miller, August E. Evrard, Dragan Huterer and Mario Mateo–who critically assessed my work and provided vital feedback that made the investigations here presented both more legible and more robust. Thank you Dragan, for the cosmology class and for teaching me (with quite a conviction too) the wonders of the Fisher matrix formalism. Thank you Mario, for your skepticism and critical assessment of established paradigms. Thank you, Gus, for your seminal research that in many ways created the conditions of possibility for this work. Last but definitely not least, I would like to thank my advisor and committee chair, Christopher J. Miller, for supporting me both in my research process (which, more often that not, caused problems and did not necessarily offer many solutions) both within the Department of Astronomy and beyond it. Thank you, Chris, for supporting my class at the Women's Huron Valley Prison, and for helping me get to Trieste, Chiapas, Vancouver, and even to Bologna. Thank you also for supporting my transition even when it didn't seem to make any sense at all. Needless to say, I will very much miss the many (many) conversations (arguments?) that we have had over the years over the mysteries of the universe (or rather, of our models of these mysteries) that are now materialized in the chapters of this thesis. Know that I always took the intensity of our arguments as an expression of passion–a quality often lacking in the halls of "the academy."

Lastly, I would like to acknowledge that the labor process of this thesis was conducted when the author was student at the University of Michigan in the years 2013 - 2017 and that it was financially supported by both the Rackham Merit Fellowship and the National Science Foundation Graduate Research Fellowship. We also want to acknowledge that the work presented in this thesis has been peer-reviewed and published as four independent papers in both *The Astrophysical Journal* and the *Physical Review*. In particular, Chapter 2 is based on Stark et al. (2016). Chapter 4 is based on Stark et al. (2017). Chapter 5 is based on Stark et al. (2016). Chapter 1 is loosely based on all of the aforementioned publications as well as Miller et al. (2016). The only exception is Chapter 3 which is based on work submitted to *The Astrophysical*

Journal that is currently under review (Stark et al. (2017)).

TABLE OF CONTENTS

DEDICATION iii

ACKNOWLEDGMENTS iv

LIST OF FIGURES xv

LIST OF TABLES xxiv

LIST OF APPENDICES xxv

ABSTRACT xxvi

CHAPTER

I. Introduction 1

1.1 Our dynamic cosmos 1
1.2 Gravitation 3
1.2.1 General relativity 3
1.2.2 Chameleon $f(R)$ gravity 4
1.3 Cosmology 6
1.3.1 The Friedmann equations 6
1.3.2 Definitions of cosmological theoretical observables . 8
1.3.3 The concordant cosmological model 11
1.4 Galaxy clusters 13
1.4.1 Weak lensing mass profiles and galactic dynamics . 13
1.4.2 Galaxy cluster phase spaces and the escape velocity edge 15
1.5 Overview of this work 19

II. Escaping a galaxy cluster in an accelerating universe 22

2.1 Introduction 22
2.2 Theoretical expectations 24

2.2.1 Derivation of the escape velocity profile of a galaxy cluster in an accelerating universe 25
2.2.2 Potential-density pair 26
2.2.3 Comparing theoretical escape velocity profiles with and without the cosmological terms 28
2.3 Theoretical Observables 28
2.4 Data 30
2.4.1 Synthetic data 30
2.4.2 Archival data: weak lensing masses and galaxy redshifts 31
2.5 Testing our theoretical expectations 33
2.5.1 Projection effects 33
2.5.2 Inferring the anisotropy parameter 34
2.6 Systematics 39
2.6.1 Escape velocity edge 42
2.6.2 Weak lensing masses 42
2.6.3 Mass-concentration relation 43
2.6.4 Cosmological parameters 43
2.7 Discussion 44
2.8 Summary 45

III. Cluster escape velocity profiles and the velocity anisotropy profile 47

3.1 Introduction 47
3.2 Data 49
3.2.1 N-body simulations 49
3.2.2 Archival data 50
3.3 Theoretical Observables 52
3.3.1 Galaxy line-of-sight velocity dispersion profiles . . . 52
3.3.2 Galaxy cluster mass profiles 54
3.4 Deriving velocity anisotropy profiles 55
3.5 Results 61
3.5.1 Synthetic data results 61
3.5.2 Archival data cluster results 63
3.6 Discussion and Summary 63

IV. Cluster escape velocity profiles as a cosmological probe . . . 70

4.1 Introduction 70
4.2 Theoretical observable 71
4.2.1 Cluster parameters 73
4.2.2 Cosmological parameters 75
4.3 Fisher matrix 81
4.3.1 Formalism 81

4.3.2 F_{ij} matrix 82
4.3.3 F_{prior} matrix 86
4.4 Constraint Forecasts 89
4.4.1 Constant equation of state w 90
4.4.2 w_0 and w_a 90
4.4.3 non-flat universe, Ω_M and Ω_Λ 94
4.5 Observational strategies 94
4.5.1 Redshift range 96
4.5.2 Reducing Systematics and Stacked Clusters 99
4.6 Comparison to other probes and joint constraints 101
4.7 Summary 105

V. Cluster escape velocity profiles as a probe of Chameleon gravity 106

5.1 Introduction 106
5.2 Theoretical expectations 107
5.2.1 Hu-Sawicki $f(R)$ gravity 107
5.2.2 Gravitational potential 108
5.2.3 Escaping a galaxy cluster in an accelerating universe 109
5.3 N-body simulations 110
5.4 Probing gravity 111
5.5 Systematics 113
5.5.1 Stacked cluster ensembles 116
5.5.2 DESI Bright Galaxy Sample forecast 118
5.6 Statistical Constraints on $f(R)$ gravity 120
5.7 Summary 122

VI. Openings 123

6.1 The cosmology and redshift dependent v_{esc} 123
6.2 Probing modified theories of gravity: redshift dependence and radius 124
6.3 To stack or not to stack? 125
6.4 Toward a global galaxy cluster velocity anisotropy 126
6.5 Something always escapes 126

APPENDICES 128

BIBLIOGRAPHY 144

LIST OF FIGURES

Figure

1.1 Density profile (left panel) and escape velocity profiles (middle and right panel) for a single simulated cluster from the Millenium Simulation (Springel et al., 2005a) with mass $M_{200} = 6.3 \times 10^{14} \mathrm{M}_{\odot}$ and radius $r_{200} = 1.34$ Mpc for three potential-density pairs: the Einasto, Gamma and NFW profiles (Eqs. 1.34-1.36a). Note that the escape velocity profiles shown in the middle panel for all three models is the one integrated to infinity (Eq. 1.37). In contrast, the escape velocity profiles shown in the right-most panel is the escape velocity profile integrated out to the equivalence radius (Eq. 1.39). 17

1.2 The fractional difference between the theoretical model of the escape velocity profiles derived from Eq. 1.39 and the simulation escape velocity edges for the potential-density Poisson pair. The bands represent the scatter of the 100 cluster-sized halos in the Millenium Simulation. The median of the 100 halos is shown with a solid line and the error bars are determined from boot-strap re-sampling of the median. The dark grey band encompasses 90% of the individual halo profiles and the light grey band the 67%. 18

2.1 Escape velocity profiles for a single cluster of fixed mass using equations 2.5 and 2.7 for four different escape velocity profile models ($v_{esc}(r)$). Note that while we change Ω_M we keep $h = 0.7$ for a fiducial flat ΛCDM cosmology. We note the significant difference between the Einasto qH^2 theoretical expectations for three different flat ΛCDM cosmologies with differing matter density parameters ($\Omega_M = 0.01, 0.3, 0.6$, denoted by dashed, solid, and dashed dotted lines respectively) and the "Einasto" theoretical expectation which does not include a cosmological term (denoted by dotted line) given by $v_{esc}(r) = \sqrt{-2\Psi(r)}$ (and using equation 2.7). Note that increasing Ω_M raises the escape velocity at all radii. Going in the opposite direction, we notice that as our universe becomes more and more dominated by Λ it will in principle be easier for galaxies to escape clusters. Secondly, we note that as Ω_M increases we recover the non-cosmological escape velocity (dotted line). Note also, as implied by equation 2.5, that the Einasto qH^2 profiles all eventually reach some radius (the equivalence radius "r_{eq}") at which the escape velocity is zero. 29

2.2 The unprojected (stars) and projected (circles) weighted average ratio between the escape velocity edge and the theoretically expected escape velocity profiles with the Einasto qH^2 model for a single set of 20 synthetic clusters from the Henriques et al. (2012) light cone. The error is the 1σ error on the averaged ratio assuming a uniform 25% mass scatter on the virial mass of each cluster and a 5% scatter on the escape velocity edge. The unprojected ratios are projected after calculating the most likely average β by comparing to the unity line (see Equation 2.15). We find this value to be well in agreement with simulation results (see figure 2.3). 35

2.3 The likelihood of the average anisotropy parameter (β) as inferred from ten sets of 20 clusters in the synthetic Henriques et al. (2012) light-cone data. The gray band represents the 1σ variation on the likelihood of the ten sets. We cross-correlated the Henriques et al. (2012) light-cone data with the 3-dimensional velocity data from Guo et al. (2011a) to calculate, analytically, the average beta for the sample via Eq. 2.14 to attain: $\beta = 0.275 \pm 0.062$ at the 95% confidence level (black line dashed and dotted). The red lines represent the β profile with 2σ error (dash and dotted) for 1000 clusters in the Millennium sample calculated also with Eq. 2.14 by Iannuzzi & Dolag (2012). Only by including the cosmological-dependent term on our theoretical formulation can we recover the true β with accuracy and to high precision. Compare the red lines to the purple band which utilizes the Einasto potential for the analytic profile of the escape velocity profile without the cosmological term. We conclude, then, that we can rule out the analytic profile without the cosmological term at the 6.3σ level. Note that the Iannuzzi & Dolag (2012) band is the error on the mean as calculated from a bootstrap algorithm also between $0.3 < r/r_{200} < 1$. Lastly, as mentioned in the text, we assume a uniform 25% mass scatter on M_{200} for all clusters and a 5% error on the escape velocity edge. The cosmology utilized for our analytic profiles is the same as what was utilized to make the simulations (see section 2.4). 37
2.4 The unprojected and projected weighted average ratios between the escape velocity edge and the theoretically expected escape velocity profiles for the set of archival data set of 20 clusters. Note the similarity between this sample and the synthetic sample Fig. 2.2. Given that we are using the particular weak lensing mass errors for each cluster (rather than a uniform mass scatter of 25% as in Fig. 2.2) the overall error on the average ratio is larger. 40
2.5 The likelihood of the average β as inferred from the set of 20 archival clusters (black line). We also re-plot the likelihood band (gray) from the ten sets of 20 synthetic clusters as well as the results from numerical simulations from Iannuzzi & Dolag (2012) (as in Fig. 2.3). With just 20 clusters we can recover the velocity anisotropy only if the escape velocity profile is described by an Einasto density field with an additional cosmological term (as in equation 2.5). 41

3.1 *Top panel:* Difference between the measured line-of-sight velocity dispersion profile (σ_{los}) and the tangential velocity dispersion (σ_t) for the 100 synthetic clusters from cosmological N-body simulations. The horizontal dashed lines represent the 1σ error on our measurement of σ_{los}, ~ 50 km s^{-1}. *Bottom panel:* Difference between the "true" β measured via Eq. 3.1 and the "line-of-sight" β (Eq. 3.24). See text for details. The black line shows the median (50th percentile) and the dark (light) gray bands represents the 68th (90th) percentile. The small bias in σ_{los} leads to a systematic bias in the inferred β. . 60

3.2 Results for the sample of 100 synthetic clusters from cosmological N-body simulations. *Top panel:* median (black line) with 68% and 90% percentile bands (dark and light gray, respectively). β is calculated with Equation 3.21 (see Section 3.4) and the resulting median is $\beta \sim 0.1$. *Bottom panel:* The difference, ($\beta - \beta^{true}$), between β as calculated with our approach and the "true" anisotropy parameter (β^{true}) calculated directly from the simulated galaxies via Eq. 3.1. The dark and light gray bands represent the same percentiles as those shown in the top panel. Note that the fractional difference between the "true" β and our inference is about zero. 62

3.3 Resulting β profile for the 35 clusters of the archival data. The black dots are the weighted mean of each individual profile calculated with Eq. 3.21 (see Section 3.4) and the error is the 1σ uncertainty on the weighted mean. Note that each individual profile that is averaged here contains both the uncertainty in mass and line-of-sight velocity dispersion. The global value of β averaged between 0.2 and r_{200} is $\langle\beta(0.2 \leq r/r_{200} \leq 1)\rangle = 0.35 \pm 0.28$. This means that the galactic orbits are mostly radially anisotropic. The gray triangles are the result of correcting for the systematic shown in the bottom-panel of Fig. 3.1. We note that the overall effect still produces a result that lies within our 1σ error. Note that we have slightly shifted the gray triangles to higher radii simply to make the plot legible. 64

3.4 Comparison of 4 of the 35 individual β profiles with results from the literature. For all the panels, the gray band represents the 68th percentile error on β from both the uncertainty in the weak lensing mass profiles as well as the uncertainty in the line-of-sight velocity dispersion profiles. See text for details. 65

3.5 Comparison between β profiles from the literature and our work. The β calculated with Equation 3.21 (see Section 3.4) from 100 N-body simulated clusters is shown in light/dark gray bands and the β from the 35 archival data clusters is shown with black dots (same as in Fig. 3.3). In contrast to those of Fig. 3.2, the synthetic cluster results (grey bands) now take into account the uncertainty in the line-of-sight velocities as well as consider only physical results ($\beta \leq 1$). In red diamonds, we show the results of the median and 1σ error on β calculated for 16 clusters by Host et al. (2009). In the red vertical line, we show the range calculated by Wojtak & Łokas (2010) for their low concentration sample (about 30 clusters) at the virial radius. Lastly, the red stars are the averaged β for 1000 simulated clusters by Iannuzzi & Dolag (2012). Note that the 1σ error for the Iannuzzi & Dolag (2012) result is too small to show. 67

4.1 Behavior of the equivalent radius (r_{eq}) as a function of redshift (z) for a cluster with mass $M_{200} = 4 \times 10^{14} M_\odot$ for three values of Ω_M in a flat ΛCDM universe and $h = 0.7$. At the transition redshift for each given cosmology, the radius shoots up to infinity. Note how r_{eq} becomes more and more sensitive to Ω_M at higher z. 77

4.2 Redshift evolution of the deceleration parameter in a flat universe with fixed $\Omega_M = 0.3$ and $h = 0.7$. Notice the divergence of values of q at low redshifts when the equation of state parameter is varied. . . 78

4.3 Using a single cluster with mass $M_{200} = 4 \times 10^{14} M_\odot$ at $z = 0$, we show the fractional difference between the escape velocity profile of a flat wCDM universe with dark energy equation of state $w = -1$ and two other dark energy models (quintessence in the solid line and phantom dark energy in the dotted line). More specifically, $\Delta v_{esc}(r, z)/v_{esc}(r, z) = [v_{esc}(w)/v_{esc}(w = -1)] - 1$. Quintessence therefore acts similarly to increasing the dark matter density. That is, it increases the escape velocity profile relative to the Λ case (see Fig. 1 of Stark et al. (2016)). On the other hand, the phantom dark energy suppresses the escape velocity profile relative to the Λ case. Lastly, we highlight that the fractional difference increases with radius in both cases. 79

4.4 Sensitivity of the observable $v_{esc}(r, z)$ to cosmology. The partial derivatives of the escape velocity profile are calculated numerically at 100 different redshifts (z) with respect to the various cosmological parameters for our fiducial cluster. The specific redshift of a given profile can be identified through the color bar on the right-hand side of the figure. In all cases, the information grows (i.e. the observable becomes more sensitive) the farther out we go radially. Some parameters are most sensitive at higher redshifts (Ω_M, Ω_Λ and h) while others are more sensitive at lower redshifts (w). Note that beyond the transition redshift for our fiducial cosmology, the derivatives with respect to all parameters reach a limit, as implied by Section 4.2 . . 83

4.5 68% and 95% confidence constraints for the flat wCDM case after marginalizing over all other parameters. We use $N_{clus} = 1000$ (100) clusters as shown in red (black) uniformly distributed in the range $0 \leq z \leq 0.8$. The priors on the Einasto parameters assume a uniform 80% weak lensing mass scatter for all redshifts (see Table 4.1). The 1σ errors are $\sigma_{\Omega_M} = 0.007(0.025)$ and $\sigma_w = 0.138(0.431)$ for $N_{clus} = 1000$ (100). 91
4.6 68% and 95% contours for the dynamic dark energy case using the CPL parametrization of dark energy marginalized over Ω_M and h as well as the other cluster parameters. More specifically, we use $N_{clus} = 1000$ clusters uniformly distributed between $0 \leq z_c \leq 0.8$ with 80% (40%) weak lensing mass scatter in the turquoise (purple) contour which yields: $\sigma_{w_0} = 0.139(0.124)$ and $\sigma_{w_a} = 0.968(0.857)$. With $N_{clus} = 100$ uniformly distributed in the same redshift range as before and with 40% mass scatter but now adding a prior on the Hubble constant from Riess et al. (2016) we attain, $\sigma_{w_0} = 0.191$ and $\sigma_{w_a} = 2.712$ (pink contours). 93
4.7 68% and 95% contours for the non-flat ΛCDM case for $N_{clus} = 100$ uniformly distributed between $0 \leq z \leq 0.8$ with 80% mass error. Applying a prior on the Hubble constant h from Riess et al. (2016) ($\sigma_h = 0.0174$) allows us to break the degeneracy and thereby significantly improve our constraints. The marginalized 1σ constraints derived from the green (black) contours are $\sigma_{\Omega_M} = 0.101(0.185)$and $\sigma_{\Omega_\Lambda} = 0.197(0.428)$. 95
4.8 Inverse area of the Ω_M - w covariance matrix after marginalizing over all other parameters as a function of maximum (left panel) and minimum (right panel) redshift used. We assume a uniform redshift distribution of clusters in the range $0 \leq z \leq z_{max}$ (left panel) and $z_{min} \leq z \leq 0.8$ (right panel). Each calculation of the inverse area assumes a fixed number of clusters, $N_{clus} = 100$. Note that $\Omega_M - w$ constraints can be improved by reducing the mass uncertainty from 80% (solid line) to 40% (dashed line), in which case the contour area decreases by a factor of ∼1.3. The constraint can be further increased by utilizing stacked weak lensing mass estimates and stacked phase spaces, and this yields a 10% mass scatter and $\sigma_\beta = 0.02$ (see Table 4.1), decreasing the contour area by a factor of ∼ 7.5 (compare solid to dotted lines). The left panel also illustrates that using clusters beyond the transition redshift leads to a gradual loss of cosmological information. While a tighter constraint can be achieved by incorporating higher redshift clusters, the right panel demonstrates that we still need low redshift clusters to achieve the tightest constraints on w. See Fig. 4.9. We conclude that as broad as possible redshift range of clusters be used (e.g. $0 \leq z \lesssim 0.8$). 96

4.9 Marginalized Ω_M and w uncertainties for the flat wCDM case with 100 clusters distributed in the range $z_{min} \leq z \leq 0.8$. Note that as the minimum redshift z_{min} increases a factor of ~1.7 improvement in σ_{Ω_M} is attained (see solid line, bottom panel). The trade-off is a significant loss of information on the dark energy equation of state parameter w at high redshift (top panel). These effects combine to make the inverse area plot as a function z_{min} relatively flat (see right-hand side panel in Fig. 4.8). Note also that a maximum factor of ~ 4 improvement in the uncertainty of these parameters may be achieved if cluster parameter uncertainties are reduced (compare solid to dotted lines). 97

4.10 68% and 95% contours for the dynamic dark energy case using the CPL parametrization of dark energy marginalized over Ω_M and h as well as the other cluster parameters. The blue contours are reproduced from the latest JLA SNIa constraints of Betoule et al. (2014). The green contours are reproduced from the Planck 2015 TT likelihood of Planck Collaboration et al. (2016a). In red are constraints derived from a sample of $N_{clus} = 1000$ clusters uniformly distributed in the redshift range $0 \leq z \leq 0.8$, after applying a conservative 80% mass scatter prior (same as the turquoise contours of Fig. 4.6). In all cases, no prior assumptions about the Hubble constant are used. . . 102

4.11 68% and 95% contours for the flat wCDM case. The red contours are derived the same as what is shown in Fig. 4.5. The blue contours are reproduced from the latest JLA SNIa constraints shown in Betoule et al. (2014). The green contours are reproduced from the Planck 2015 TT likelihood Planck Collaboration et al. (2016a). In all cases, no prior assumptions about the Hubble constant are used. 103

5.1 The $z = 0$ gravitational potential ratio between high and low mass bins of synthetic galaxy clusters for the GR (black), the FR5 (*left*) parametrization of $f(R)$ gravity (green), and the FR6 (*right*) parametrization (red). The points are the average of the square of the observed escape velocities for each bin in radius and mass. The errors are 1σ on the mean from boot-strap re-sampling. The solid lines represent the theoretical predictions using the NFW density parameter (Eqns. 5.7 - 5.9). Note the $\gtrsim 5\sigma$ level difference between the GR and FR5 ratios. The percentages denote how we separate the high and low mass bins. Note that the separation between GR and *f(R)* potential ratios increases with increasing separation in the mass bins. 111

5.2 The simulated and theoretical averaged GR and $f(R)$ gravity potential ratios for the same clusters of Figure 5.1 (top 20% and bottom 20% mass bins). We have added the theoretical prediction for $|f_{R0}| = 4 \times 10^{-6}$ gravity (yellow) and include not only the GR statistical error on the mean (black error bars) but also the 10% systematic error due to cosmic variance (black dashed lines). This figure demonstrates how we would detect and/or constrain MG. Assuming GR as our "observation," the data is contained within the black dashed bands. We can therefore ask the question: which of the three plotted models best describes the data? We conclude our probe can, including systematics, successfully discern between GR and $|f_{R0}| = 4 \times 10^{-6}$ at 1σ.Note that this result is attained with only 40 clusters (20 in each mass bin) and the potential is inferred from 3-dimensional phase space synthetic data. We reproduce this plot for a projected DESI-like data-set in Fig. 5.4. 115

5.3 The gravitational potential ratio of Fig. 5.1 (black dots with statistical error) and the gravitational ratio as inferred from an ensemble of clusters (gray line with statistical error) from the light cone data of Henriques et al. (2012). The high and low mass cluster ensembles are made up of 5 different ensembles each with 10 clusters that include 500 galaxies each. The error bars are 1σ error on the mean from boot-strap re-sampling. This nearly flat transfer function incorporates numerous observational systematics when going from 3D to realistic observational data. 117

5.4 The projected gravitational potential ratio for a DESI-like galaxy cluster sample (black dots and bootstrap error on the mean) as inferred from synthetic galaxy clusters from the light cone provided by Henriques et al. (2012). Compared to Fig.5.2 (where the ratio is inferred from a 3D phase space) we see that projection significantly increases the statistical error. The DESI sample is significantly larger as it contains 9.6 times many more clusters and so the systematic error is significantly reduced (286 low mass clusters and 96 high mass clusters). From this we can determine which gravitational theory best matches the "observation." To visualize this, we plot both the GR theoretical prediction (black line) and two $f(R)$ theoretical predictions (orange-red and yellow). We conclude that our probe can differentiate between GR and $|\overline{f_{R0}}| = 4 \times 10^{-6}$ (2×10^{-6}) at $> 5\sigma$ $(> 2\sigma)$. 121

C.1 Structure of the $N_{dim} \times N_{dim}$ (see Eq. (4.19)) F_{ij} matrix. The "cosmo-cosmo" submatrix (orange) has dimensions $N_{cosmo} \times N_{cosmo}$ and contains the information solely of the cosmological parameters and their inverse covariances. The "cosmo-cluster" submatrices (red) lie along the first row and column of the F_{ij} matrix and are composed of the cross-correlated information between cluster parameters and cosmological parameters. Note that along the first column these submatrices have dimension $N_{clus} \times N_{cosmo}$, and along the first row, the matrices are transposed and therefore have dimensions $N_{cosmo} \times N_{clus}$. Lastly, the "cluster-cluster" submatrices (green) lie along the diagonal and have dimensions $N_{clus} \times N_{clus}$. Note that zeros populate the off-diagonal spaces given that there is no correlation between clusters, so that the derivatives cancel out. 138

D.1 Marginalized likelihood of the inferred mass of our fiducial cluster ($M_{200} = 4 \times 10^{14} M_\odot$) from the weak lensing surface density shear profile $\Sigma(r)$. The total uncertainty in the inferred mass increases by a factor of ~ 2 if no prior on the cosmological parameters is introduced; however, a reasonable prior on the Hubble parameter h from Riess et al. (2016) recovers most of the lost information on M_{200}. 142

LIST OF TABLES

Table

2.1 List of Galaxy Clusters and References 32

3.1 List of Galaxy Clusters and References 51

4.1 Cluster parameter uncertainties that make up the F_{prior} matrix used in the various cases considered in the Constraint Forecasts section as well as the error on the edge $\sigma_{v_{esc}}$ that makes up the F_{ij} matrix. Note that in principle there is no covariance between β and the three other parameters, but we simply change the uncertainty on β for the other cases with reduced weak lensing mass scatter. Furthermore, as explained in the text, we use the weak lensing (WL) mass percent error on M_{200} as shorthand to describe uncertainties in all three Einasto parameters. In the last row we tabulate the uncertainties in the three Einasto parameters after applying a prior on h from from Riess et al. (2016). All other cluster parameter uncertainties listed contain both statistical error as inferred from weak lensing (WL) analyses and systematic error from cosmology as explained in the "Prior information" section and Appendix D. 87

LIST OF APPENDICES

Appendix

A. Derivation of qH^2 for various cosmological cases 129

B. Fisher matrix derivation 134

C. Fisher matrix structure 137

D. Weak lensing mass covariance with cosmology 141

ABSTRACT

The late-time cosmic acceleration of the universe is one of most profound mysteries of physical cosmology. What is at stake with this discovery is the following: either our universe is composed of some exotic "dark energy" which drives the dynamics of the acceleration or our general relativistic theory of gravity must be radically transformed. Clusters of galaxies, some of the largest gravitationally-bound objects in our universe containing hundreds of galaxies, have been fruitful sites from which to study the consequences of our cosmological models and the gravitational theory from which these models are derived. In this work, we derive and test a novel model that takes into account the effects of our accelerating universe at the scale of galaxy clusters. More specifically, the theoretical observable we work with in this dissertation is the escape velocity profile of galaxy clusters. Our model implies that in an accelerating universe, the escape velocity profile of galaxy clusters is lower than what is expected from a universe that is not accelerating. Put differently, if the universe is accelerating, galaxies confined to their clusters have an easier time escaping them. However, testing the implications of this model is difficult given that observations can only allow us to infer the projected escape velocity profiles. Here, we study how the observed profiles can be de-projected via a function that depends on the cluster velocity anisotropy profile. To that end, we also develop a novel approach to derive cluster velocity anisotropy profiles with joint dynamical and weak lensing data. We further show that our cosmology-dependent model of the escape velocity profile can be utilized to constrain cosmological models. In particular, with the Fisher matrix formalism we show that our theoretical observable has the capacity to set competitive constraints on relativistic cosmological models of the accelerating universe in the near future. Lastly, we drop the presupposition that general relativity is the only way to describe gravitational phenomena and develop a novel probe of gravity that utilizes the sensitivity of our theoretical observable to changes in the gravitational potential.

CHAPTER I

Introduction

1.1 Our dynamic cosmos

Sooner or later, everything changes. In this sense, everything has a history. The study of the history of the universe as a whole we call "cosmology." More specifically, we are referring to the physical theory of cosmology as elaborated in the revolutionary years of the early 20th century that is derived from the current dominant physical theory of space-time and gravitation–the theory of general relativity (GR). As is perhaps expected from this formulation that emphasizes historicity, cosmology was not always this way and it could also perhaps be otherwise.

As radical as the theory of relativity was in proposing a dynamical relationship between the curvature of a 4-dimensional manifold called "space-time" and the mass-energy that inhabits it, one of the first cosmological models derived from this theory implied that the cosmos was static and not dynamic. One of these "steady state cosmologies" was proposed by Albert Einstein in 1917, and today it is remembered for Einstein's introduction of the famous "cosmological constant" that counteracted the expanding tendencies of the universe implied by the equations of general relativity.

Today, the dominant paradigm posits that the universe is not only not static, but rather quite dynamical, in fact it is expanding, and it is expanding at a faster rate than before.[1] Our universe is accelerating. In fact, the concordance cosmological model stipulates that a dark energy (some mysterious substance) prevents the gravitational pull of the dark matter (another mysterious substance) from making the universe collapse on itself. In brief, our current (moving) picture of the world is one in which the universe is a dynamic totality evolving from small perturbations in the fabric of space-

---

[1] We emphasize that this apprehension of the cosmos as changing and dynamical is in continuity with the "Copernican revolution," which was not only a revolution in that it de-centered the Earth from the universe, but perhaps more radically, proposed that the Earth itself was moving.

time about 13.8 billion years ago which have, over time, gravitationally collapsed in a hierarchical manner (less massive objects collapse first) to form the structures we see today – from the smallest systems of binary stars, to galaxies containing billions of stars, to the hundreds of galaxies that inhabit gravitationally-bound galaxy clusters. This is the history of our dynamic cosmos as narrated by physical cosmology condensed into one sentence. This cosmology implies that the universe today is mostly composed of dark energy (69%), followed by dark matter (31%), and the rest (less than 1% of the total mass-energy "budget" of the universe) is visible matter (the stuff that stars–as well as the world we are most familiar with–is made of).

In several ways, we can say that this thesis is a small contribution in continuing to come to terms with the evolving consequences of our dynamical cosmos. As the title of this work implies, these pages weave together the concrete materiality of galaxies as their dynamics relate to both: our cosmological models, as well the theories of gravity from which these models are derived.

In particular, in what follows we propose a mathematical model that describes the ways in which cosmological phenomena, such as the acceleration of the universe at the largest of scales, is intimately related to the dynamics of clustered galaxies. More specifically, the theoretical observable we work with throughout this work is the *escape velocity profile* of galaxy clusters.[2] In the chapters that follow, we describe how in a universe that is accelerating – either due to dark energy, or extensions (or modifications) to general relativity– the capacity for galaxies confined in clusters to escape is reduced. Which is to say, in a universe in which the accelerated expansion dominates the dynamics of the cosmos, clustered galaxies can more easily become unbounded from their clusters. The mathematical model that encapsulates this statement is developed at the end of this introduction and in Chapter II. We also propose a novel way of constraining cosmology models in Chapter IV that relies on an accurate and precise measurement of the galaxy cluster anisotropy parameter β. We develop a new approach to derive β profiles in Chapter III. Lastly, using this same theoretical observable, we develop an independent way to study extensions to general relativistic gravity, such as Chameleon $f(R)$ gravity, in Chapter V.

Before we go into the small contribution this work makes to our apprehension of the dynamical cosmos, in this chapter we (1) briefly sketch the ways in which workers in the field astrophysics have characterized galaxy clusters, (2) provide an overview of our dominant cosmological model, and (3) review the foundations of the dominant

---

[2] Throughout this work we use "theoretical observable" to emphasize that all observables are always already theory-laden.

theory of space-time and gravitation–the theory of general relativity–as well as recent attempts to modify it.

1.2 Gravitation

1.2.1 General relativity

The theory of relativity is a theory of space and time as well as a theory of gravity. In contrast to Newtonian gravity, which posits that gravitation is an attractive force acting a distance between massive objects, general relativity posits that gravity is not a force, but rather, it is the very curvature of space-time itself. Put differently, general relativity implies that massive bodies themselves shape the arena in which they move (that is, space-time). To put it briefly, we can encapsulate the relativistic conception of gravitation in the following way: matter tells space-time how to curve, and space-time tells matter how to move.[3] Mathematically, this statement can be translated into the Einstein Field Equations (EFE) of general relativity,

$$R_{\mu\nu} - \frac{1}{2}Rg_{\mu\nu} = 8\pi G T_{\mu\nu}, \tag{1.1}$$

where we have set the speed of light c to 1 and G is the usual Newtonian gravitational coupling constant. The left-hand side (LHS) of the EFE embodies the geometry of space-time, encapsulated in some mathematical objects of differential geometry: the Ricci tensor $R_{\mu\nu}$, the Ricci scalar R, and the metric tensor $g_{\mu\nu}$. This LHS can in turn be expressed in terms of the "Einstein tensor",

$$G_{\mu\nu} \equiv R_{\mu\nu} - \frac{1}{2}Rg_{\mu\nu}. \tag{1.2}$$

The right-hand side (RHS) of the EFE takes into account the matter-energy in a given local region of space-time–as expressed in the stress-energy tensor $T_{\mu\nu}$. The indices used in defining the tensors, μ and ν, refer to the indices of a chosen coordinate frame.

From this very brief introduction, we may already intuit how a theory of cosmology may be derived from the EFE. The evolution of the left-hand side of the EFE (the changing and evolving geometry of space-time) is related to the evolution and transformation of the matter-energy in that space-time (the RHS of the EFE). As such, if we can trace the evolution of matter across time, we can reconstruct the history of

---

[3] This beautifully simple formulation can be found in the monumental book *Gravitation* by C.W. Misner, K.S. Thorne, and J.A. Wheeler.

space across cosmic epochs. We develop how this done in Section 1.3 below.

While at first sight the EFE may appear opaque, to develop some intuition of its innerworkings we can relate Eq. 1.1 to the more familiar Poisson equation for the gravitational field. In particular, we can think of Poisson's equation as the equation that the EFE's aim to generalize. The Poisson equation is given by,

$$\nabla^2\Phi = 4\pi G\rho, \tag{1.3}$$

where Φ is the Newtonian gravitational potential and ρ is a density field describing the matter density profile, say, of galaxy clusters.[4] In the language of relativity, the LHS of Eq. 1.3 encapsulates the "curvature" of the gravitational potential field Φ (which plays the role of the metric in the EFE) seeded by the distribution of matter ρ (which is part of the stress-energy tensor in the EFE).

This association between the Poisson equation and the EFE helps us motivate how the gravitational potential of galaxy clusters Φ and consequently the escape velocity of clusters (v_{esc}) is intimately related to cosmology, since,

$$v_{esc}^2 = -2\Phi. \tag{1.4}$$

Before we describe this intimate relation between the escape velocity profile of clusters and cosmology, we take a brief detour away from our dominant theory of gravity to briefly overview alternative theories of gravity that extend general relativity.

1.2.2 Chameleon $f(R)$ gravity

In the introductory paragraph to this chapter we briefly mentioned that a variety of high precision observations all seem to indicate that our universe is currently undergoing accelerated expansion.[5] The most popular model that is consistent with these observations deploys the framework of GR with an additional cosmological constant (Λ) that induces cosmic acceleration at late times.[6] Whether this term is introduced in the LHS or RHS of Eq. 1.1 is a source of debate with deep theoretical implications (Durrer & Maartens, 2008). However, the theoretical framework of this concordant cosmological model, GR, is still poorly tested on megaparsec scales. This has given

---

[4] For a more thorough elaboration of this informal argument to derive and motivate the EFE, which follows the intuition of Einstein, see Ch. 4 of S. Carroll (2003). *Space-time and Geometry: An Introduction to General Relativity.*

[5] See Weinberg et al. (2013) for an excellent overview of these observations.

[6] "Late times" is used in cosmology to differentiate this phenomena from the acceleration of the early universe stipulated by the various inflationary models in the fractions of a second after the so called "Big Bang."

way for the proliferation of both novel ways of testing GR as well as gravitational theories that modify GR in cosmological scales (Joyce et al., 2015; Koyama, 2016).

Therefore, the main theoretical thrust behind models of modified gravity (MG) is that while we know GR and its weak-field limit (Newtonian gravity) work exquisitely well at the scales of binary pulsars and the solar system, we should be cautious when extrapolating out to much larger (i.e. cosmological) scales. For this reason, models of MG that successfully reproduce late time cosmic acceleration on large scales must also recover the predictions made by GR on small scales.

To accomplish this, modified theories of gravity implement *screening mechanisms* that attenuate the effect of additional forces in high density regions. One such mechanism is the *Chameleon mechanism* whereby the additional fifth force active in low density regions is screened in regions of high density by shortening the range of interaction of the field (Khoury & Weltman, 2004a,b). A more general approach utilizes Effective Field Theory (EFT) of cosmic acceleration (Creminelli et al., 2009; Bloomfield et al., 2013), where recent theoretical advances have shown that there exists a large model space that recovers an accelerated expansion on large scales, while reducing to Newtonian gravity on the small scales in linear theory (Lombriser & Taylor, 2015).

Thus, there is a need for well-defined observational tests which can distinguish the many models. Chapter V of this work provides such a test for the scale of galaxy clusters. Without going into further detail about what is presented in Chapter V, we now simply want to highlight how the EFE change in the case of a Chameleon $f(R)$ gravity model presented in Hu & Sawicki (2007). In the case of Chameleon $f(R)$ gravity, Eq. 1.1 now becomes,

$$R_{\mu\nu} - \frac{1}{2}Rg_{\mu\nu} + f_R R_{\mu\nu} - \left(\frac{f}{2} - \Box f_R\right)g_{\mu\nu} - \nabla_\mu \nabla_\nu f_R = 8\pi G T_{\mu\nu}, \tag{1.5}$$

where the additional degree of freedom f_R creates an additional fifth force which can be expressed in terms of a "modified Poisson equation." For small field values ($f_R << 1$, again, with $c = 1$), and neglecting the time derivatives of Eq. 1.5, the modified Poisson equation is given by (Hu & Sawicki, 2007),

$$\nabla^2\left(\Phi + \frac{1}{2}\delta f_R\right) = 4\pi G\rho. \tag{1.6}$$

As such, we immediately notice that the relation between the gravitational potential (and consequently the escape velocity profile of massive objects – such as galaxy clusters) and the density profile will be affected. However, not all massive objects are affected the same way. In particular, our probe of gravity compares high mass clusters, where Chameleon effects are weak, to low mass clusters, where the effects can be strong.

Lastly, we emphasize that the screening mechanisms deployed by MG must also operate in such a way as to recover the predictions made by general relativity at the largest scales as well. For instance, these models cannot make predictions that strongly deviate from current uncertainties in cosmological observations that are based on general relativity. We describe relativistic cosmology and the concordant cosmological model next.

1.3 Cosmology

1.3.1 The Friedmann equations

The equations of contemporary relativistic cosmology can be derived from the Copernican principle in conjunction with the EFE. This principle, which can be tested, states that at large scales (that is, at the scales of hundreds of megaparsecs) the universe is the same in every direction (it's homogeneous) and has no preferred directional orientation at any point (it's isotropic).[7] However, our cosmos is dynamic. As such, we must clarify that the Copernican principle entails that the universe is *spatially* homogeneous and isotropic but it evolves with time. Geometrically, this means that the space-time metric ($g_{\mu\nu}$ in the EFE), expressed in an infinitesimal region of space-time via the interval $ds^2 = g_{\mu\nu}dx^\mu dx^\nu$, for this Copernican principle can be expressed in the following way,

$$ds^2 = -dt^2 + a^2(t)\left[\frac{dr^2}{1-kr^2} + r^2 d\Omega^2\right], \tag{1.7}$$

where the co-moving elements are expressed in terms of polar coordinates and $d\Omega^2 = d\theta^2 + \sin^2\theta d\phi^2$. This is the famous Friedmann-Lemaître-Robertson-Walker (FLRW) metric.

The scale factor $a(t)$ determines how a proper distance $d(t)$ changes the comoving distance today d_0 over time, $a(t)d_0 = d(t)$. Given this definition of the scale factor, k represents the Gaussian curvature of space today ($a(t_0) = 1$). The possible values of k encapsulate three different geometries: elliptic ($k > 0$), Euclidean ($k = 0$), or hyperbolic ($k < 0$). Using the tools of Riemannian geometry one can work out the

---

[7] The most direct and cleanest observational test of the isotropy of the universe comes from the Cosmic Microwave Background radiation which shows the universe has a single temperature of 2.7K with very small fluctuations around that mean.

Riemann tensor and the Ricci scalar with the usual Christoffel symbols from the $g_{\mu\nu}$ metric shown in the line interval above.[8] This gives us the LHS of the EFE. The diagonal elements of the Einstein tensor are,

$$\begin{aligned} G_{tt} &= \tfrac{3(k+\dot{a}^2)}{a^2}, && (1.8)\\ G_{rr} &= -\tfrac{2a\ddot{a}+\dot{a}^2+k}{1-kr^2}, && (1.9)\\ G_{\theta\theta} &= -r^2(2a\ddot{a}+\dot{a}^2+k), && (1.10)\\ G_{\phi\phi} &= -r^2\sin^2\theta(2a\ddot{a}+\dot{a}^2+k). && (1.11)\end{aligned}$$

Where the dots, as usual, denominate derivatives with respect to the zeroth element, time. For the RHS of the EFE, if the stress-energy tensor is then modeled as a perfect fluid (due to the Copernican principle) then we have,

$$T_{\mu\nu} = (\rho + p)U_\mu U_\nu + p g_{\mu\nu}, \tag{1.12}$$

where p is the pressure and ρ is the energy density of the fluid (both quantities defined in the rest frame). Given that we want the fluid's pressure to be isotropic, the normalized four-velocity four-vector for the FLRW is given by,

$$U^\mu = (1, 0, 0, 0). \tag{1.13}$$

So the elements of the stress-energy tensor for the FLRW metric using Eq. 1.12 are,

$$\begin{aligned} T_{tt} &= \rho, && (1.14)\\ T_{rr} &= p\tfrac{a^2(t)}{1-kr^2}, && (1.15)\\ T_{\theta\theta} &= pa^2(t)r^2, && (1.16)\\ T_{\phi\phi} &= pa^2(t)r^2\sin^2\theta. && (1.17)\end{aligned}$$

Putting together the RHS and the LHS of the EFE with Eq. 1.8-1.17, respectively, yields the Friedmann equations. For the "*tt*" component we get,

$$\left(\frac{\dot{a}}{a}\right)^2 = \frac{8\pi G}{3}\rho - \frac{k}{a^2}, \tag{1.18}$$

---

[8] See Chapter 8 of S. Carroll (2003). *Space-time and Geometry: An Introduction to General Relativity.*

and the acceleration equation can be derived from Eq. 1.18,

$$\frac{\ddot{a}}{a} = -\frac{4\pi G}{3}(\rho + 3p). \tag{1.19}$$

These equations, the Friedmann equations, are the fundamental equations of relativistic cosmology. We can now finally appreciate what we foreshadowed in the last section – the expansion history of the universe encapsulated in the scale factor $a(t)$ is a function of the dynamics of the matter-energy in the universe as encapsulated in the stress-energy tensor elements. We can now re-write general relativity's fundamental statement in terms of cosmology: matter-energy tells space how to expand, and space tells matter-energy how to evolve.

But how do these matter-energy densities evolve over time? What specific equation governs their evolution? A third equation can be derived by combining Eq. 1.18 and 1.19. This equation is called the continuity equation and it is given by,

$$\dot{\rho} = -3\frac{\dot{a}}{a}(p + \rho). \tag{1.20}$$

Having derived and motivated the fundamental equations of cosmology from the theory of general relativity, we now briefly go over some key definitions of cosmological functions used in contemporary cosmology and throughout this work.

1.3.2 Definitions of cosmological theoretical observables

To solve the Friedmann equations and reconstruct the expansion history of the universe it is useful to define the equation of state parameter w,

$$w = \frac{p}{\rho}. \tag{1.21}$$

Note that this equation again assumes that $c = 1$, $p = w\rho c^2$. The specific value of w depends on the species of matter-energy we are working with. For instance, the dominant model for the dark energy equation of state assumes that it is simply constant over time (the famous "cosmological constant") and at the same time creates a kind of "negative pressure," and so it is represented by the equation of state parameter $w = -1$. The second most important component of the mass-energy "budget" of our universe is the dark matter. The dominant model for this matter, "cold dark matter," implies that it is a pressureless fluid, and so its equation of state parameter is $w = 0$.

Furthermore, the continuity equation (Eq. 1.20) is quite useful in that it allows us to solve for the evolution of the energy density of whatever kind of matter-energy species with a *constant* equation of state parameter w,

$$\rho = \rho_0 a^{-3(1+w)}, \tag{1.22}$$

where the energy density of the given species today is defined by ρ_0.

But how is the scale factor a measured? Unfortunately, cosmologists cannot take the "view from nowhere" and lay down a ruler in the universe. One concrete quantity that astronomers actually measure is the redshift z of some object along a line of sight. The redshift is defined as the fractional change between the observed and the emitted wavelength λ of the given object (for instance, a galaxy),

$$z \equiv \frac{\lambda_{observed} - \lambda_{emitted}}{\lambda_{emitted}}. \tag{1.23}$$

The redshift is related to the scale factor via the definition,

$$a \equiv \frac{1}{1+z}. \tag{1.24}$$

Where the current epoch is defined to be equivalent to $a = 1$ (or $z = 0$). As such, throughout this thesis when we speak of "galaxy redshifts" and describe cosmic epochs in terms of their redshift we are referring to the aforementioned relations.

Two other key functions we will use throughout this thesis, both of which are expressions of the Friedmann equations, are the deceleration parameter q, and the Hubble parameter H,

$$q \equiv -\frac{\ddot{a}a}{\dot{a}^2}, \tag{1.25}$$

$$H \equiv \frac{\dot{a}}{a}. \tag{1.26}$$

We can also re-define both of these fundamental quantities of cosmology in terms of the density parameter Ω. This parameter is defined in terms of the critical density of the universe. Quantitatively, using the Friedmann equation (Eq. 1.18) with $k = 0$, in combination with the definition of H above (Eq. 1.26), the critical density is,

$$\rho_{crit} \equiv \frac{3}{8\pi G} H_0^2. \tag{1.27}$$

From this, the Ω parameter for a given density is defined to be,

$$\Omega \equiv \frac{\rho}{\rho_{crit}}. \tag{1.28}$$

Using this definition, in combination with Eq. 1.22 and Eq. 1.20 we can re-write the Friedmann equation (Eq. 1.18) in terms of the Ω parameters for the various matter-energy species that make up our universe,

$$H^2 = H_0^2 E^2(z) = H_0^2 \left[\Omega_M (1+z)^3 + \Omega_k (1+z)^2 + \Omega_{DE} \exp \left\{ 3 \int_0^z \frac{dz}{(1+z')} [1 + w_{DE}(z')] \right\} \right], \tag{1.29}$$

where, as before, the cold dark matter fluid is assumed to be that of the pressureless cold dark matter ($w_M = 0$), the curvature "equation of state" is worked out to be equal to $w_k = -1/3$, and we have generalized the equation of state for the dark energy to be redshift-evolving ($w_{DE}(z)$). Hence the $(1+z)^2$ and $(1+z)^3$ scalings for the curvature and dark matter terms, respectively. Often in the literature, and throughout this work as well, $w(z)$ will simply refer to the equation of state parameter of the dark energy. Lastly, note that the Ω_i values for these different matter-energy species are defined in terms of present values. For example, "Ω_M" refers to the density parameter of the dark matter at $z = 0$.

This form of the Friedmann equation is quite useful in that it allows us to calculate the comoving distance $d(z)$. From the FLRW metric we get,

$$d(z) = \int_0^z \frac{dz'}{H(z')}. \tag{1.30}$$

Furthermore, from this expression of the comoving distance we can derive the two fundamental definitions of physical distances in cosmology: the luminosity distance d_L and the angular diameter distance d_A. The former is inferred from how the measured flux of a given object with luminosity L diminishes at a distance d_L, $f = \frac{L}{4\pi d_L^2}$. The latter is inferred from how some object with proper length l changes its angular extent in the sky $\delta\theta$, $d_A \delta\theta = l$. It can be shown that these are given by, [9]

$$d_L = \left[(1+z) \frac{c H_0^{-1}}{\sqrt{\Omega_K}} \sin \left(\sqrt{\Omega_K} \int_0^z \frac{dz'}{E(z')} \right) \right], \tag{1.31}$$

$$d_A = (1+z)^2 d_L, \tag{1.32}$$

where "sin(x)" (the non-flat closed universe case) becomes "x" for the flat universe case.

---

[9] See Chapter 8 of S. Carroll (2003). *Space-time and Geometry: An Introduction to General Relativity.*

Lastly, for ease of calculation, we may also re-write the deceleration parameter (Eq. 1.25) in terms of the derivatives of the redshift-evolving Hubble parameter H of Eq. 1.29,

$$q = \frac{(1+z)}{H}\frac{dH}{dz} - 1. \tag{1.33}$$

Both Eq. 1.29 and Eq. 1.33 represent some of the most fundamental quantities of contemporary relativistic cosmology. They encapsulate, respectively, the expansion and deceleration rates of space. They will be used throughout the chapters that follow this introduction.

1.3.3 The concordant cosmological model

Having defined and specified some of the fundamental theoretical observables of cosmology that are used in this work, we now briefly review the main pieces of evidence that support our "concordant cosmological model" today – that is, the most widely accepted model of cosmology based on the theory of general relativity.

The concordant cosmological model is named the ΛCDM ("Lambda Cold Dark Matter") model because (1) it assumes that the dark energy can, to within statistical uncertainty, be taken to be a uniform fluid with a constant equation of state $w = -1$ (that is, mathematically, it takes the form of "cosmological constant" Λ that Einstein proposed a century ago but with the opposite effect) and (2) it assumes that the dark matter is "cold" (that is, pressureless) with an equation of state parameter $w = 0$. The latest results from the *Planck* satellite data analysis of the Cosmic Microwave Background (CMB) radiation, tells us that the best-fit parameters of the ΛCDM model for our cosmic epoch are: $\Omega_M = 0.31$ and $\Omega_\Lambda = 0.69$ with a Hubble constant equal to $H_0 = 67.7$ km s^{-1} Mpc^{-1} (Planck Collaboration et al., 2016b). Furthermore, utilizing the Friedmann equation, and for late-times (where the radiation density is close to nil $\Omega_R \sim 0$), we have that $\Omega_k = 1 - \Omega_M - \Omega_\Lambda$. As such, the CMB data implies our universe is flat ($\Omega_k = 0$).

The afterglow of the CMB – produced ∼380,000 years after the Big Bang and is the first time in the history of the universe in which light was able to propagate freely without being absorbed by matter– provides us the earliest and most compelling evidence of what Fred Hoyle once pejoratively called the "Big Bang" model. This model, a cornerstone of ΛCDM, stipulates that the universe emerged from a hot and dense soup of matter and it immediately underwent a period of rapid acceleration $\sim 10^{-36}$ seconds after the Big Bang (as stipulated by the theory of inflation). This rapid acceleration smoothed out the universe and made its spatial geometry flat.

According to the theory of Big Bang Nucleosynthesis (BBN), another cornerstone of ΛCDM, the matter we see today emerged minutes after this hot soup of primordial stuff cooled down enough to create the least massive atoms (such as hydrogen, helium and lithium). More massive elements, such as those that act as building blocks for organic particles (such as carbon, oxygen, and nitrogen), were created much later in the history of the universe, deep inside the first accumulations of matter that collapsed by their own weight – the stars. Theories of stellar formation and structure have shown that if the mass of these collapsed objects is high enough, their core can reach high enough temperatures to kick off thermonuclear reactions and begin to fuse hydrogen and helium to produce the heavier elements. These stars are often formed in binary systems, which make up star clusters, which in turn make up galaxies. The life and death of the stars– which act as beacons of light in the otherwise empty void that is our cosmos–are responsible for creating the diversity of cosmic objects whose dynamics and character preoccupy astronomers today: white dwarves, neutron stars, and black holes.

The ΛCDM model also stipulates that, using the aforementioned values for Ω_M and Ω_Λ with the Friedmann equation, we can calculate the "age of the universe" which is roughly given by $t_0 \sim 1/H_0$. Doing the full calculation, we find that the universe is 13.8 billion years old. A calculation like this one was one of the earliest indications in the last decades of the 20th century that the universe must contain some kind of repulsive dark energy. More specifically, astronomers calculated that the oldest star clusters of the universe – globular clusters – were older than what the cosmological theories which assumed a flat matter-only universe ($\Omega_M = 1$) stipulated the age of the universe was. As such, if the estimates of the age of these globular clusters was correct, the cosmological model of a flat universe with Ω_M could not be correct. This contradiction provided one of the first pieces of evidence that the universe was accelerating.

The history of the universe that the ΛCDM model tells is one of expanding space that went from decelerating to accelerating. More specifically, from the moments of the Big Bang, when the universe was predominately composed of radiation, its expansion made the matter-energy cool down to the point that the radiation no longer dominated the dynamics of the universe. The matter then dominated until $z \sim 0.67$ after which the deceleration parameter first became negative – that is, q went from $q > 0$ (deceleration in the era of dark matter domination) to $q < 0$ (acceleration in the current era of dark energy). This deceleration-to-acceleration transition took place about 6.2 billion years ago.

This "late-time" acceleration of the universe (named that way as to not confuse it with the earlier period of inflation) was further substantiated with two seminal papers at the turn of the 20th century that used Type Ia Supernovae (SNIa) as a "standard candle" (or rather, a standardizable candle) to probe the recession luminosity distance/redshift relation (see Eq. 1.31) expected by relativistic cosmology (Riess et al., 1998; Perlmutter et al., 1999). What these papers showed was that supernovae at high z were dimmer (farther away) than what is expected by a flat dark matter-only universe (that is, a flat universe with no dark energy). In short, the data statistically favored a model with $\Omega_M < 1$, and $\Omega_\Lambda > 0$. In terms of the present value of the acceleration parameter, Riess et al. (1998) showed that the data favored an accelerating universe ($q_0 < 0$) with high statistical confidence.

While SNIa and the CMB are two of the fundamental cosmological probes that provide strong evidence in favor of the ΛCDM model, we note that many other probes also have independently supported, within statistical and systematic error, the concordant cosmological model. In particular, galaxy clusters have also played a key role in creating this consensus around ΛCDM in our so called "golden age of cosmology."

1.4 Galaxy clusters

1.4.1 Weak lensing mass profiles and galactic dynamics

Clusters of galaxies are fruitful sites of experimentation that allow us to unravel the nature of gravitation, understand the ingredients of our cosmological models (such as dark matter and dark energy), as well as make sense of the complex astrophysical processes involved in both the evolution of galaxies and the intracluster medium (Kravtsov & Borgani, 2012a). From the standard model of structure formation, galaxy clusters are both the last and the largest structures to have formed in the history of cold dark matter halos. These halos all emerged from small seeds of density perturbations embedded in the expanding Hubble flow that have grown hierarchically since then (Gunn & Gott, 1972; Bertschinger, 1985; Fillmore & Goldreich, 1984).

Results from cosmological N-body simulations of cold dark matter halos have shown that the mass profile of clusters can be universally characterized by simple models of potential-density pairs, such as:

$$\rho(r) = \frac{\rho_0}{(r/r_0)(1+r/r_0)^2}, \tag{1.34a}$$

$$\Phi(r) = -\frac{4\pi \mathrm{G}\rho_0(r_0)^2\ln(1+r/r_0)}{r/r_0}, \tag{1.34b}$$

$$\rho(r) = \frac{(3-n)\mathrm{M}}{4\pi}\frac{r_0}{r^n}\frac{1}{(r+r_0)^{4-n}}, \tag{1.35a}$$

$$\Phi(r) = \begin{cases} \frac{\mathrm{GM}}{r_0}\ln\frac{r}{r+r_0}, \text{ for } n=2 \\ \frac{\mathrm{GM}}{r_0}\frac{-1}{2-n}\Big[1-\Big(\frac{r}{r+r_0}\Big)^{2-n}\Big], \text{ for } n\neq 2, \end{cases} \tag{1.35b}$$

$$\rho(r) = \rho_0 \mathrm{exp}\Big[-\Big(\frac{\mathrm{r}}{\mathrm{r}_0}\Big)^{1/\mathrm{n}}\Big], \tag{1.36a}$$

$$\Phi(r) = \frac{-\mathrm{GM}}{r}\Big[1-\frac{\Gamma\big(3n, \frac{r}{r_0}^{(1/n)}\big)}{\Gamma(3n)}+\frac{r}{r_0}\frac{\Gamma\big(2n, \frac{r}{r_0}^{(1/n)}\big)}{\Gamma(3n)}\Big], \tag{1.36b}$$

which represent the NFW (Navarro-Frenk-White, see Navarro et al. (1997)), Gamma (Dehnen, 1993) and Einasto (Einasto, 1965) potential-density pairs, respectively. These are referred to as density-potential pairs because they are related by the Poisson equation. For example, the potential for both of these density profiles can be derived via the integral form of the Poisson equation from their respective density ρ,

$$\Phi(r) = -4\pi G\left[\frac{1}{r}\int_0^r \rho(r')r'^2dr' + \int_r^\infty \rho(r')r'dr'\right]. \tag{1.37}$$

Observationally, these results from N-body simulations have meant that mass estimation techniques, such as those depending on weak lensing shear measurements, utilize these universal profiles to fit the data and infer cluster masses. While most of the observed cluster weak lensing mass profiles are derived using the NFW profiles (as an example, see the metacatalog compiled in (Sereno, 2015)), recent work using high resolution simulations has shown that an Einasto model, combined with a transition to a steep power-law beyond $\sim r_{200}$ (with respect to the critical density of the universe), provides the most accurate description of density profile for clusters over a wide range of accretion histories and redshifts (Diemer & Kravtsov, 2014, 2015; More et al., 2015, 2016).

Parallel to these investigations, the internal dynamics of galaxy clusters continues to be a fruitful avenue of research. For instance, in early N-body simulation investigations, the velocity dispersion of the cluster particles was identified as a simple yet powerful way to infer the gravitational potential (Evrard, 1986). As the resolution of the N-body simulations increased to include sub-halos as representative of the galaxy populations, the 3-dimensional velocity dispersion was better characterized, including the effects of sub-halo sampling bias (Evrard et al., 2008; Wu et al., 2013; Gifford et al., 2013; Gifford & Miller, 2013; Saro et al., 2013). Through the growth of large-scale spectroscopic surveys and multi-object spectroscopic instrumentation, we are evidencing the proliferation of precise dynamical data of galaxy clusters (Miller et al., 2005; Becker et al., 2007; Farahi et al., 2016; Bayliss et al., 2017)

The relation between the dynamics of clustered galaxies and the totality of the observable universe has long been a fruitful site of investigation for physical cosmology. One good example is Zwicky's seminal investigation of the dark matter, which crystallized through an analysis of the dynamics of galaxies in the Coma cluster (then referred to as "clusters of nebulae") (Zwicky, 1937). Three decades ago, also utilizing the Coma cluster as a cosmological laboratory, Shectman (1982) demonstrated that the universe's matter energy density was sub-critical – thereby pointing to the existence of some other unknown substance and demonstrating the capacity for the infall regions of galaxy clusters to be mobilized as a powerful cosmological probe. Just a few years after this, Regoes & Geller (1989a) used the Coma cluster in conjunction with three other nearby clusters to argue for the existence of "caustics" in the velocity-distance space (or "phase space") of galaxy clusters. These "caustics" trace an identifiable "edge" that would later be demonstrated to be representative of the radial escape velocity profile of galaxy clusters (Diaferio & Geller, 1997a). From this point on, the caustics would be used solely to generate mass profiles of galaxy clusters via the "caustic technique" (Diaferio, 1999; Geller et al., 2013). These dynamical cluster masses have been used to constrain cosmology through the cluster mass function (Rines et al., 2008). However, the capacity of caustic edges themselves to constrain cosmological parameters has not been pursued since the work of Regoes (1996). This is part of the work that this present thesis takes on. We explain the relation between galaxy cluster phase spaces, the escape velocity edge, and the cosmology-dependent escape velocity profile model next.

1.4.2 Galaxy cluster phase spaces and the escape velocity edge

A recent analysis by Miller et al. (2016) utilized 3-dimensional phases spaces from the Millennium simulation (Springel et al., 2005a) to demonstrate that the inferred escape velocity edge can recover the true underlying escape velocity profile of galaxy clusters to high accuracy and precision. The phase space is constructed by taking the extrema of the tracer velocities (either particles or sub-halos) in the radius-velocity phase space which in turn define a sharp surface "edge" which has been identified as the escape velocity profile. The escape velocity profile can then be modeled from the application of the Poisson equation to the measured cluster density profile as implied by the analysis presented in the previous section along with Eq. 1.4. However, what Miller et al. (2016) shows is that this model also requires cosmological information pertaining to the acceleration of space.

In particular, Miller et al. (2016) uses the integral form of the Poisson equation (Eq. 1.37) but instead of integrating to infinity integrates it out integrates out to some "equivalence radius" r_{eq} which is a function of cosmology. This equivalence radius corresponds to the point at which the outward acceleration of space equals the inward pull of the cluster's mass and is given by,

$$r_{eq}^3 = -\frac{GM}{qH^2}, \tag{1.38}$$

where M corresponds to the mass of the cluster and q and H refer to the deceleration parameter and the Hubble parameter, respectively, as we have just defined them in Section 1.3. We note that this quantity was first utilized in the context of modified theories of gravity in Stark et al. (2016) and was first derived in the context of defining bounded and unbound particles of dark matter halos in N-body cosmological simulations by Behroozi et al. (2013). We note that in contrast to Stark et al. (2016) and Miller et al. (2016), Behroozi et al. (2013) first derives this radius for a point mass.

From utilizing the equivalent radius as the integration limit, Miller et al. (2016) and Stark et al. (2016) find that the effective potential Ψ which includes the effects of the cosmological expansion is then given by,

$$-2\Psi = v_{esc}^2 = -2\Big[\Phi(r) - \Phi(r_{eq})\Big] - qH^2(r^2 - r_{eq}^2), \tag{1.39}$$

where Φ is chosen to be one the potential-density models shown above.

The phase space and escape velocity profiles for the three models just mentioned (the NFW, Gamma and Einasto potential-density pairs) is shown in Fig. 1.1 for a single simulated cluster from the Millenium Simulation (Springel et al., 2005a) with mass $M_{200} = 6.3 \times 10^{14}\ M_\odot$ and radius $r_{200} = 1.34$ Mpc (defined at 200 times the

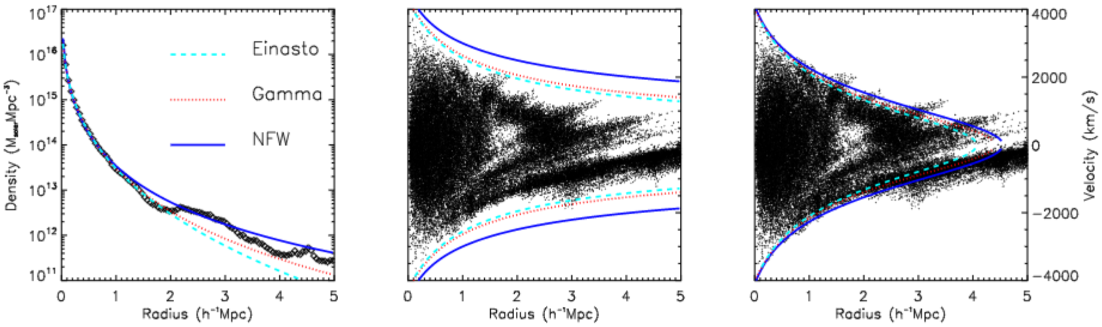

Figure 1.1: Density profile (left panel) and escape velocity profiles (middle and right panel) for a single simulated cluster from the Millenium Simulation (Springel et al., 2005a) with mass $M_{200} = 6.3 \times 10^{14} \mathrm{M}_{\odot}$ and radius $r_{200} = 1.34$ Mpc for three potential-density pairs: the Einasto, Gamma and NFW profiles (Eqs. 1.34-1.36a). Note that the escape velocity profiles shown in the middle panel for all three models is the one integrated to infinity (Eq. 1.37). In contrast, the escape velocity profiles shown in the right-most panel is the escape velocity profile integrated out to the equivalence radius (Eq. 1.39).

critical density of the universe). Note how in the right-most panel of Fig. 1.1 all of the escape velocity profiles go to zero at some radius (the equivalence radius) whereas in the middle panel the escape velocity profiles tend to overestimate the escape velocity edge traced by the phase space (black dots).

In their analysis, Miller et al. (2016) also report that the NFW model overestimates the escape velocity profiles of galaxy clusters by $\sim 10\%$ (Navarro et al., 1996, 1997). This is because the NFW density profile over-estimates the mass beyond the virial radius. Other analytic models of the density profile of dark matter halos, such as the Einasto (Einasto, 1965) and the Gamma model (Dehnen, 1993), fare much better. We note that each of these analytical representations of the density profile can be constrained to be identical within $\sim r_{200}$. Where these density profiles differ is in the outskirts–where both the Einasto and the Gamma profiles are steeper than the NFW profile. For an example of a single simulated cluster density profile fit, see the left panel of Fig. 1.1.

To further demonstrate the need to use the cosmology-dependent escape velocity profile (Eq. 1.39) to model escape velocity edge, Figure 1.2 shows the fractional difference between the measured 3-dimensional escape velocity edge and the three aforementioned models of potential-density pairs for 100 simulated clusters from the Millenium Simulation.

However, these results from Miller et al. (2016) do not take into account the complications of projection effects involved in actual observations of galaxy cluster

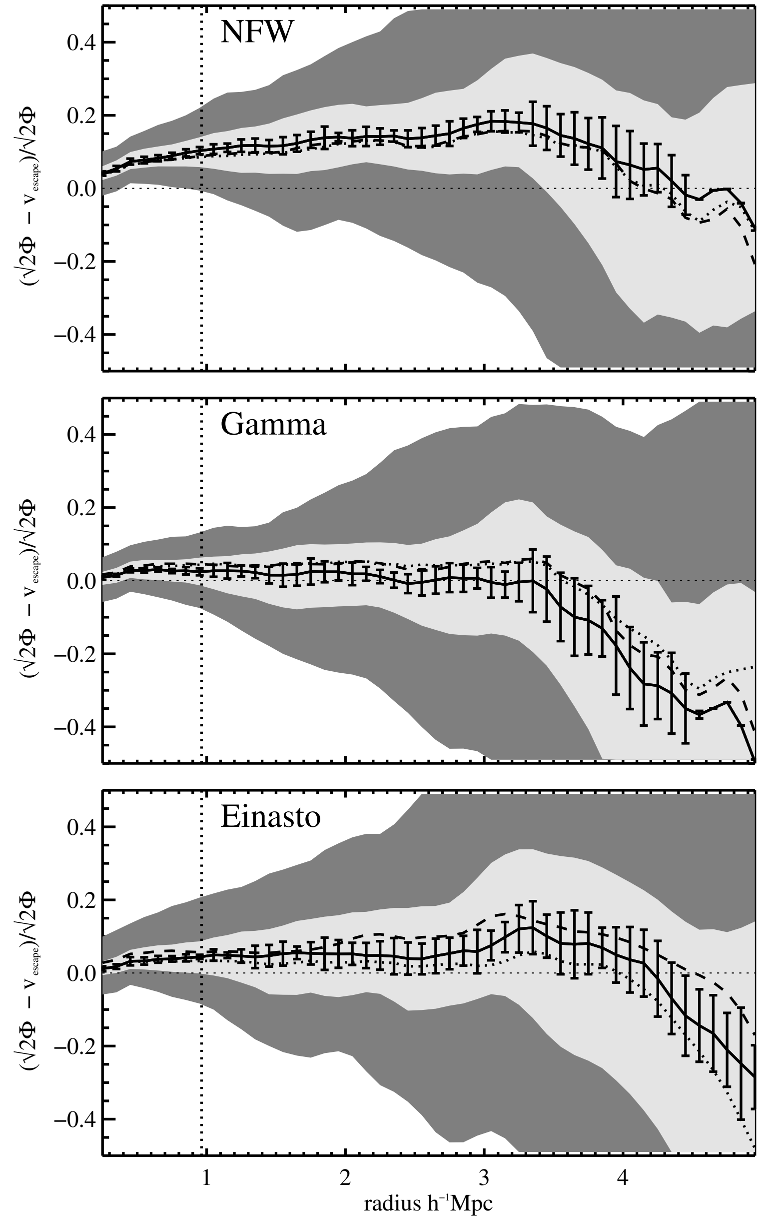

Figure 1.2: The fractional difference between the theoretical model of the escape velocity profiles derived from Eq. 1.39 and the simulation escape velocity edges for the potential-density Poisson pair. The bands represent the scatter of the 100 cluster-sized halos in the Millenium Simulation. The median of the 100 halos is shown with a solid line and the error bars are determined from boot-strap re-sampling of the median. The dark grey band encompasses 90% of the individual halo profiles and the light grey band the 67%.

phase spaces. In particular, the galaxies along a line of sight may be within the cone of observation but may not actually be located within the virial sphere of the cluster. Furthermore, the escape velocity profiles just described must be de-projected, given that what we measure with real galaxy clusters is not 3-dimensional velocities (such as the ones plotted in the phase space of Fig. 1.1), but rather, the line of sight velocities which are suppressed with respect to their 3-dimensional counterparts. In particular, through a simple geometric argument, Diaferio (1999) has shown that the 3-dimensional and projected line of sight velocity profiles are related by a factor of $g(\beta)$,

$$v_{esc,los} = v_{esc} \times \left(\sqrt{g(\beta)}\right)^{-1}, \tag{1.40}$$

where,

$$g(\beta) = \frac{3 - 2\beta(r)}{1 - \beta(r)}. \tag{1.41}$$

β is the velocity anisotropy profile and it quantifies the degree to which galactic orbits are more radial or tangential, via the ratio of the velocity dispersion in the tangential direction (σ_t) to the velocity dispersion in the radial direction (σ_r),

$$\beta(r) = 1 - \frac{\sigma_t^2}{\sigma_r^2}, \tag{1.42}$$

where $\sigma_t^2 = \frac{1}{2}\left(\sigma_\theta^2 + \sigma_\phi^2\right)$ includes both azimuthal and latitudinal velocity dispersions. The limiting cases are: radial infall ($\beta = 1$), circular motion ($\beta = -\infty$) and isotropy ($\beta = 0$). More specifically, for the radial range within r_{200}, Serra et al. (2011) has shown that $\sqrt{g(\beta(r))} \sim 1.9$ which means the projected escape velocity profiles can be lower than their 3-dimensional counterparts by that factor. Clearly, projection effects must be taken into account. Providing a novel way to derive β profiles is also part of the work that this thesis takes on. We now provide a more specific overview of this dissertation.

1.5 Overview of this work

In Chapter II we provide a different derivation of Eq. 1.39 and test its validity after taking into account the aforementioned projection effects. More specifically, we derive the escape velocity profile for an Einasto density field in an accelerating universe and demonstrate its physical viability by comparing theoretical expectations to both light-cone data generated from N-body simulations and archival data of 20 galaxy clusters. We demonstrate that the projection function ($g(\beta)$) is deemed physically viable only for the theoretical expectation that includes a cosmology-dependent term. Using simulations, we show that the inferred velocity anisotropy is more than 6σ away from the expected value for the theoretical profile which ignores the acceleration of the universe. In the archival data, we constrain the average galaxy cluster velocity anisotropy parameter of a sample of 20 clusters to be $\beta = 0.248^{+0.164}_{-0.360}$ at the 68% confidence level.

As shown with Eq. 1.40, in order to de-project the projected escape velocity profiles we need an independent estimate of β. In Chapter III we develop such an approach. In particular, we present an analytic approach to lift the mass-anisotropy degeneracy in clusters of galaxies by utilizing the line-of-sight velocity dispersion of clustered galaxies jointly with weak lensing-inferred masses. More specifically, we solve the spherical Jeans equation by assuming a simple relation between the line-of-sight velocity dispersion and the radial velocity dispersion and recast the Jeans equation as a Bernoulli differential equation which has a well-known analytic solution. We first test our method in cosmological N-body simulations and then derive the anisotropy profiles for 35 archival data galaxy clusters with an average redshift of $\langle z_c \rangle = 0.25$. The resulting profiles yield a weighted average global value of $\langle \beta(0.2 \leq r/r_{200} \leq 1) \rangle = 0.35 \pm 0.28$ (stat) ± 0.15 (sys). This indicates that clustered galaxies tend to globally fall on radially anisotropic orbits. We note that this is the first attempt to derive velocity anisotropy profiles for a cluster sample of this size utilizing joint dynamical and weak lensing data.

Having corroborated that our model works, in Chapter IV we present a novel approach to constrain accelerating cosmologies with the projected galaxy cluster escape velocity profile. With the Fisher matrix formalism we forecast constraints on the cosmological parameters that describe the cosmological expansion history. We find that our probe has the potential of providing constraints comparable to, or even stronger than, those from other cosmological probes. More specifically, after applying a conservative 80% mass scatter prior on each cluster and marginalizing over all other parameters, we forecast 1σ constraints on the dark energy equation of state w and matter density parameter Ω_M of $\sigma_w = 0.138(0.431)$ and $\sigma_{\Omega_M} = 0.007(0.025)$ in a flat universe for a sample of 1000 (100) clusters uniformly distributed in the redshift range $0 \leq z \leq 0.8$. Assuming 40% mass scatter and adding a prior on the Hubble constant we can achieve a constraint on the CPL parametrization of the dark energy equation of state parameters w_0 and w_a with 100 clusters in the same redshift range: $\sigma_{w_0} = 0.191$ and $\sigma_{w_a} = 2.712$. Dropping the assumption of flatness and assuming

$w = -1$ we also attain competitive constraints on the matter and dark energy density parameters: $\sigma_{\Omega_M} = 0.101$ and $\sigma_{\Omega_\Lambda} = 0.197$ for 100 clusters uniformly distributed in the range $0 \leq z \leq 0.8$ after applying a prior on the Hubble constant. We also discuss various observational strategies for tightening constraints in both the near and far future.

Lastly, as hinted at in this introduction, modified theories of gravity provide us with a unique opportunity to generate innovative tests of gravity. In Chameleon $f(R)$ gravity, the gravitational potential differs from the weak-field limit of general relativity (GR) in a mass dependent way. In Chapter V develop a probe of gravity which compares high mass clusters, where Chameleon effects are weak, to low mass clusters, where the effects can be strong. We utilize the escape velocity edges in the radius/velocity phase space to infer the gravitational potential profiles on scales of 0.3 - 1 virial radii. We show that the escape edges of low mass clusters are enhanced compared to GR, where the magnitude of the difference depends on the background field value $|\overline{f_{R0}}|$. We validate our probe using N-body simulations and simulated light cone galaxy data. For a DESI (Dark Energy Spectroscopic Instrument) Bright Galaxy Sample, including observational systematics, projection effects, and cosmic variance, our test can differentiate between GR and Chameleon $f(R)$ gravity models, $|\overline{f_{R0}}| = 4 \times 10^{-6}$ (2×10^{-6}) at $> 5\sigma$ $(> 2\sigma)$, more than an order of magnitude better than current cluster-scale constraints.

In Chapter VI, we close this work with possible openings, challenges, and perspectives for future investigations. In the last pages of this dissertation, enumerated in the various Appendices, we provide derivations and in-depth explanations of various equations used throughout this work, mostly as they pertain to Chapter IV.

CHAPTER II

Escaping a galaxy cluster in an accelerating universe

2.1 Introduction

The late-time acceleration of the universe is one of the most profound mysteries of physical cosmology. As briefly mentioned in the introductory chapter, what is at stake with this discovery is the following: either our universe is composed of some exotic "dark energy" whose physics drives the dynamics of acceleration and/or our general relativistic theory of gravity must be extended or modified (Joyce et al., 2015; Koyama, 2016; Joyce et al., 2016).

Given its profound importance, cosmic acceleration is currently being investigated through a broad constellation of probes that mobilize a range of astrophysical objects and phenomena such as: Type Ia supernovae, Baryon Acoustic Oscillations (BAO), weak gravitational lensing and galaxy clusters (see Weinberg et al. (2013) for an excellent review of these and other approaches).

Galaxy clusters in particular are vital laboratories that allow us to sensitively probe the physics of large-scale structure formation and thereby constrain cosmological models of our universe (Kravtsov & Borgani, 2012b). The method most commonly undertaken is based on the cluster abundance function, which evolves in shape and amplitude as a function of the cosmological parameters (Vikhlinin et al., 2009; Rozo et al., 2010). The abundance function as a cosmological probe depends not only on robust analytic theory which is calibrated through simulations, but also on accurate masses as inferred from dynamical, weak lensing and X-ray methods.

An alternative way of constraining cosmology that does not depend directly on the galaxy cluster abundance function was developed in Regoes & Geller (1989b) and extended by Regoes (1996). Both of these papers constrain the cosmological matter density parameter through an analysis of the phase (velocity vs. distance) space of galaxy clusters. More specifically, as demonstrated by Kaiser (1986) the infall pattern around galaxy clusters forms a trumpet-shaped profile in their phase spaces. This trumpet-shaped profile, also known as a phase space "caustic", can be inferred from the line-of-sight velocity information. When compared to what is predicted by spherical infall models, an estimate on the matter density parameter of the universe may be inferred. However, the capacity for the caustic amplitude and shape to precisely constrain the matter density parameter, at least when considering both linear and non-linear theory from the spherical infall model, have since been called into question (Diaferio & Geller, 1997a).

In particular, Diaferio & Geller (1997a) demonstrated that the caustic profiles were related to the escape velocity profile of the cluster as mediated by a projection function. This projection function stems from the fact that we observe only the line-of-sight component of a galaxy's velocity and because the true velocity vectors can be non-isotropic. Only after projection can the caustics be utilized to infer the mass profiles of galaxy clusters. While this method opened the path for a novel way of estimating the mass profiles of galaxy clusters, the capacity for the caustic to constrain cosmology directly has not been pursued.

In what follows, as was shown with 3-dimensional phase spaces from N-body simulations in Miller et al. (2016), we argue that in order to properly model the escape velocity profile of galaxy clusters as inferred from their phase spaces a cosmological acceleration term must be included. The reason for this is that the escape velocity profile is often defined by integrating the density profile out to infinity via the integral form of the Poisson equation. However, current analytical expressions of the gravitational potential of galaxy clusters at "infinity" are not well defined. As such, if the potential is not properly normalized it will yield the wrong escape velocity profile.

In particular, we extend the work Miller et al. (2016), presented in Chapter I, by including projection effects and also testing the theory and the algorithm on real data. More specifically, we use projected synthetic data from the Henriques et al. (2012) light-cone as well as archival data of 20 galaxy clusters with extensive spectroscopic data and weak lensing mass profiles. We analyze the cosmology-dependent escape velocity profiles as inferred from their projected phase spaces and assess the viability of our analytic expectations. We note that only when including cosmological effects do we recover values for the velocity anisotropy parameter that are in agreement with ΛCDM simulations and with various other observational studies: Łokas et al. (2006), Benatov et al. (2006), Lemze et al. (2009), Wojtak & Łokas (2010), and Biviano et al.

(2013).

The outline of this chapter is as follows: in Section 2.2 we derive and review the theoretical expectations related to our observable: the escape velocity profile of galaxy clusters. In Section 2.3 we outline how this observable is inferred from the phase space of galaxy clusters. From thereon, in Section 2.4, we describe both the synthetic and non-synthetic projected data we utilized to probe our theoretical expectations. In Section 2.5 we describe projection effects and estimate the value of the velocity anisotropy parameter we infer assuming two different theoretical expectations of the escape velocity profile: one that includes the cosmological term and one that does not. In the following section, Section 2.6, we thoroughly assess likely sources of systematics affecting our analysis. We follow this analysis with a discussion and conclusion in sections 2.7 and 2.8 respectively.

Except for the case of synthetic data in which the cosmological parameters are already defined (Springel et al., 2005a), in what follows we assume a flat ΛCDM cosmology with $\Omega_M = 0.3$, $\Omega_\Lambda = 1 - \Omega_M$, and $H_0 = 100h$ km s^{-1} Mpc^{-1} with $h = 0.7$.

2.2 Theoretical expectations

The theory of general relativity and its derivative cosmological models demonstrate that the dynamics of the matter-energy and the universe's expansion dynamics are dialectically entwined. As it is often said: matter-energy tells space-time how to curve and space-time tells matter-energy how to move. For instance, in the case of galaxy cluster-sized halos, large scale cosmological dynamics are expressed in the amplitude and shape of the halo mass function (Tinker et al., 2008). Qualitatively, what this tells us is that the dynamics of the galaxies in a gravitationally bound structure such as a galaxy cluster must also necessarily be affected by cosmology.

In this chapter we focus on a particular observable, the escape velocity profile of clusters as inferred from their phase space, and test the ways in which analytical formulations of this observable must necessarily introduce a cosmological term in order to accurately describe the escape velocity edges of galaxy clusters. In particular, the velocity profile (v_{esc}) can be inferred analytically by characterizing the potential (ϕ) a given test particle must escape from,

$$v_{esc}^2 = -2\phi. \tag{2.1}$$

However, as mentioned in section 2.1, the cosmological effect on the escape velocity profile has to be included in this potential. We now derive the escape velocity profile that includes cosmology and which has been utilized and tested against both ΛCDM universe simulations (Behroozi et al., 2013; Miller et al., 2016) and extensions to general relativity such as Chameleon $f(R)$ gravity (Stark et al., 2016). We then extend those derivations to include projection effects.

2.2.1 Derivation of the escape velocity profile of a galaxy cluster in an accelerating universe

Nandra et al. (2012a) demonstrated that in the weak field approximation of general relativity and at sub-horizon scales, a massive particle will still feel a force from the accelerated expansion of space. Following Nandra et al. (2012a), then, the effective acceleration experienced by a massive particle with zero angular momentum in the vicinity of a galaxy cluster with gravitational potential (Ψ) is given by,

$$\vec{\nabla}\Phi = \vec{\nabla}\Psi + qH^2 r\hat{r}. \tag{2.2}$$

The effective potential (Φ) therefore takes into account both the curvature produced by a density field with potential Ψ and the curvature produced by the acceleration term qH^2r. From a Newtonian perspective, then, this last term can be thought of as a repulsive force that opposes the inward pull of the cluster's mass distribution.

In the second term of equation 2.2, q is the usual deceleration parameter given by: $q \equiv -\frac{\ddot{a}a}{\dot{a}^2}$.We assume a flat universe ($\Omega_k = 0$), and a dark energy equation of state parameter $w = -1$. Also, given that we work in low-redshift regime (such that $\Omega_\gamma(z) \approx 0$) the deceleration parameter can be expressed in terms of the redshift evolving matter density parameter ($\Omega_M(z)$) and the redshift evolving Λ density parameter ($\Omega_\Lambda(z)$), $q(z) = \frac{1}{2}\Omega_M(z) - \Omega_\Lambda(z)$. For our chosen cosmology at the present epoch, we attain: $q(z = 0) = -0.55$. Lastly, the Hubble parameter (H) for this same cosmology is as usual, $H(z) = H_0E(z) = H_0\sqrt{(1 - \Omega_M) + \Omega_M(1 + z)^3}$.

Having defined the cosmological quantities that compose equation 2.2, we can integrate over the physical radius (r) to find the effective potential, and subsequently the escape velocity profile via equation 2.1 with effective potential Φ. Integrating equation 2.2,

$$\int_r^{r_{eq}} d\Phi = \int_r^{r_{eq}} d\Psi + qH^2 \int_r^{r_{eq}} r' dr'. \tag{2.3}$$

Note that we are integrating out not to infinity but to a finite radius, r_{eq}, which is termed the "equivalence radius" in Behroozi et al. (2013). The reason for this is that the escape velocity at infinity is poorly defined. This ambiguity introduces a problem with the normalization of the potential that is used to calculate the escape velocity profile. In particular, as demonstrated in Miller et al. (2016) this offset ends up overestimating the potential by $\sim$20%. Following Behroozi et al. (2013) we define the equivalence radius to be the point at which the acceleration due to the gravitational potential of the cluster and the acceleration of the expanding universe are equivalent ($\vec{\nabla}\Phi = 0$) which yields, $r_{eq} = (\frac{GM}{-qH^2})^{1/3}$, where G is the gravitational coupling constant and M is the mass of the cluster as inferred from a choice of Ψ via the Poisson equation, as detailed in subsection 2.2 below. Now, integrating equation 2.3 out to r_{eq}, we have,

$$\Phi(r) = \Psi(r) - \Psi(r_{eq}) + \frac{1}{2}qH^2\big(r^2 - r_{eq}^2\big) + \Phi(r_{eq}). \tag{2.4}$$

Setting the boundary condition such that the escape velocity must necessarily be 0 at the equivalence radius, $-2\Phi(r_{eq}) = v_{esc}^2(r_{eq}) = 0$, and using equation 2.1 we find,

$$v_{esc}(r) = \sqrt{-2\big(\Psi(r) - \Psi(r_{eq})\big) - qH^2\big(r^2 - r_{eq}^2\big)}. \tag{2.5}$$

This reproduces the result shown in Stark et al. (2016) and Miller et al. (2016).Note that equation 2.5 is therefore normalized to yield an escape velocity of zero at the equivalence radius once a Ψ has been chosen. Note also that equation 2.5 yields the escape velocity profile in an accelerating universe for any choice of gravitational potential Ψ.

From now on we refer to this escape velocity profile as "Einasto qH^2" because we choose the Einasto model to describe the potential Ψ. We describe this choice in detail below.

2.2.2 Potential-density pair

While it is common to describe the density profile of galaxy clusters with the NFW model of dark matter halos (Navarro et al., 1996, 1997), recent investigations have shown that the NFW potential-density pair over estimates the escape velocity profile by $\sim$10% within galaxy clusters (Miller et al., 2016). This is because, on average, the NFW profile tends to overestimate the mass in the outskirts of galaxy clusters (see also Diemer & Kravtsov (2015)).

Moreover, as is also demonstrated by Miller et al. (2016), in contrast to the NFW model, once the cosmological term (Eq. 2.5) has been included, both the Gamma (Dehnen, 1993) and Einasto (Einasto, 1965) gravitational potential profiles can model the radial escape velocity profiles to better than 3% precision. In what follows, we utilize the Einasto profile. However, we emphasize that our analysis is not dependent on the Ψ used. That is, insofar as the gravitational potential profiles are derived from a true density-potential pair, all of our analysis will yield the same results.

Because nearly all published weak-lensing mass profiles utilize the NFW model, we need to map the NFW parameters to the equivalent parameters in the Einasto profile. The Einasto representation of dark matter halos (Einasto, 1965) is a three parameter model (n, ρ_0, r_0) described by the following fitting formula for the density profile,

$$\rho(r) = \rho_0 \mathrm{exp}\Bigg[- \left(\frac{\mathrm{r}}{\mathrm{r}_0}\right)^{1/\mathrm{n}} \Bigg]. \tag{2.6}$$

From the density field described by equation 2.6 we can derive the gravitational potential using the integral form of the Poisson equation. As demonstrated by Retana-Montenegro et al. (2012) this yields,

$$\Psi(r) = -\frac{\mathrm{GM}}{r}\left[1 - \frac{\Gamma\big(3n, (\frac{r}{r_0})^{1/n}\big)}{\Gamma(3n)} + \frac{r}{r_0}\frac{\Gamma\big(2n, (\frac{r}{r_0})^{1/n}\big)}{\Gamma(3n)}\right]. \tag{2.7}$$

As in Miller et al. (2016), ρ_0 (or the mass term M) can be thought of as the normalization, r_0 is the scale radius and n is the index.

Following Retana-Montenegro et al. (2012), we use $\Gamma(3n) = 2\Gamma(3n, d_n)$ where the d_n term is solved for via asymptotic expansion. In particular, we use the d_n term cited therein expanded up to the fifth order, with $\alpha = 1/n$,

$$\begin{aligned} d_\alpha \approx \frac{3}{\alpha} - \frac{1}{3} + \frac{8}{1215}\alpha + \frac{184}{229635}\alpha^2 \\ + \frac{1048}{31000725}\alpha^3 - \frac{17557576}{1242974068875}\alpha^4 + \mathcal{O}(\alpha^5). \end{aligned} \tag{2.8}$$

Lastly, $\Gamma(a, x)$ denotes the upper incomplete gamma function, given as usual by:

$$\Gamma(a, x) = \int_x^\infty t^{a-1} e^{-t} dt. \tag{2.9}$$

As shown in Sereno et al. (2016a) and references therein, the mapping between NFW and Einasto profiles is straightforward. In our case, we insist that the two profiles be nearly identical within r_{200}. We do this by solving for the Einasto parameters which match analytical NFW density profiles on a cluster-by-cluster basis. As noted by Sereno et al. (2016a), recent weak lensing analyses of stacked clusters cannot distinguish between the Einasto and NFW halo representations of the density profile within this range.

2.2.3 Comparing theoretical escape velocity profiles with and without the cosmological terms

In Fig. 2.1 we show the resulting profiles for a single cluster-sized halo at $z = 0$. In particular we plot both the escape velocity profiles for the Einasto qH^2 profile (Eq. 2.5) with three different cosmologies (dashed, solid and dash-dotted lines) and for the Einasto profile without the cosmological term (dotted line): $v_{esc}(r) = \sqrt{-2\Psi(r)}$.

As set by our aforementioned boundary condition, the Einasto qH^2 escape velocity profiles all reach $v_{esc}(r) \to 0$ as $r \to r_{eq}$. We also highlight the significant difference between the Einasto qH^2 model with $\Omega_M = 0.3$ and the Einasto model without the cosmological term. Lastly, note that as we increase Ω_M our Einasto qH^2 profiles converge to the Einasto profile without the cosmological term.

Given that all other data indicate we do not live in an Einstein-de Sitter universe, we should be able to detect the $\gtrsim 10\%$ cosmology-dependent effects on the escape velocity profiles of galaxy clusters. We first test our theoretical expectations in N-body simulations in order to thoroughly assess systematic effects (including projection effects, mass scatter, and more, as explained in the subsequent sections) and then utilize archival redshift data and weak lensing mass estimates of 20 galaxy clusters to test our expectations.

2.3 Theoretical Observables

As is clear from our theoretical expectations, our observables are the projected escape velocity profile of galaxy clusters ($v_{esc}^{edge}(r)$) and the observed weak-lensing mass profile. We use the latter in our analytic model of the 3-dimensional escape edge and we require the cosmology and the projection function as described in Section 2.5.2.

We utilize the redshift information of galaxy clusters to generate phase spaces (v_{los} vs. r space) from which we infer the escape velocity profile. More specifically, we do this by transforming the galaxy redshifts at a given angular separation from the cluster center (θ) to line-of-sight (v_{los}) velocities at the cluster's redshift (z_c) via,

$$v_{los} = c\frac{(z - z_c)}{(1 + z_c)}. \tag{2.10}$$

Where c is the speed of light, and z denominates the redshift of individual galaxies. To

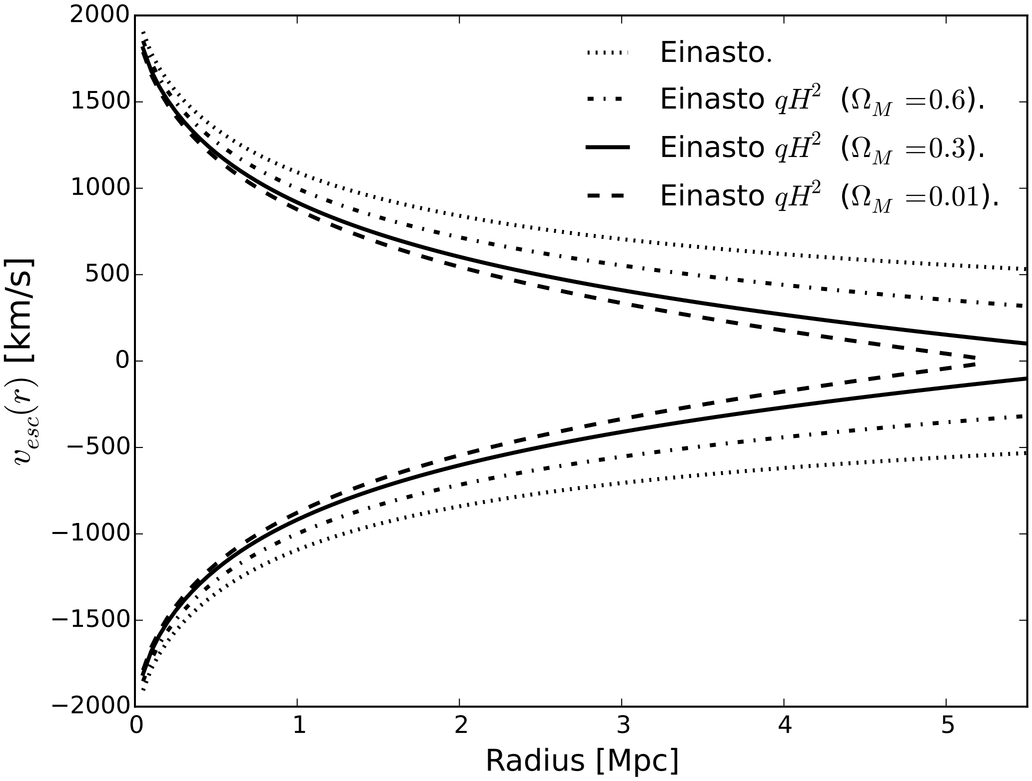

Figure 2.1: Escape velocity profiles for a single cluster of fixed mass using equations 2.5 and 2.7 for four different escape velocity profile models ($v_{esc}(r)$). Note that while we change Ω_M we keep $h = 0.7$ for a fiducial flat ΛCDM cosmology. We note the significant difference between the Einasto qH^2 theoretical expectations for three different flat ΛCDM cosmologies with differing matter density parameters ($\Omega_M = 0.01, 0.3, 0.6$, denoted by dashed, solid, and dashed dotted lines respectively) and the "Einasto" theoretical expectation which does not include a cosmological term (denoted by dotted line) given by $v_{esc}(r) = \sqrt{-2\Psi(r)}$ (and using equation 2.7). Note that increasing Ω_M raises the escape velocity at all radii. Going in the opposite direction, we notice that as our universe becomes more and more dominated by Λ it will in principle be easier for galaxies to escape clusters. Secondly, we note that as Ω_M increases we recover the non-cosmological escape velocity (dotted line). Note also, as implied by equation 2.5, that the Einasto qH^2 profiles all eventually reach some radius (the equivalence radius "r_{eq}") at which the escape velocity is zero.

calculate the physical distance from the cluster's center (r) we calculate the angular diameter distance (d_A) and use the angular separation (θ),

$$r = d_A(z)\theta = \left[\frac{1}{1+z}\frac{c}{H_0}\int_0^z \frac{dz'}{E(z')}\right]\theta. \tag{2.11}$$

For each cluster phase space we then identify the edge in radial bins of 0.1 Mpc by finding galaxies with the top 10% velocities. We follow the interloper removal prescriptions of Gifford et al. (2013) and Gifford et al. (2016). The latter tested this edge detection technique on projected data in two different simulations with widely varying values for $\sigma_8 = 0.8$ vs $\sigma_8 = 0.9$, where σ_8 is the normalization of the matter power spectrum on 8 Mpc scales. They conclude that the edge detection is independent of large variations in the line-of-sight interloper fraction. We also test the robustness of this edge-detection technique as discussed in the Systematics section below. There are various techniques used to define phase space edges in the literature (Diaferio & Geller, 1997a; Gifford et al., 2013; Serra et al., 2011; Rines et al., 2013; Geller et al., 2013; Lemze et al., 2009; Miller et al., 2016). With N-body simulations Miller et al. (2016) have shown that the escape velocity edge (v_{esc}^{edge}) can be inferred with $\sim$ 5% accuracy. We discuss all of this more thoroughly in the Systematics section.

The weak lensing mass profiles are taken from the literature (Sereno, 2015). As noted in Section 2.2.2, these are provided as NFW profiles and we convert them to Einasto density profiles on an individual basis. When the NFW concentration parameter is not provided, we use the mass-concentration from Duffy et al. (2008). We include the weak lensing mass errors as provided in the literature.

2.4 Data

We first test our theoretical expectations with a sample of synthetic clusters from theHenriques et al. (2012) light-cone data. After having assessed relevant systematics (thoroughly described in Section 6 below) with the synthetic data we conduct our analysis on 20 clusters with weak lensing and redshift data. We briefly discuss these data sets below.

2.4.1 Synthetic data

We utilize the Millennium simulation (Springel et al., 2005a) which employs a flat cosmology with $\Omega_M = 0.25$ and $h = 0.73$. In particular we pick all the clusters above $M_{200} > 4 \times 10^{14} h^{-1} M_{\odot}$ in the Henriques et al. (2012) light-cone and from there we ensure that each cluster has $N \gtrsim 110$ galaxies within $2r_{200}$ and between $-2000 \leq v_{los} \leq 2000$ km/s. We do this to ensure that the phase spaces we are working with are well sampled so that we may accurately infer escape velocity edges from them. From these cuts, we end up working with a sample of 200 halos. We then cross-correlate this light-cone data sample with the Guo et al. (2011a) catalog in order to obtain 3-dimensional velocity information for each of our projected clusters in the Henriques et al. (2012) light cone. This 3-dimensional information is needed in order to compute the velocity anisotropy parameter of each cluster. We expand on this in Section 5 below. Out of the sample of 200 clusters we separate them into ten sets of 20 with similar mass distributions in order to create a sample with comparable statistics as our archival non-synthetic galaxy cluster sample.

2.4.2 Archival data: weak lensing masses and galaxy redshifts

We used the VizieR catalog (Ochsenbein et al., 2000) to search for redshift data of galaxy clusters with weak lensing mass estimates. The galaxy redshift information is taken from a variety of sources (Rines et al., 2013; Miller et al., 2006; Ellingson et al., 1997; Sánchez-Portal et al., 2015; Geller et al., 2014; Zitrin et al., 2012; Owers et al., 2011a; Rines et al., 2003; Lemze et al., 2013) and so are the weak lensing mass estimates (Okabe & Umetsu, 2008; Okabe & Smith, 2015; Hoekstra et al., 2015; Umetsu et al., 2012; Gavazzi et al., 2009). The references for both weak lensing mass profiles and galaxy redshifts for each of the 20 clusters in our sample are summarized in Table 2.1. Note that while we cite the original source of the weak lensing papers we ultimately use the M_{200} masses and errors in our analysis compiled in the Sereno (2015) meta catalog. We particularly chose to utilize this meta catalog because it includes standardized weak lensing mass estimates across cosmologies.[1] Note that the only case in which we use the exact mass as made explicit in the weak lensing papers listed in Table 2.1 is for A1656 given that this cluster is not included in the Sereno (2015) meta catalog.

As with the synthetic galaxy cluster sample, all 20 of our clusters have $N \gtrsim 110$ galaxies within $2r_{200}$ and between $-2000 \leq v_{los} \leq 2000$ km/s. The only exception is A2111 which has $N = 87$ galaxies within that range. The mass range of the data lies between $5 \times 10^{14} M_{\odot}$ and $2.6 \times 10^{15} M_{\odot}$.

The meta catalog only lists masses inferred from NFW fits (Navarro et al., 1996,

---

[1] The latest and most updated weak lensing parameter estimates from the meta catalog can be accessed through Mauro Sereno's website: `pico.bo.astro.it/~sereno/CoMaLit/LC2/2.0/`.

Table 2.1: List of Galaxy Clusters and References

Cluster name[2]	Redshift	Weak lensing[3]	Galaxy redshifts
A2111	0.229	H15	Miller et al. '06
A611	0.288	H15	Lemze et al. '13
MS1621	0.428	H15	Ellingson et al. '97
Cl0024	0.3941	H15	Sanchez et al. '15
A2259	0.164	H15	Rines et al. '13
A1246	0.1921	H15	Rines et al. '13
A697	0.2812	H15	Rines et al. '13
A1689	0.1842	H15	Rines et al. '13
A1914	0.166	H15	Rines et al. '13
A2261	0.2242	H15	Rines et al. '13
A1835	0.2506	H15	Rines et al. '13
A267	0.2291	H15	Rines et al. '13
A1763	0.2312	H15	Rines et al. '13
A963	0.206	H15	Rines et al. '13
A383	0.187	H15	Geller et al. '14
A2142	0.0909	OU08	Owers et al. '11
RXJ2129	0.2339	OS15	Rines et al. '13
A2631	0.2765	OS15	Rines et al. '13
MACS1206	0.439	U12	Zitrin et al. '12
A1656	0.0237	G09	Rines et al. '03

1997) to weak lensing shear measurements. As discussed in Section 2.2.2, we convert the NFW profiles to Einasto density profiles.

2.5 Testing our theoretical expectations

To summarize, with galaxy redshift information for each cluster we create a phase space with its line-of-sight velocities (v_{los}). From this phase space we infer the escape velocity edge (v_{esc}^{edge}), as detailed in Section 3. On the other hand, with mass profile measurements we generate an analytic escape velocity profile through equation 2.5 after assuming a gravitational potential with the form of equation 2.7 (i.e. the Einasto model of dark matter halos). We expect that if our theoretical expectations can reproduce the edge profile to high precision then the average ratio v_{esc}^{edge}/v_{esc} should yield unity. What Miller et al. (2016) has shown is that the Einasto model with the additional cosmological term can analytically reproduce velocity escape edges inferred from 3-dimensional phase spaces to high precision. Therefore, when comparing our analytic formulation with edges inferred from projected phase spaces, any difference between this ratio and unity should arise from projection effects.

2.5.1 Projection effects

As demonstrated by Diaferio & Geller (1997a) and Diaferio (1999) the 3-dimensional escape velocity profile ($v_{esc}(r)$) can be projected by a function of the velocity anisotropy parameter ($g(\beta)$),

$$v_{los}(r) = v_{esc}(r) \times \left(\sqrt{g(\beta(r))}\right)^{-1}. \tag{2.12}$$

Where $g(\beta(r))$ is given by,

$$g(r) = \frac{3 - 2\beta(r)}{1 - \beta(r)}. \tag{2.13}$$

The anisotropy parameter (β) is given by the ratio of the velocity dispersion in the tangential direction (σ_t) to the velocity dispersion in the radial direction (σ_r),

$$\beta(r) = 1 - \frac{\sigma_t^2}{\sigma_r^2}, \tag{2.14}$$

where $\sigma_t^2 = \frac{1}{2}\left(\sigma_\theta^2 + \sigma_\phi^2\right)$ includes both azimuthal and latitudinal velocity dispersions. The limiting cases are: radial infall ($\beta = 1$), circular motion ($\beta = -\infty$) and isotropy ($\beta = 0$).

Therefore, if we had the 3-dimensional velocity information for each of our clusters we can calculate β and directly project our profiles. However, in practice this parameter is difficult to determine and as such we are left to infer what β would be given an expected theoretical profile for a given cluster and compare our result with simulations.

2.5.2 Inferring the anisotropy parameter

Given that our theoretical expectation matches the edges in 3-dimensions to high precision, by taking the ratio between the escape velocity edge and our theoretical profile we should be able to infer the anisotropy parameter via,

$$\left\langle \frac{v_{esc}^{edge}(r)}{v_{esc}(r)} \right\rangle \left\langle \sqrt{g(r)} \right\rangle = 1. \tag{2.15}$$

The brackets in equation 2.15 signify that the average is calculated on $N = 20$ clusters. That is, we calculate the ratio for each cluster and then take the average at each radial bin, with a separation of $\Delta(r/r_{200}) = 0.1$. Moreover, the averaged ratio is weighted by the error on the ratio of each individual cluster at a given radial bin. The details of our error budget are thoroughly discussed in the Systematics section below.

Using equation 2.15, for a given average ratio, we can find what average $g(\beta(r))$ is needed to make that ratio unity. Then by inverting equation 2.13 we can find the anisotropy parameter β via,

$$\beta(r) = \frac{3 - g(r)}{2 - g(r)}. \tag{2.16}$$

Lastly, the theoretical expectation (v_{esc}) can be either the escape velocity profile with the cosmological term (i.e. Einasto qH^2, Eq. 2.5) or without it (i.e. just the Einasto potential, Eq. 2.7: $v_{esc}(r) = \sqrt{-2\Psi(r)}$). The differences between the inferred β parameters for these two analytic profiles are detailed in section 5.2.1 and 5.2.2 for the synthetic sample, respectively. For the archival data we only compare our inferred β assuming the Einasto qH^2 theory.

2.5.2.1 Synthetic data and theory with cosmological term

Assuming $v_{esc}(r)$ in equation 2.15 is the Einasto qH^2 model (Eq. 2.5), for a single set of 20 clusters in our synthetic sample, the weighted average ratio is shown in Fig. 2.2 (black stars).

We then can calculate the χ^2 between the left-hand side of Equation 2.15 and the right-hand side (unity) in the range $0.3 < r/r_{200} < 1$ in order to infer the most

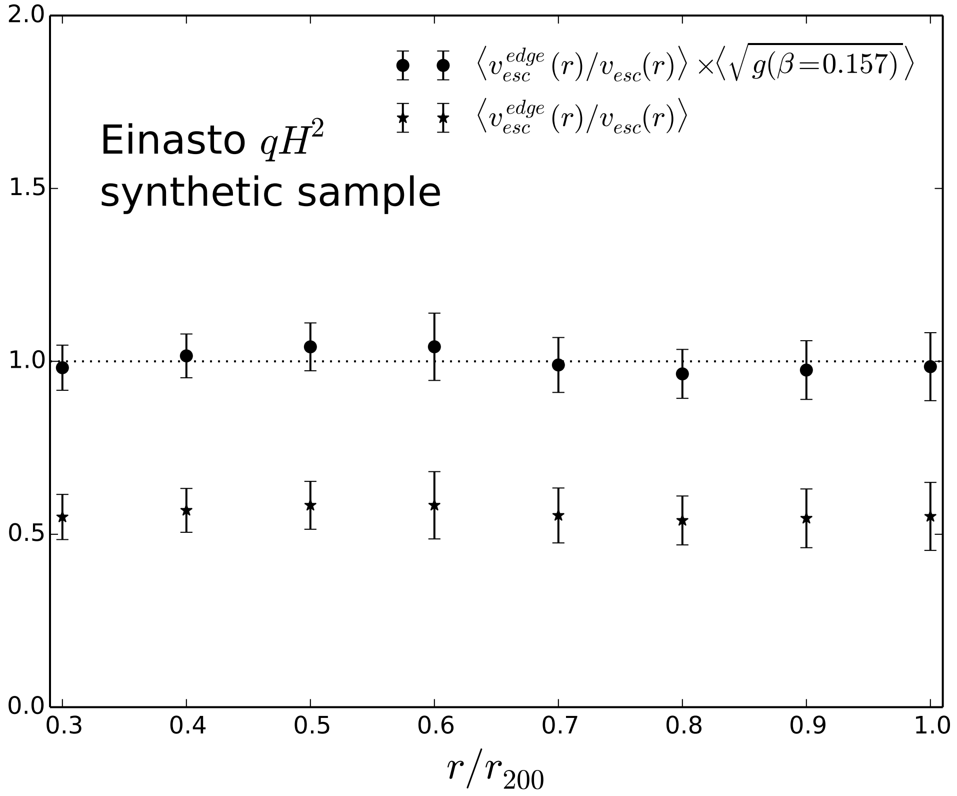

Figure 2.2: The unprojected (stars) and projected (circles) weighted average ratio between the escape velocity edge and the theoretically expected escape velocity profiles with the Einasto qH^2 model for a single set of 20 synthetic clusters from the Henriques et al. (2012) light cone. The error is the 1σ error on the averaged ratio assuming a uniform 25% mass scatter on the virial mass of each cluster and a 5% scatter on the escape velocity edge. The unprojected ratios are projected after calculating the most likely average β by comparing to the unity line (see Equation 2.15). We find this value to be well in agreement with simulation results (see figure 2.3).

likely average β for this set of 20 synthetic clusters. The uncertainty we use in this calculation is therefore the error on the mean on each of the radial bins, as shown by the error bars in Fig. 2.2. Note that, necessarily, we also utilize the relation shown in Eq. 2.16. Note also that we focus on the region between $0.3 < r/r_{200} < 1$ because simulation results have shown that the anisotropy parameter is–on average–constant across different redshifts within this radial range (Serra et al., 2011; Lemze et al., 2012; Munari et al., 2013) which justifies the assumption of a constant β.

Moreover, with the χ^2 we calculated, and assuming a Gaussian likelihood $\mathcal{L} \propto \exp[-\chi^2/2]$, we can generate a likelihood plot of our inferred average β for each of our ten sets of 20 synthetic clusters. The result is shown by the gray band in Fig. 2.3. The band represents the 1σ error on the distribution of likelihoods for all ten sets of averaged cluster ratios and their inferred β's. In that same figure we compare our inferred β with two other results from synthetic data.

After inferring the most likely β from this method we project the average profile. The projected results for a single set of 20 clusters for this synthetic sample are also shown in Fig. 2.2 (black dots).

The red vertical dashed line is the average anisotropy parameter (also between $0.3 < r_{200} < 1$) as directly measured in 3-dimensions using Eq. 2.14 calculated by Iannuzzi & Dolag (2012). The 2σ bootstrap error on the mean is shown in red dotted lines. The sample used by Iannuzzi & Dolag (2012) is composed of the 1000 clusters in the Millennium simulation at $z = 0$ with virial masses greater than $2 \times 10^{14} M_\odot$. This is a much larger sample size than we use and as such we consider this β to be a robust estimate of the true anisotropy parameter.

The black vertical dashed lines in Fig. 2.3 come from a direct calculation of the anisotropy parameter (using Eq. 2.14) for the superset of 200 clusters with masses $M_{200} > 4 \times 10^{14} M_\odot$ that we use in this work. Our superset has a slightly larger average β, but both our measurement and Iannuzzi & Dolag (2012)'s are within $\sim 2\sigma$ of each other. We hypothesize that this small difference could be attributed to the fact that our simulated data include the orphan galaxies in the Guo et al. (2011a) catalog, whereas Iannuzzi & Dolag (2012) exclude these. Note, for instance, that the β calculated in Lemze et al. (2012) utilized particles and is also larger than the β calculated in Iannuzzi & Dolag (2012).

The gray line (and band) is the likelihood which represents β using only the projected phase-space profiles of 20 clusters (i.e., no 3-dimensional information). As expected, this likelihood is much larger than the error bounds on β from the 3-dimensional information for larger samples. The reason it is larger is because the χ^2

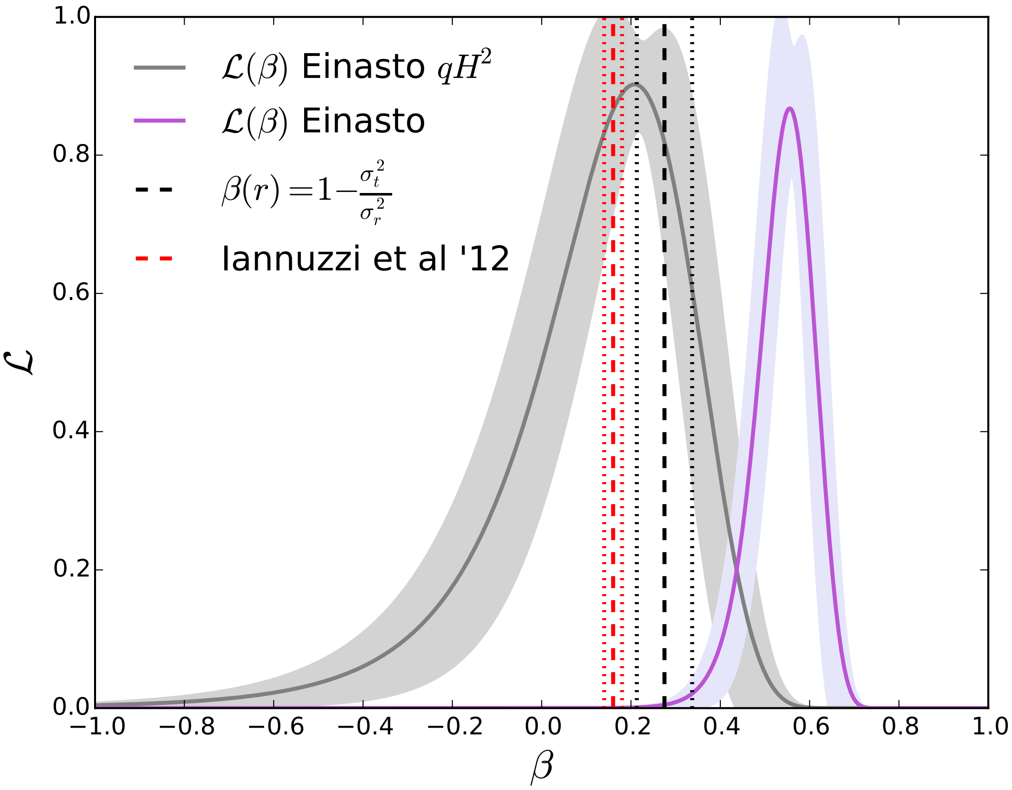

Figure 2.3: The likelihood of the average anisotropy parameter (β) as inferred from ten sets of 20 clusters in the synthetic Henriques et al. (2012) light-cone data. The gray band represents the 1σ variation on the likelihood of the ten sets. We cross-correlated the Henriques et al. (2012) light-cone data with the 3-dimensional velocity data from Guo et al. (2011a) to calculate, analytically, the average beta for the sample via Eq. 2.14 to attain: $\beta = 0.275 \pm 0.062$ at the 95% confidence level (black line dashed and dotted). The red lines represent the β profile with 2σ error (dash and dotted) for 1000 clusters in the Millennium sample calculated also with Eq. 2.14 by Iannuzzi & Dolag (2012). Only by including the cosmological-dependent term on our theoretical formulation can we recover the true β with accuracy and to high precision. Compare the red lines to the purple band which utilizes the Einasto potential for the analytic profile of the escape velocity profile without the cosmological term. We conclude, then, that we can rule out the analytic profile without the cosmological term at the 6.3σ level. Note that the Iannuzzi & Dolag (2012) band is the error on the mean as calculated from a bootstrap algorithm also between $0.3 < r/r_{200} < 1$. Lastly, as mentioned in the text, we assume a uniform 25% mass scatter on M_{200} for all clusters and a 5% error on the escape velocity edge. The cosmology utilized for our analytic profiles is the same as what was utilized to make the simulations (see section 2.4).

analysis includes representative errors on both the weak lensing masses (25%) and the escape edges (5%). However, this likelihood fully captures the true underlying 3-dimensional radially averaged velocity anisotropy.

2.5.2.2 Synthetic data and theory without cosmological term

In both of our synthetic data samples shown in Fig. 2.2 and Fig. 2.3 we took the ratio between escape velocity edge and the Einasto qH^2 analytic profile. Now, assuming we do not actually need the cosmological-dependent term to accurately reproduce the escape edge, we test whether or not we can recover the true anisotropy parameter. More specifically, the $v_{esc}(r)$ in the ratio now utilizes Eq. 2.1 with the Einasto potential of 2.7: $v_{esc}(r) = \sqrt{-2\Psi(r)}$ (rather than Eq. 2.5). The result is shown in Fig. 2.3 (purple band).

As with the gray band described above, the purple band represents the likelihood on the inferred β with the 1σ error representing the standard deviation in the ten sets of 20 synthetic clusters. We see that if we remove the cosmological term, the average anisotropy parameter is much larger and therefore we cannot recover the simulation results. More specifically, assuming the red bands are correct in Fig. 2.3, that is, if it truly describes the anisotropy parameter, then we can rule out the non-cosmological dependent theory (purple band) at the 6.3σ level. Put differently, the average value of β shown by the red dashed line is 6.3σ away from from the range of allowed β's shown with the purple band.

In summary, these tests on the simulations provide two important results: first that our algorithm can recover the average β given only projected data and second that the cosmological model plays a significant role.

2.5.2.3 Archival data and theory with cosmological term

After getting a sense of what we should expect for a given sample size of 20 clusters, and after making concrete the abstract necessity of including a cosmological dependent term in our escape velocity profile by studying the underlying velocity anisotropy distributions with 200 synthetic clusters, we perform the same analysis on an archival data set of 20 galaxy clusters.

The ratio for our sample of 20 clusters, similar to Fig. 2.4, is shown in Fig. 2.4. As with the synthetic data, we calculate the χ^2 and after assuming a Gaussian we can infer the likelihood for the average anisotropy parameter for our set of 20 clusters. Again, the χ^2 is calculated between the left-hand side of Equation 2.15 and the right-hand side (unity) in the range $0.3 < r/r_{200} < 1$ in order to infer the most likely average β for the set of 20 clusters from the archival dataset. The uncertainty on the ratio used for the χ^2 can be seen on Fig. 2.4. The resulting likelihood is shown in Fig. 2.5 where we compare the likelihood of β inferred for the archival set of 20 clusters (black line) to the distribution of β inferred from the synthetic set of clusters (gray band, as in Fig. 2.3).

We find that for our sample of just 20 clusters we recover the peak of the likelihood as inferred from simulations to high accuracy. In particular we find that the value of the most likely anisotropy parameter for our archival data of 20 galaxy clusters is $\beta = 0.248^{+0.164}_{-0.360}$ at the 68% confidence level. Note that we calculate this interval by assuming that the distribution to the right of the peak is Gaussian and then find where $Q > -2\ln[\mathcal{L}(\beta)/\mathcal{L}_{max}]$ (where for our single parameter model $Q = 1$). After this error is calculated then we find the error to the left of the peak by integrating the likelihood from the rightmost error up to the value of β which yields 0.68 times the total area of the likelihood.

In Fig. 2.5 the data likelihood (black line) is larger than the simulation likelihood for β (gray band) and with a longer tail to negative β. This is because in the simulations we applied a representative error on the cluster masses fixed at 25%, whereas the data have errors which vary from 15% to 44%. The larger errors on the weak lensing masses allow for more negative anisotropy. In fact, as we discuss below, the weak lensing mass errors are the dominant component of our error budget.

2.6 Systematics

The agreement between the anisotropy parameter inferred with the archival data of 20 clusters and the ΛCDM simulation results (assuming the Einasto qH^2 theory) is clear. To understand the robustness of this result, we carefully consider possible systematics.

As mentioned in the previous section, we carefully consider the uncertainties that make up our averaged ratio and we weight our data with those errors. In particular, we weight the ratio for a given cluster at a given radius by its error at that radius. More specifically, we propagate the error on the ratio by considering the error on the numerator (i.e. $v_{esc}^{edge}(r)$) and the error on the denominator (i.e. the theoretical escape velocity profile, $v_{esc}(r)$). We consider various uncertainties plaguing these two components of the average ratio below.

Throughout, we use a χ^2 statistic and assume that the errors on the ratios are

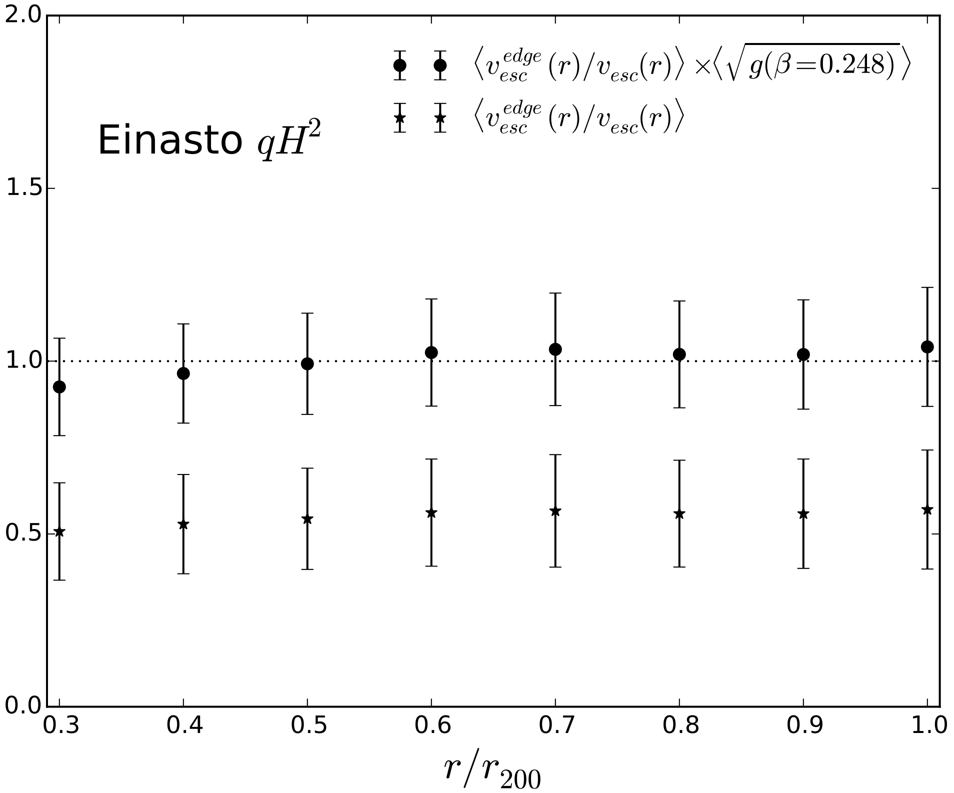

Figure 2.4: The unprojected and projected weighted average ratios between the escape velocity edge and the theoretically expected escape velocity profiles for the set of archival data set of 20 clusters. Note the similarity between this sample and the synthetic sample Fig. 2.2. Given that we are using the particular weak lensing mass errors for each cluster (rather than a uniform mass scatter of 25% as in Fig. 2.2) the overall error on the average ratio is larger.

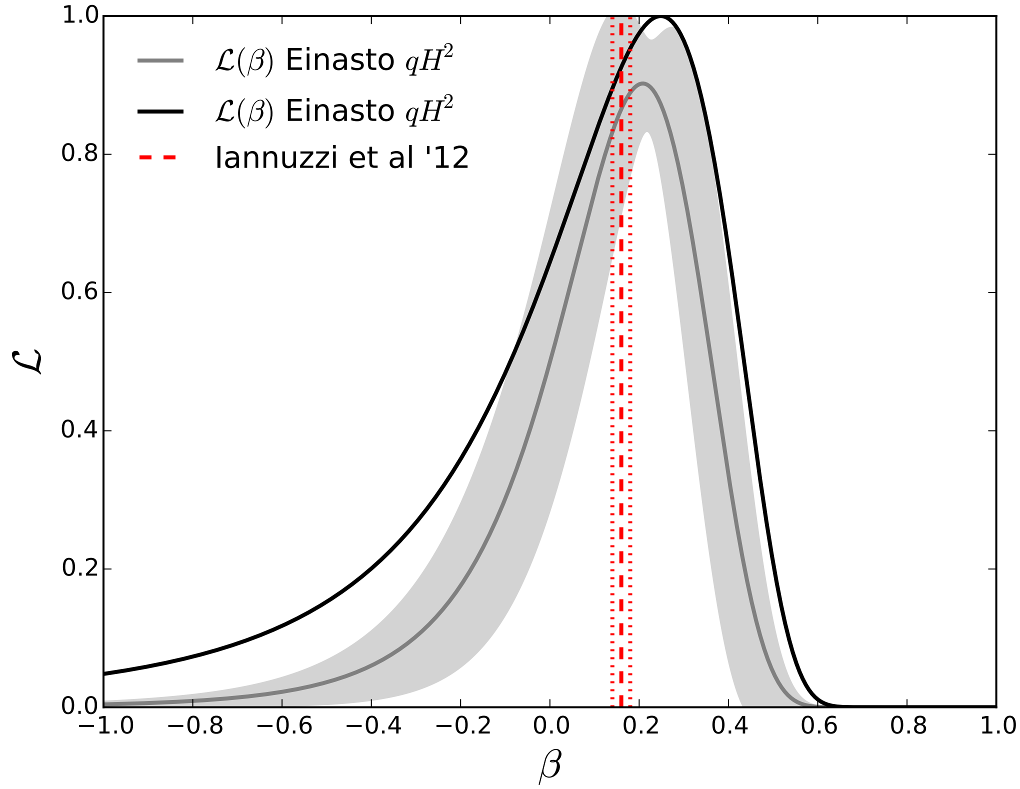

Figure 2.5: The likelihood of the average β as inferred from the set of 20 archival clusters (black line). We also re-plot the likelihood band (gray) from the ten sets of 20 synthetic clusters as well as the results from numerical simulations from Iannuzzi & Dolag (2012) (as in Fig. 2.3). With just 20 clusters we can recover the velocity anisotropy only if the escape velocity profile is described by an Einasto density field with an additional cosmological term (as in equation 2.5).

Gaussian. The fact that our likelihood is centered near the truth for the simulated data indicates that the assumption of Gaussianity is not a bad choice for our analysis.

2.6.1 Escape velocity edge

We propagate the error on the averaged ratio by assuming the error on the numerator, that is on the edge (v_{esc}^{edge}), at each cluster and at each radial bin to be 5% (as studied by Miller et al. (2016)). As mentioned previously, the edge is characterized by the galaxies with projected velocities in the top 10% of the phase-space at a given radial bin. We test the robustness of the edge-detection technique by changing this percentage by 50% and find that the resulting variations lie within our 68% confidence interval error. We note that these variations on the edge affect both the Einasto and Einasto qH^2 β likelihoods equally. As such, it has no direct effect on our results. Furthermore, we utilize the interloper removal technique described in Gifford et al. (2013) which was tested against different cosmologies in Gifford et al. (2016) to infer the edge to high precision using ~ 50 galaxies per phase-space. Note that our clusters have much higher phase-space sampling and thus better contrasted edges. We also compared our edges to those measured with completely independent techniques (e.g., Geller et al. (2013)) and find no significant differences within the scatter and limited sample size used. Given the expectations from theory, the tests in simulated projected data, and the comparison to other observed measurements, we do not consider this component of the average ratio calculation to be a significant source of systematic uncertainty.

2.6.2 Weak lensing masses

2.6.2.1 Mass scatter

In the denominator of the ratio, we calculate the error on the theory (v_{esc}) by folding through the error in the weak lensing mass estimates. The mean ratio is weighted according to its total error, and so our mean ratios can vary slightly if the weak lensing mass errors change. More importantly, the likelihood will shrink (grow) as the weak lensing mass errors shrink (grow). Nonetheless the dominant error on the ratio comes from the weak lensing mass estimates.

Lastly, note that in our calculation of the error we assume that the error on the $v_{esc}^{edge}(r)$ and the error on $v_{esc}(r)$ from the mass scatter have no covariance. This could either raise or decrease our overall error.

2.6.2.2 Mass bias

Another possible systematic that could affect our theoretical expectation is biased weak lensing masses. In particular, biasing all of the weak lensing masses in our archival data sample by 5% (i.e. $M_{200} \rightarrow 0.95 \times M_{200}$), as is perhaps expected by Becker & Kravtsov (2011a), would change the most likely velocity anisotropy parameter to $\beta = 0.138$. This value is still within a reasonable range of our likelihood expectation from the synthetic cluster sample. However, we note that given that we recover the results in simulations by using the same technique we can be confident that we are not utilizing biased masses in our archival data sample.

2.6.3 Mass-concentration relation

Another component that is implicit in our calculation of $v_{esc}(r)$ is the utilization of a mass-concentration relation to attain the NFW density profiles. Recalling from previous sections, we utilize this NFW density to infer the Einasto parameters as described above. In particular, we utilize the Duffy et al. (2008) mass-concentration relation for both the synthetic and archival data samples. Most importantly, this is the relation also used in the metacatalog we utilize (Sereno, 2015). The relation is given by,

$$c_{200}(M_{200}, z) = A_{200}\left(\frac{M_{200}}{M_{piv}}\right)^{B_{200}}(1+z)^{C_{200}}. \tag{2.17}$$

Where $A_{200} = 5.71$, $B_{200} = -0.084$, $C_{200} = -0.47$ and $M_{piv} = 2 \times 10^{12} h^{-1} M_{\odot}$. We recalculated our inferred β from our samples by employing the 1σ error variations on the relation's parameters $(A_{200}, B_{200}, C_{200})$ and found that the inferred β varied only by $\sim 1\%$. Perhaps this is expected given the relative flatness of the mass-concentration relation in the high mass end of the spectrum which is where most of our clusters lie.

2.6.4 Cosmological parameters

As expressed in the preceding sections, our theoretical expectation for the projected escape velocity profile involves assuming a cosmology. Therefore, we expect that the uncertainty in these cosmological parameters will also affect our theoretical escape velocity profile ($v_{esc}(r)$), and consequently, β. We note that the variations for these cosmological parameters are significant. This much is already implied by Fig. 2.1.

In particular we note that decreasing Ω_M to 0.01 changes the peak of the anisotropy likelihood to $\beta = -0.08$. This significant difference in β is due to the fact that the escape velocity profiles would be underestimated in relation to the inferred escape velocity edges. Similarly, increasing Ω_M increases the escape velocity profiles and raises β, thereby shifting the peak to the right. Picking a more realistic uncertainty, we find that a 10% variation in Ω_M, yields a 19% variation in the peak of β.

Increasing H_0 for a constant Ω_M also increases β. The variations are even more accentuated. For example, a 2% variation in H_0 yields a 42% variation in the peak of β. These variations are still within the 95% confidence region as shown in Fig. 2.5.

We emphasize that despite these significant variations on the inferred value of β our goal in this chapter is to test whether we can accurately and precisely reproduce projected escape velocity edges given a cosmology-dependent model.

2.7 Discussion

By utilizing archival data of just 20 galaxy clusters and by picking a fiducial cosmology within the range of what is expected from cosmological probes, we are able to recover the average anisotropy parameter β in agreement with ΛCDM simulations. In this sense, then, we are already implicitly constraining cosmology by picking a reasonable choice of values for h, Ω_m and w. What remains to be seen, however, and this much we defer to future work, is how precisely we can constrain cosmology with Eq. 2.5 once β is independently inferred for each cluster given the scatter on weak lensing masses (our dominant systematic). If β can be inferred for each cluster through an independent technique (e.g. via the Jeans equation), we can leverage this to constrain cosmological parameters in the near future.

We note that our resulting average velocity anisotropies are well in agreement with other analyses (Biviano et al., 2013; Lemze et al., 2009; Łokas et al., 2006; Wojtak & Łokas, 2010; Benatov et al., 2006). For example, with a sample of only 6 nearby relaxed Abell clusters, Łokas et al. (2006) constrains the anisotropy parameter to $-1.1 < \beta < 0.5$ at the 95% confidence level. Our results with 20 clusters basically reproduce this constraint on β.

Furthermore, we note that our treatment would not affect observables that are either first or second derivatives of the potential, such as Jeans mass analyses or inferences of X-ray masses. The reason for this is that the dominant term in equation 2.5 is the normalization constant $\Psi(r_{eq})$. The techniques that are affected by our theoretical expectations are those that directly deal with the escape velocity profile as such (or in other words, with the cluster's potential as inferred from dynamics). Therefore our analyses matters when the normalization of the potential matters. This is not the case for the two aforementioned methods nor for weak lensing masses. In short, cosmology matters for escape-velocity inferred masses, as shown in 3-dimensional ΛCDM simulation (Miller et al. (2016)), 2-dimensional simulations (Fig. 2.3), and real data (Fig. 2.5, black line).

One technique that directly deals with the escape velocity profile as such is the caustic technique. Hoekstra et al. (2015) has recently demonstrated that mass estimates by the caustic technique (see Rines et al. (2013)) are on average underestimated when compared to the weak lensing masses by $\sim 22\%$. If we drop the cosmological terms in our theoretical profile, the overall escape velocity profile would increase (as in Fig. 2.1). As such, in order to match this Einasto profile without the cosmological term, the Einasto qH^2 would always infer a higher mass. Interestingly, we find that $M_{200}(\text{Einasto } qH^2)/M_{200}(\text{Einasto}) = 1.22$, exactly reproducing Hoekstra et al. (2015)'s result. We note this as a possible explanation for this discrepancy and as a call to return to reflect upon the cosmological dependence of the escape velocity edges as already argued long ago by Kaiser (1986) and Regoes & Geller (1989b).

2.8 Summary

With archival data of just 20 galaxy clusters with extensive redshift information and weak lensing mass profile estimates we demonstrate the need to include a cosmological dependent term in the analytic model of the escape velocity profile of galaxy clusters. We conduct our analysis also utilizing ten sets of 20 synthetic galaxy clusters to study underlying systematics and projection effects. We find that our analytic formulation provides remarkable agreement with both sets of data.

More specifically, we leverage the complications involved in projecting the line-of-sight velocities related to to the anisotropy parameter (β) and utilize this information to quantify the necessity of including a cosmological term in our analytic theory.

We find that if we do not include a cosmological term in our analytic theory we infer velocity anisotropies that are inconsistent with both numerical results and observational data.

Throughout our analysis we picked a fiducial cosmology to probe our theoretical expectations and showed that there is a degeneracy between the velocity anisotropy parameter and cosmology. However, by independently inferring the anisotropy parameter, and combining this with the cosmology dependent Einasto qH^2 theoretical profiles, one can in principle constrain cosmology.

As such, we have briefly motivated the capacity for the escape velocity profile of galaxy clusters to become a novel probe of cosmology in the near future given its sensitivity to the physics of cosmic acceleration. What is required to realize this is the next generation of weak-lensing data for galaxy clusters as well as deep spectroscopic follow-up (e.g., the Dark Energy Survey (Diehl et al., 2014) and the Dark Energy Spectroscopic Instrument–DESI). Given that the data is not yet available, in Chapter IV we use the Fisher matrix formalism to derive constraint forecasts on general relativistic cosmologies with the escape velocity profile model presented in this chapter.

CHAPTER III

Cluster escape velocity profiles and the velocity anisotropy profile

3.1 Introduction

As demonstrated in Chapter II, we can utilize the cosmology-dependent escape velocity profile as a probe of cosmology only if we are able to either independently measure the cluster anisotropy parameter β for each of the clusters used. In this chapter we develop a novel approach to derive galaxy cluster anisotropy profiles for galaxy clusters independent of cosmology. We note that beyond the motivation to further develop our cosmological probe, the global galaxy cluster velocity anisotropy profile β is actually not yet well characterized nor broadly studied. In fact, what is presented in this chapter is the first attempt to derive velocity anisotropy profiles for a large cluster sample size ($N = 35$) utilizing joint dynamical and weak lensing data.

In general, β is defined in the following way (Binney & Tremaine, 1987),

$$\beta(r) = 1 - \frac{\sigma_t^2}{\sigma_r^2}, \tag{3.1}$$

where σ_t^2 and σ_t^2 signify the tangential and radial velocity dispersions, respectively, of galaxies at a given radial bin. As an example, in the case of a totally isotropic velocity distribution of the galaxies, Eq. 3.1 yields $\beta = 0$, whereas a totally radial velocity distribution yields $\beta = 1$. While the upper limit of the parameter is unity, the lower limit can in principle be $\beta = -\infty$. Values of β below 0 entail tangential galactic orbits.

Typically, inferring velocity anisotropy profiles follows the long tradition of studies that has modeled the galaxy cluster as a collisionless system described by the anisotropic Jeans equation (Binney & Tremaine, 1987; Binney & Mamon, 1982;

Solanes & Salvador-Sole, 1990),

$$\frac{d(\rho\sigma_r^2)}{dr} + \frac{2\beta\sigma_r^2\rho}{r} = -\rho\frac{d\phi}{dr}, \tag{3.2}$$

where the potential-density pair of the system is defined respectively by the quantities ϕ and ρ, and σ_r^2 represents the radial velocity dispersion of the tracers (in our case, galaxies).

In the Jeans equation, β is degenerate with the mass profile through both the density and the derivative of the potential. This is the so called "mass-anisotropy degeneracy" (Merritt, 1987). One obvious solution to this degeneracy is to attain an independently measured mass (Binney & Mamon, 1982; Solanes & Salvador-Sole, 1990). Previous work in this area has provided estimates for cluster anistropy profiles by using X-ray masses (Host et al., 2009; Hwang & Lee, 2008; Benatov et al., 2006). Other authors have attempted to break the mass-anisotropy degeneracy using just the dynamical information in the cluster phase-spaces (Wojtak & Łokas, 2010; Łokas et al., 2006; Biviano & Katgert, 2004). However, there are very few examples of higher precision measurements of the anisotropy profile using large samples of clusters (Host et al., 2009; Wojtak & Łokas, 2010).

Given the proliferation of data and techniques to characterize the mass profiles of galaxy clusters, various papers have focused on deriving $\beta(r)$ for individual clusters by combining mass profiles inferred through different techniques (Biviano et al., 2013; Aguerri et al., 2017; Annunziatella et al., 2016; Munari et al., 2014; Lemze et al., 2009). Most of these studies conclude that while the orbits of clustered galaxies are unlikely to be tangential, the overall scatter is often too large to determine either the degree of isotropy or radial anisotropy of galactic orbits that is expected from the results of N-body simulations – which tends to show only a weak radial anisotropy within the virial radius (Iannuzzi & Dolag, 2012; Lemze et al., 2009; Serra et al., 2011). In contrast to these individual cluster studies, we are more interested in deriving a "global" galaxy anisotropy profile from a relatively large sample size of clusters, in the spirit of work such as that of Wojtak & Łokas (2010), which derived velocity anisotropy profiles for 41 clusters.

In what follows, we derive an average anisotropy profile for 35 galaxy clusters. We follow the intuition of (but also take a different approach than) Natarajan & Kneib (1997)–a seminal paper that is the first to attempt to do a joint dynamics-weak lensing constraint of β using the Jeans equation. We carefully test our approach using synthetic clusters produced through the N-body Millennium simulations (Springel et al., 2005a). We then apply our new algorithm to archival data from 35 galaxy clusters with both weak lensing mass profiles and extensive spectroscopic coverage. In contrast to Natarajan & Kneib (1997), which largely focuses on characterizing the degree of anisotropy of the core of a single cluster, we derive profiles for our 35 clusters that extend out to one virial radii and also sidestep the complications of modelling galaxy cluster cores. In particular, we find that within 0.2 - 1 virial radii, the average galaxy cluster velocity anisotropy profile of the 35 clusters derived from archival data tends to be radially anisotropic with a small statistical scatter. In what follows, we attempt to address how these results compare to other derivations of β and discuss its implications. We highlight that this is the first attempt to derive a global β profile of galaxy clusters with joint weak lensing and dynamical data.

The outline this chapter is as follows: in Section 3.2 we describe the data we used to both test our approach in cosmological N-body simulations, as well as the joint weak lensing and spectroscopic archival data of the 35 galaxy clusters; in Section 3.3 we clarify the observables derived from the aforementioned data and then describe how they are used to derive β profiles in Section 3.4; Section 3.5 presents the results of our approach; lastly, in Section 3.6 we discuss our results in light of other derivations of β as well as the systematics affecting our probe. For the case of synthetic data (real data) we assume a flat ΛCDM cosmology with $\Omega_M = 0.25(0.3)$, $\Omega_\Lambda = 1 - \Omega_M$, and $H_0 = 100h$ km s^{-1} Mpc^{-1} with $h = 0.73(0.7)$.

3.2 Data

In this section we describe the synthetic data we used to test our approach with N-body simulations, and then describe the archival of the 35 galaxy clusters that contain both weak lensing and spectroscopic observations.

3.2.1 N-body simulations

We test our method on dark matter halos generated by the N-body cosmological simulations of the Millennium simulation (MS) (Springel et al., 2005a). In particular, we use the particle data from these simulations to measure the cluster Einasto density profiles. We treat these density profiles as the "weak lensing" data, since they trace the underlying matter distribution.

More specifically, we select 100 halos from the Millennium Simulation to test our approach. Our sample aims for fair cluster mass sampling over the range $\sim 10^{14} - 10^{15} M_\odot$. The average mass of our sample is $\langle M \rangle = 2.34 \times 10^{14} M_\odot$ and the average critical radius is $\langle r_{200} \rangle = 0.95$Mpc. We then use the semi-analytic galaxy catalogs from Guo et al. (2011b) to define our projected cluster radius/velocity phase-spaces. These phase-spaces typically contain between 100-200 galaxies within r_{200} and ± 3000km s^{-1}, which is similar to the observed data (see next sub-section). The volume around each halo is a cube with box length 60Mpch^{-1}. This box length is large enough to make line-of-sight projections to include realistic phase-space contamination from typical galaxy peculiar velocities (i.e., $\pm \sim 3000$ km s^{-1}). We calculate the line-of-sight velocity dispersions using 100 random orientations around each cluster. We then use these to measure the median line-of-sight velocities v_{los} as well as an error based on the 1σ scatter of the individual profiles. We explain this more thoroughly in the next sections.

3.2.2 Archival data

To derive the global β profile in real data we use data from 35 clusters found in the literature. To find the 35 archival data clusters we used the VizieR catalog (Ochsenbein et al., 2000) to search for redshifts of the galaxy clusters (Rines et al. (2013); Maurogordato et al. (2008); Owers et al. (2011b,c); Tyler et al. (2013); Girardi et al. (2008); Oemler et al. (2009); Agulli et al. (2016); Tran et al. (2007); Demarco et al. (2010); Lemze et al. (2013); Moran et al. (2007); Geller et al. (2014); Girardi et al. (2015); Edwards & Fadda (2011)) that also have weak lensing data (Hoekstra et al. (2015); Okabe & Umetsu (2008); Okabe et al. (2010); Okabe & Smith (2015); Umetsu et al. (2015); Cypriano et al. (2004); Pedersen & Dahle (2007); Medezinski et al. (2016); Foëx et al. (2012); Clowe et al. (2000); Jee et al. (2011); Smail et al. (1997)). We tabulate this joint dynamic-weak lensing dataset on Table 3.1. Note that while we cite the original papers, the weak lensing masses (and their respective errors) we use in our analysis were taken from the standardized Sereno (2015) meta catalog.

More specifically, we note that 10 clusters in our sample have $57 < N < 100$ galaxies while the remaining 25 clusters have more than 100 galaxies within r_{200} and within their escape velocity profile (v_{esc}). The mass range of the archival data lies between $4.1 \times 10^{14} M_{\odot}$ and $2.06 \times 10^{15} M_{\odot}$. Note that the meta catalog only lists masses inferred from NFW fits to weak lensing shear measurements. As is detailed in the next section, we transform the NFW fit parameters to those of the Einasto model.

Table 3.1: List of Galaxy Clusters and References

Cluster name[1]	Redshift	Weak lensing[2]	Galaxy redshifts
A1682	0.227	P07	Rines et al. '13
A1553	0.167	C04	Rines et al. '13
A1423	0.214	O15	Rines et al. '13
A2163	0.201	H15/R08	Maurogordato et al. '08
A2034	0.113	O08	Rines et al. '13
A2029	0.077	C04	Tyler et al. '13
A2009	0.152	O15	Rines et al. '13
A2219	0.226	O10/O15/A14	Rines et al. '13
A2744	0.306	M16	Owers et al. '11
A520	0.201	H15	Girardi et al. '08
A851	0.405	F12	Oemler et al. '09
A85	0.055	C04	Agulli et al. '16
A773	0.217	O15	Rines et al. '13
ZwCl3146	0.289	O15	Rines et al. '13
BLOXJ1056	0.831	CL00	Tran et al. '07
RXJ1720	0.160	O15	Owers et al. '11
RXJ0152	0.837	J11	Demarco et al. '10
RXCJ1504	0.217	O15	Rines et al. '13
A2111	0.229	H15	Rines et al. '13
A611	0.287	O10	Lemze et al. '13
ZwCl0024	0.395	S97	Moran et al. '07
A2259	0.161	H15	Rines et al. '13
A1246	0.192	H15	Rines et al. '13
A697	0.281	O10	Rines et al. '13
A1689	0.184	U15	Rines et al. '13
A1914	0.166	H15	Rines et al. '13
A1835	0.251	H15	Rines et al. '13
A267	0.229	O15	Rines et al. '13
A1763	0.231	H15	Rines et al. '13
A963	0.204	O15	Rines et al. '13
A383	0.189	O15	Geller et al. '14
A2142	0.090	O08	Owers et al. '11
RXCJ2129	0.234	O15	Rines et al. '13
MACS1206	0.440	F12	Girardi et al. '15
Coma	0.0231	H15	Edwards, Fadda'11

3.3 Theoretical Observables

Before we can derive β profiles for our set of both synthetic data and the 35 clusters, we extract both the dynamical data of clustered galaxies thorough their line-of-sight velocities as well as their respective cluster mass profiles. In the following two sub-sections we describe the relevant observables and other quantities that we use in our approach to derive β.

3.3.1 Galaxy line-of-sight velocity dispersion profiles

The redshifts of galaxies along a line-of-sight are used to generate the line-of-sight velocities vs. physical distance (v_{los} vs. r) "phase spaces." From these phase spaces we infer the line-of-sight velocity dispersion. In particular, for a given cluster, given some angular separation from the cluster center (θ) the line-of-sight (v_{los}) velocities at the cluster's redshift (z_c) can be inferred via,

$$v_{los} = c\frac{(z - z_c)}{(1 + z_c)}, \tag{3.3}$$

where c denominates the speed of light, and z is the redshift of the individual galaxies along the line-of-sight. Now, the physical distance from the cluster's center (r) can be inferred from the angular diameter distance (d_A) and the aforementioned angular separation (θ),

$$r = d_A(z)\theta = \left[\frac{1}{1+z}\frac{c}{H_0}\int_0^z \frac{dz'}{E(z')}\right]\theta, \tag{3.4}$$

where the cosmological evolution of the energy densities for the aforementioned ΛCDM cosmology is given by $E(z) = \sqrt{(1 - \Omega_M) + \Omega_M(1 + z)^3}$. Note that for the cluster center and cluster redshift z_c we use what has been specified for each respective cluster in the spectroscopic catalog described in the previous section.

Having created a phase space for a given cluster, we then calculate the velocity dispersion profile of the cluster. However, before we can do this we remove galaxies that may exist in our phase space simply because they are observed within our line-of-sight, but do not exist within the virial sphere of the cluster. If these "interloper" galaxies are not removed, the resulting velocity dispersion profiles will be biased. To do this, we apply the shifting-gapper technique of Gifford et al. (2013) (see further references about interloper removal techniques therein, as well as a detailed statistical and systematic analysis of this technique).

Having identified and removed interlopers from the cluster phase space, we bin the galaxies radially to calculate the line-of-sight velocity dispersion profile.

For each radial bin r, we then calculate the line-of-sight dispersion via the following robust estimator,

$$\sigma_{los}^2(r) = \sum_j \frac{\langle v_{los}(r_j)^2 \rangle}{N_{gal,j} - 1}, \tag{3.5}$$

where we sum over the number of galaxies $N_{gal,j}$ within a given radial bin r_j . We calculate the error on each radial bin via a bootstrapping re-sampling algorithm, and find that the error on any given radial bin is on average ~ 50 km s^{-1}.

Having calculated the line-of-sight velocity profile we then smooth them in order to be able to extrapolate beyond the measured values by fitting them with a simple power law, (Carlberg et al., 1997; Aguerri et al., 2017)

$$\sigma_f(r) = \sigma_{f,0}(1 + r)^p, \tag{3.6}$$

where the central projected velocity dispersion is given by $\sigma_{f,0}$ and p signifies the exponent.

For the case of the synthetic data we use a radial bin width of $\Delta r = 0.2$ Mpc and we fit equation 3.6 to the σ_{los} profiles for the radial range $0.1 \leq r \leq 1.5 r_{200}$ Mpc. We find that the fits match the measured v_{los} profiles with no bias and to high precision.

Clusters in the archival data are occasionally less well-sampled than in the simulation data. Therefore, we define the center of each radial bin after first ensuring that there is 20 galaxies within it. We take the mean radius of these twenty galaxies in each bin. As such, for a given cluster in the synthetic data, the radial bin width can range from $\Delta r \sim 0.1$ to 0.2 Mpc. Note that in contrast to the synthetic clusters, we fit Equation 3.6 over the radial range for all the data available, which varies in spatial extent depending on the cluster. We find that the averaged difference between the fits and the measured line-of-sight velocity profiles is $\langle \sigma_{los}^{fit} - \sigma_{los} \rangle \sim -43$ km s $^{-1}$. This bias is at about the level of the individual errors on the galaxy velocities. Note that this stipulates that, on average, our fits are slightly biased low compared to the noisy data. This effect is due to the bias-variance tradeoff and indicates that there is likely a better fitting function that could be applied. We also note that, as reported in Gifford & Miller (2013), improving the completeness of the cluster phase spaces would improve these fits. Nonetheless, we note that they are within the statistical error. We further discuss the implications of our σ_{los} fits on Section 3.6.

3.3.2 Galaxy cluster mass profiles

The other observable of interest is the mass profile of galaxy clusters. For the case of the N-body simulations we attain the parameters describing these profiles by fitting the dark matter halo with an Einasto profile. The Einasto representation of the dark matter halo density profile (Einasto, 1965) is a three parameter model (n, ρ_0, r_0) described by the following fitting formula for the density profile,

$$\rho(r) = \rho_0 \exp\left[-\left(\frac{r}{r_0}\right)^{1/n}\right]. \tag{3.7}$$

For the case of the archival data, however, we utilized the weak lensing parameters listed in the catalog for each respective cluster as described in the previous section (see Table 3.1). Because the vast majority of characterizations of galaxy cluster's density profiles are represented in terms of NFW fits, we fit the Einasto profile to the NFW density profile for each respective cluster in the radial range $0.05 \leq r \leq r_{200}$ Mpc and ensure that they fit to high precision within that radial range as expected by Sereno et al. (2016a). To do this, however, we must also use a mass-concentration relation from the cluster metacatalog, where the concentration (c_{200}) as a function of mass (M_{200}) and cluster redshift (z_c) is given by (Sereno, 2015),

$$c_{200}(M_{200}, z_c) = A_{200}\left(\frac{M_{200}}{M_{piv}}\right)^{B_{200}}(1+z_c)^{C_{200}}. \tag{3.8}$$

Where $A_{200} = 5.71$, $B_{200} = -0.084$, $C_{200} = -0.47$ and $M_{piv} = 2 \times 10^{12} h^{-1} M_{\odot}$. As usual, the quantities with subscript "200" are defined in terms of the radius r_{200} which is the distance at which the density enclosed within a sphere drops to 200 times the critical density in the Universe. The mass M_{200} is therefore the mass enclosed within that sphere, from which we can attain the corresponding concentration c_{200} via the relation shown above.

At this point it is important to highlight that β is correlated with the parameter γ (which quantifies the radial slope of the density profile of dark matter halos) and that the choice of density profile has some relation to the resulting β (Hansen, 2009). However, the reason that we pick an Einasto profile over the NFW density profile (as well as whether or not it makes any difference to our results) will be made clear in the following section – where we describe the particular method we utilize to derive velocity anisotropy profiles.

3.4 Deriving velocity anisotropy profiles

Our strategy to derive the velocity anisotropy profile β follows the long tradition of studies that has modeled the galaxy cluster as a collisionlesss system described by the anisotropic Jeans equation, reproduced here in Equation 3.2 (Binney & Tremaine, 1987; Binney & Mamon, 1982; Solanes & Salvador-Sole, 1990)

If the mass of the system can be independently inferred, the potential-density pair can be defined and in combination with a second equation that relates the velocity dispersion of the system to its potential-density pair, the anisotropy profile β can be derived by solving Eq. 3.2. For instance, Natarajan & Kneib (1997), following Binney & Mamon (1982), reconstructs the radial velocity dispersion and use a weak lensing inference of the potential-density pair to derive β for a single cluster.

In contrast to this approach, we use a simple relation that relates the radial velocity dispersion to the line-of-sight velocity dispersion. In particular, if cluster rotation is negligible, we have, $\langle v_\theta^2 \rangle = \langle v_\phi^2 \rangle = \langle v_{los}^2 \rangle$. And so from β of Eq. 3.1, with $\sigma_t^2 = \frac{1}{2}\left(\sigma_\theta^2 + \sigma_\phi^2\right)$, we have that,

$$\langle v_r^2 \rangle = \frac{\langle v_{los}^2 \rangle}{1-\beta}. \tag{3.9}$$

This relation is utilized in the quite successful caustic mass technique (see Diaferio & Geller (1997a); Diaferio (1999); Serra et al. (2011); Geller et al. (2013)). For now, we take it as a given and we explore its validity at the end of this section.

In galaxy clusters, $\langle v_r^2 \rangle = \sigma_r^2$, and so we have that with Eq. 3.9, the Jeans equation (Eq. 3.2) now becomes,

$$\frac{d}{dr}\left(\rho \frac{\langle v_{los}^2 \rangle}{1-\beta}\right) + \frac{2\beta\rho}{r}\left(\frac{\langle v_{los}^2 \rangle}{1-\beta}\right) = -\rho \frac{d\phi}{dr}. \tag{3.10}$$

At first sight, solving this highly nonlinear differential equation for β seems like a daunting task. However, after a bit of algebra we can re-write Eq. 3.10 in the following way,

$$\frac{d\beta}{dr} + (1-\beta)X + (1-\beta)^2 Y + \beta(1-\beta)Z = 0, \tag{3.11}$$

where we have used the following redefinitions,

$$\begin{aligned} X \equiv & \frac{1}{(\rho\sigma_{los}^2)}\frac{d(\rho\sigma_{los}^2)}{dr}, \\ Y \equiv & \frac{1}{\sigma_{los}^2}\frac{d\phi}{dr}, \\ Z \equiv & \frac{2}{r}. \end{aligned} \tag{3.12}$$

Now, redefining some variables again, $u \equiv 1 - \beta$, we can re-write the Eq. 3.11 in the following form,

$$\frac{du}{dr} + P(r)u - Q(r)u^2 = 0. \tag{3.13}$$

Where we have defined,

$$\begin{aligned} P(r) \equiv & -X - Z, \\ Q(r) \equiv & Y - Z. \end{aligned} \tag{3.14}$$

The redefinitions and variable changes have allowed us to recast the Jeans equation (Eq. 3.10) as a Bernoulli differential equation (Eq. 3.13) which has a well-known analytic solution.

In particular, the form of the differential equation above is exactly that of the Bernoulli differential equation with $a = 2$,

$$\frac{dy}{dx} + p(x)y = q(x)y^a \tag{3.15}$$

Which for $a \neq 1$ has the general solution,

$$y = \left[\frac{(1-n)\int e^{(1-a)\int p(x)dx}q(x)dx + C_1}{e^{(1-a)\int p(x)dx}}\right]^{1/(1-a)}. \tag{3.16}$$

So for our Jeans equation, since $a = 2$, and using our function definitions,

$$\beta(r) = 1 - \left[\frac{e^{-\int P(r)dr}}{-\int e^{-\int P(r)dr}Q(r)dr + C_1}\right], \tag{3.17}$$

where the numerator is the integrating factor and the integral in the exponent is given by,

$$\begin{aligned}\int P(r)dr =& -\int \left[\frac{1}{(\rho\sigma_{los}^2)}\frac{d(\rho\sigma_{los}^2)}{dr}+\frac{2}{r}\right]dr \\ =& -\int \frac{1}{(\rho\sigma_{los}^2)}\frac{d(\rho\sigma_{los}^2)}{dr}dr - \int \frac{2}{r}dr \\ =& -\left[\ln(\rho\sigma_{los}^2)+2\ln(r)\right] \\ =& -\ln(\rho\sigma_{los}^2 r^2) - C_p.\end{aligned} \tag{3.18}$$

Simplifying,

$$\begin{aligned}e^{-\int P(r)dr} =& e^{\ln(\rho\sigma_{los}^2 r^2)+C_p}. \\ =& A_p\rho\sigma_{los}^2 r^2\end{aligned} \tag{3.19}$$

Putting in the analytic solution to the integrating factor ,

$$\beta(r) = 1 - \left[\frac{A_p\rho\sigma_{los}^2 r^2}{-\int A_p\rho\sigma_{los}^2 r^2 Q(r)dr}\right]. \tag{3.20}$$

Canceling A_p, we finally have,

$$\beta(r) = 1 - \frac{\rho\sigma_{los}^2 r^2}{I_1 - I_2}. \tag{3.21}$$

Where the integrals are given by,

$$\begin{aligned}I_1(r) =& \int_{r_1}^{r} 2\rho\sigma_{los}^2 R dR, \\ I_2(r) =& \int_{r_1}^{r} \rho\frac{d\phi}{dR}R^2 dR,\end{aligned} \tag{3.22}$$

and where the lower integration limit $r_1 = 0.05$ Mpc. We explain the reason choosing this integration limit below.

As such, the radial anisotropy profile for a given cluster can be attained with Eqs. 3.21-3.22 for an independently inferred mass profile which determines the potential-density pair (that is, ϕ and ρ, respectively) and a measurement of the line-of-sight velocity profile of galaxies (σ_{los}).

As anticipated in the previous section, for the potential-density pair we pick the Einasto model. From the Einasto density profile (Eq. 3.7) we can derive the gravitational potential ϕ using the integral form of the Poisson equation (Retana-Montenegro et al., 2012),

$$\phi(r) = -\frac{\mathrm{GM}}{r}\left[1 - \frac{\Gamma\big(3n, \left(\frac{r}{r_0}\right)^{1/n}\big)}{\Gamma(3n)} + \frac{r}{r_0}\frac{\Gamma\big(2n, \left(\frac{r}{r_0}\right)^{1/n}\big)}{\Gamma(3n)}\right]. \tag{3.23}$$

Note that we calculate the derivative of ϕ in Eqs. 3.21-3.22 numerically. For more specifics on the definition of the Einasto potential see Chapter II.

At this point it is important to clarify the reason we chose to use an Einasto rather than an NFW potential-density pair in our analysis and how this relates to why we pick $r_1 = 0.05$ Mpc.

As shown in both cosmological N-body simulations (Miller et al., 2016) and observational data (Stark et al., 2016) the gravitational potential inferred from the NFW density profile yields a profile that is biased high from what is expected. In particular, the NFW density is significantly steeper than the Einasto density as $r \to 0$, which also means that the potential (ϕ) and its derivative ($d\phi/dr$) are higher for the NFW model. As such, when Eqs. 3.21-3.22 are integrated, we expect to see a difference between the NFW and Einasto profiles in the resulting β. Because we want our results to be as model-independent as possible, and because there is still considerable uncertainty in the modeling of galaxy cluster cores, the lower limit (r_1) of the integrals in Eq. 3.22 is chosen to be 0.05 Mpc. Moreover, note that for any given cluster we actually extrapolate the integrand functions out to 30 Mpc. But given that we cut off the derived β's at r_{200}, where the Einasto and NFW models agree with each other, this upper limit to the extrapolated radial range does not make a difference to our results. As such when the radial range used in the integrands of Eq. 3.22 is $0.05 \leq r \leq r_{200}$ Mpc, we see no significant difference between the Einasto and NFW models. This is due to the fact that the major difference between these models arises from the modeling of the core of galaxy clusters and its outskirts (that is, $r > r_{200}$). While we find the model dependence of the inferred β to be a crucial matter that merits further study, we relegate a more thorough analysis of it to a future attempt.

Secondly, we also want to note that in contrast to the results of Miller et al. (2016) and Stark et al. (2016), our Jeans equation is not dependent on cosmology. The reason for this is that while those two studies work with observables that are directly proportional to the potential (and must therefore take into account the specific normalization of the potential) the Jeans equation is only dependent on the spatial derivative of the potential for which the effects of the expansion of the Universe can be neglected. This is known as the "Jeans swindle" and has been formally justified in Falco et al. (2013).

Thirdly, another important aspect to highlight about our approach is that unlike the common and widely-used method developed in Solanes & Salvador-Sole (1990), our approach allows us to straightforwardly calculate the uncertainties of β. As noted by both Biviano et al. (2013) and Biviano & Katgert (2004), the derived uncertainties on β are very difficult to calculate with the approach of Solanes & Salvador-Sole (1990) because it works through a complicated set of coupled differential equations. This is not the case for our method given that we solve for β analytically by recasting it as a Bernoulli differential equation. In particular, for our simulated clusters, we take into account the uncertainty in measuring the line-of-sight velocities simply by creating an array of β's which correspond the 1σ errors on the measured line-of-sight velocity profiles (σ_{los}). For our real clusters, we consider both the error on the inferred σ_{los} profiles as well as the error on the mass profiles (which propagates to $d\phi/dr$ and ρ) simply by recalculating β for the range of uncertainty in either the mass and the line-of-sight dispersion profiles.

Lastly, as mentioned before, our approach is based on the relation shown in Eq. 3.9 which is utilized in the well-established caustic mass technique (Diaferio & Geller, 1997a; Diaferio, 1999; Serra et al., 2011; Geller et al., 2013). Nonetheless, we want to confirm the validity of Eq. 3.9. In particular, we want to analyse how β^{los} compares to the directly measured β from galaxies in simulated halos via Eq. 3.1, that is, the "true" β. To that end, we define Eq. 3.9 to be the "line-of-sight" velocity anisotropy profile (β^{los}),

$$\beta^{los} = 1 - \frac{\sigma_{los}^2}{\sigma_r^2}. \tag{3.24}$$

The difference between β^{los} and the "true" β is shown in Fig. 3.1. In the top-panel, we show that while on average the assumption made by in the caustic technique yields a null bias, the relation between the line-of-sight velocity dispersion (σ_{los}) and the transversal velocity dispersion (σ_t) depends on radius. We note that, while this systematic is still within our overall uncertainties, it must be corrected for. As shown in the bottom-panel of the same figure, if this systematic is not corrected for, our technique can yield an average β that is higher from the true value by a difference of 0.14 at r_{200}. We also note that while this systematic is important, it still lies within our current uncertainties in the measurement of σ_{los}, which are about 50 km s^{-1} (see the horizontal dashed lines on the top panel of Fig. 3.1).

Having checked the validity of our presuppositions and having specified our approach to derive β profiles, we now describe our results.

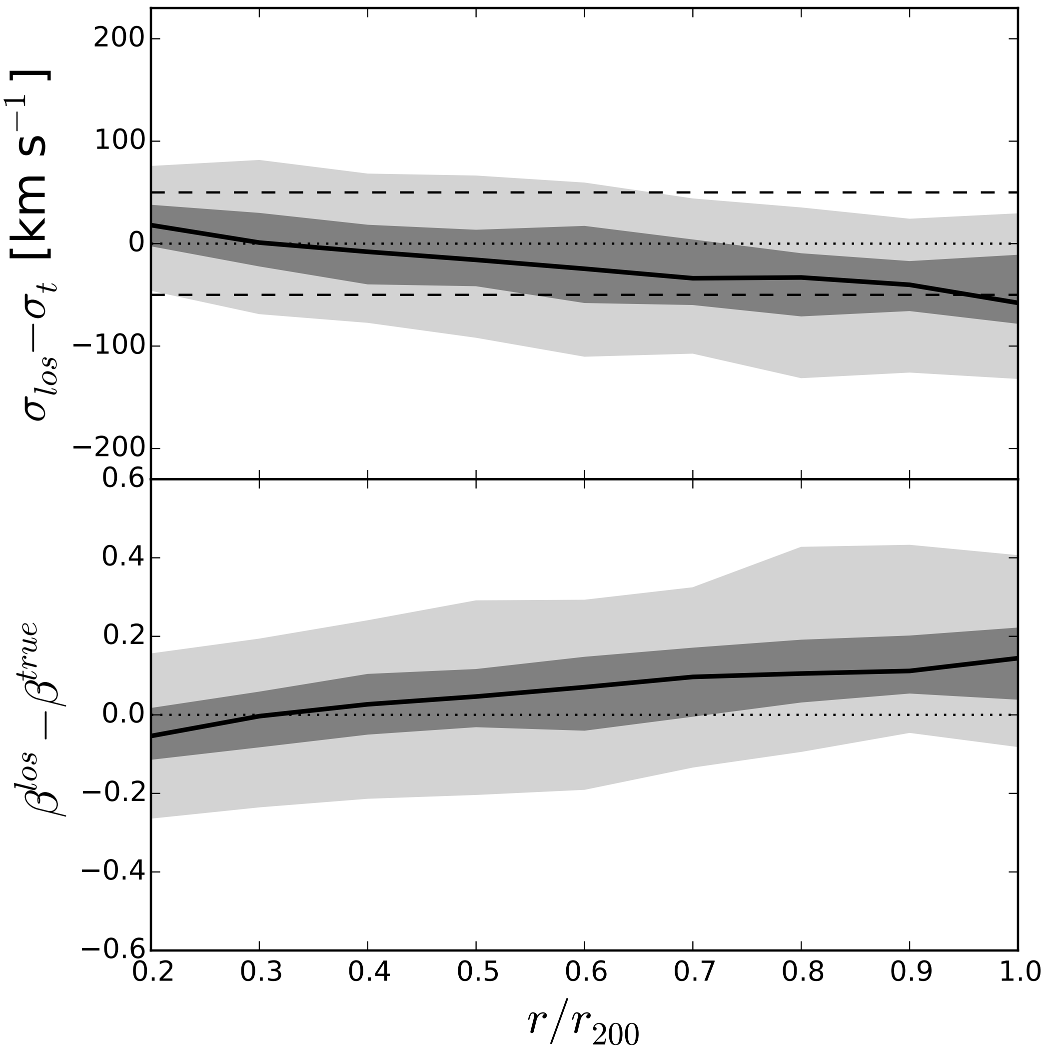

Figure 3.1: *Top panel:* Difference between the measured line-of-sight velocity dispersion profile (σ_{los}) and the tangential velocity dispersion (σ_t) for the 100 synthetic clusters from cosmological N-body simulations. The horizontal dashed lines represent the 1σ error on our measurement of σ_{los}, ~ 50 km s^{-1}. *Bottom panel:* Difference between the "true" β measured via Eq. 3.1 and the "line-of-sight" β (Eq. 3.24). See text for details. The black line shows the median (50th percentile) and the dark (light) gray bands represents the 68th (90th) percentile. The small bias in σ_{los} leads to a systematic bias in the inferred β.

3.5 Results

Using Eq. 3.21 (see Section 3.4) we test our approach with the 100 synthetic clusters from cosmological N-body simulations and then move on to derive β profiles for archival data of 35 galaxy clusters.

3.5.1 Synthetic data results

The top panel of Figure 3.2 shows our results for the 100 synthetic clusters using Equation 3.21. The bands represent the 68th (dark gray) and 90th (light gray) percentiles of the sample. The median (black line) hovers around $\beta \sim 0.1$. In the lower panel of Figure 3.2, we plot up the difference between β as estimated through our approach (Eq. 3.21) and the "true" β estimated directly from Eq. 3.1 (solid line). Figure 3.2 demonstrates that our approach works with accuracy and precision once radially averaged, $\langle \beta - \beta^{true} \rangle \sim 0$. The dashed black line in the bottom-panel shows the resulting difference after having corrected for the systematic shown in the bottom panel of Figure 3.1. This test also allows us to set a baseline for the systematic uncertainty, which incorporates both the observational systematic (see Figure 3.1) as well as any additional systematic errors introduced by the technique itself. Using Figure 3.1, we define the overall systematic error on the mean measurement of $\beta(r)$ to be $\sim \pm 0.15$, which is the maximum deviation between our inference of $\beta(r)$ and the true $\beta(r)$.

We note that the result of Fig. 3.2 does not take into account the uncertainty on σ_{los} nor the weak lensing inferred density and potential that exist in the real data. When doing so, one can find β profiles that occasionally exceed the physical condition from Equation 3.1 that $\beta < 1$. This is due to the fact that while the integrals of Equation 3.22 are well-behaved in the radial range discussed in the previous section, the solutions to Eq. 3.21 can still yield non-physical results for any given combination of mass (ρ and $d\phi/dr$) and dynamics (σ_{los}). That is, for some clusters, there is a combination of dynamics and weak lensing that yields a β profile that is unphysical within the uncertainties on σ_{los} and the weak lensing mass profile estimates. In particular, the only case which can yield a non-physical result (namely, $\beta > 1$) occurs whenever $I_1 > I_2$ at some given radius. As such, when we include errors on the line-of-sight dispersions and the weak lensing masses, and in contrast to what is shown on Figure 3.2, we require that the solutions yield physical results ($\beta < 1$). Specifically, we do not use β profiles that yield $\beta > 1$ within the virial sphere (that is, if $\beta(r \leq r_{200}) > 1$).

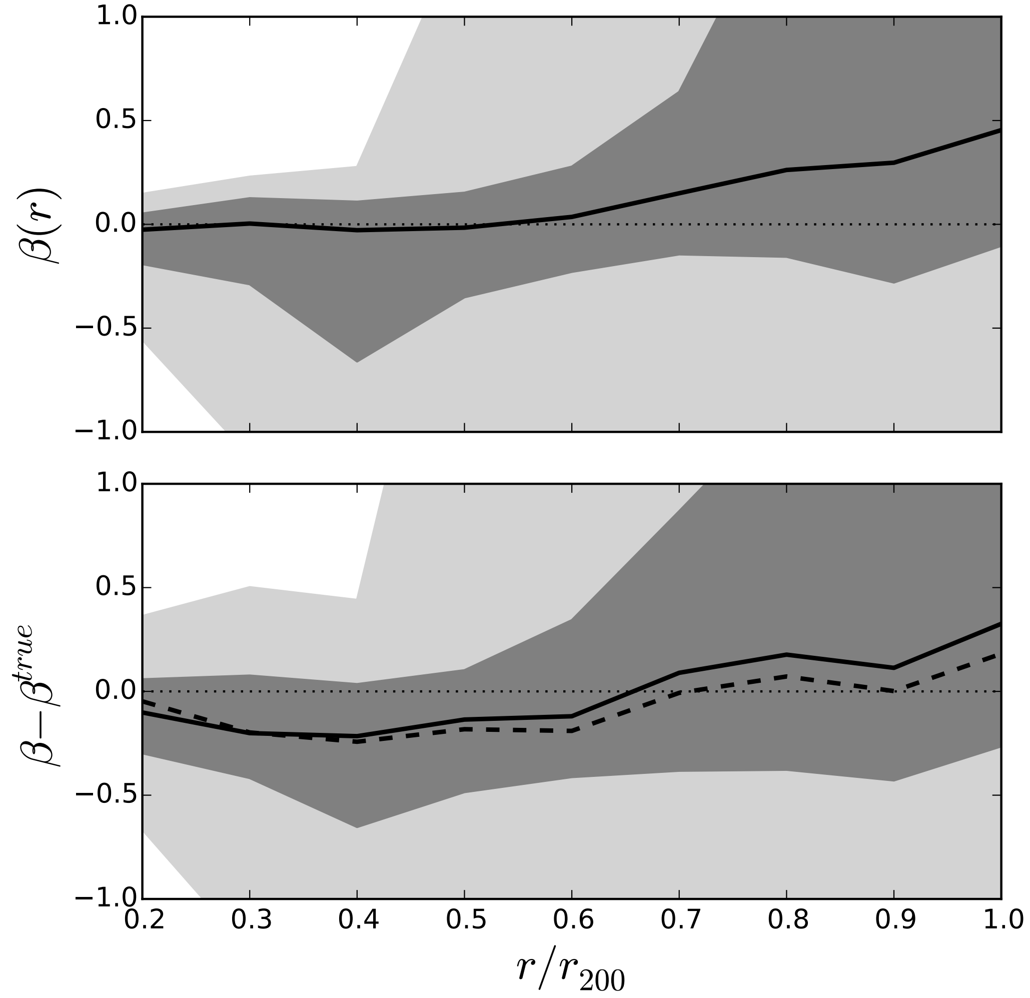

Figure 3.2: Results for the sample of 100 synthetic clusters from cosmological N-body simulations. *Top panel:* median (black line) with 68% and 90% percentile bands (dark and light gray, respectively). β is calculated with Equation 3.21 (see Section 3.4) and the resulting median is $\beta \sim 0.1$. *Bottom panel:* The difference, $(\beta - \beta^{true})$, between β as calculated with our approach and the "true" anisotropy parameter (β^{true}) calculated directly from the simulated galaxies via Eq. 3.1. The dark and light gray bands represent the same percentiles as those shown in the top panel. Note that the fractional difference between the "true" β and our inference is about zero.

3.5.2 Archival data cluster results

Having shown our approach to derive β works well in N-body simulations, and in particular, that it allows us to recover the true β to within ±0.15, we now derive the β profiles for the 35 clusters from the archival data.

In Fig. 3.3 we plot the weighted average of the 35 β profiles. More specifically, we take the average β at each radial bin, now divided in increments of $\Delta(r/r200) = 0.1$, by weighing the individual cluster profiles-all of which have different uncertainties at a given radii incurred from both their respective line-of-sight velocity dispersion profile and their mass profile uncertainties. The result is shown in the black dots with the 1σ error on the mean in Fig. 3.3. The gray triangles are the resulting weighted average (and respective 1σ error on the mean) when we correct for the systematic shown in Fig. 3.2 by subtracting off the difference (see bottom-panel of that same figure) from our weighted average. We note that the resulting weighted average after this systematic is included is well within the 1σ error.

The radially averaged β, shown with black dots in Fig. 3.3, yields a global value of $\langle\beta\rangle = 0.35 \pm 0.28$. The grey triangles in Fig. 3.3, yield a global value of $\langle\beta\rangle = 0.26$. These results imply that the observed velocity anisotropy profile of galaxy clusters is radially anisotropic. We discuss the implications of this result and compare it to other studies in the next section.

3.6 Discussion and Summary

The goal of this work is to constrain the average radial anistropy profile of clusters, $\langle\beta(r)\rangle$, using a large set of clusters with combined weak lensing and dynamical phase space data. In what follows we compare our results to other numerical studies as well as other observational data results.

Individually, many of the clusters have large errors in their inferred $\beta(r)$ profiles. However, there are a few clusters with well-constrained mass profiles and well-sampled phase spaces which also have previously published anisotropy profiles. As such, we compare our results for these clusters. In Figure 3.4, we plot four of these cluster β profiles as well as the profiles derived by Biviano et al. (2013) (upper-left panel), Aguerri et al. (2017) (upper-right panel), Lemze et al. (2009) (lower-right panel) and Host et al. (2009) (lower-left panel). All of these papers model the relation between dynamics, anisotropy, and the mass of galaxy clusters via the Jeans equation, although they utilize different methods to estimate the mass profile. For instance, Biviano et al. (2013); Aguerri et al. (2017); Lemze et al. (2009) all combine different mass

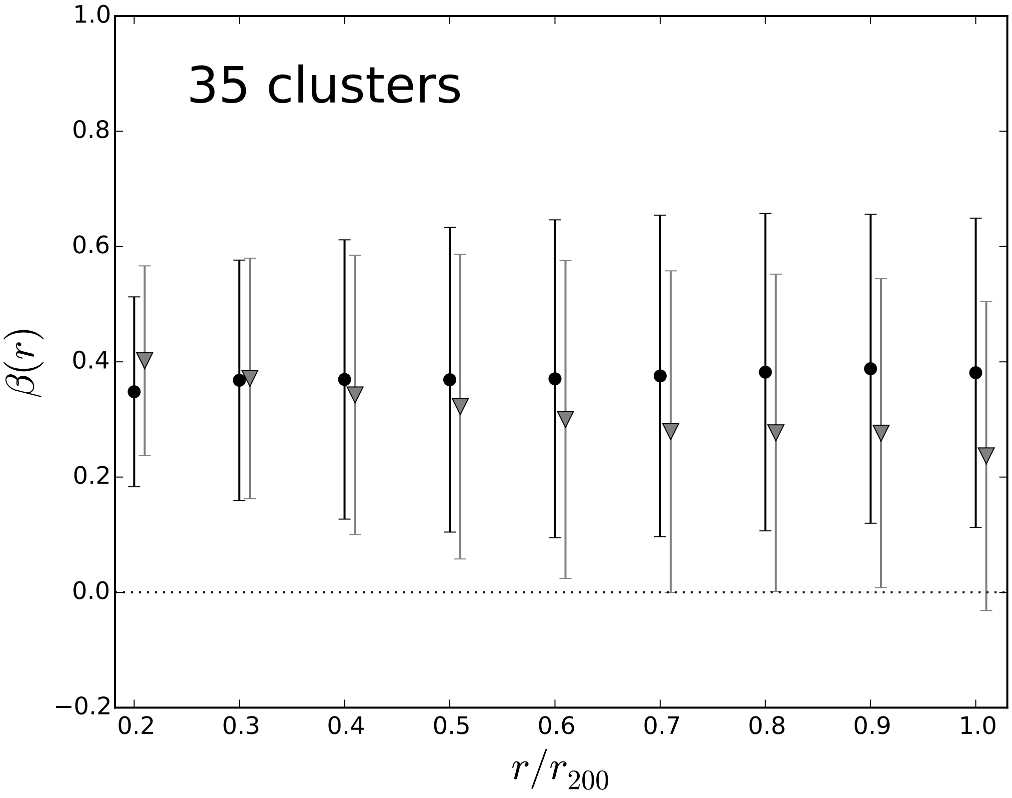

Figure 3.3: Resulting β profile for the 35 clusters of the archival data. The black dots are the weighted mean of each individual profile calculated with Eq. 3.21 (see Section 3.4) and the error is the 1σ uncertainty on the weighted mean. Note that each individual profile that is averaged here contains both the uncertainty in mass and line-of-sight velocity dispersion. The global value of β averaged between 0.2 and r_{200} is $\langle\beta(0.2 \leq r/r_{200} \leq 1)\rangle = 0.35 \pm 0.28$. This means that the galactic orbits are mostly radially anisotropic. The gray triangles are the result of correcting for the systematic shown in the bottom-panel of Fig. 3.1. We note that the overall effect still produces a result that lies within our 1σ error. Note that we have slightly shifted the gray triangles to higher radii simply to make the plot legible.

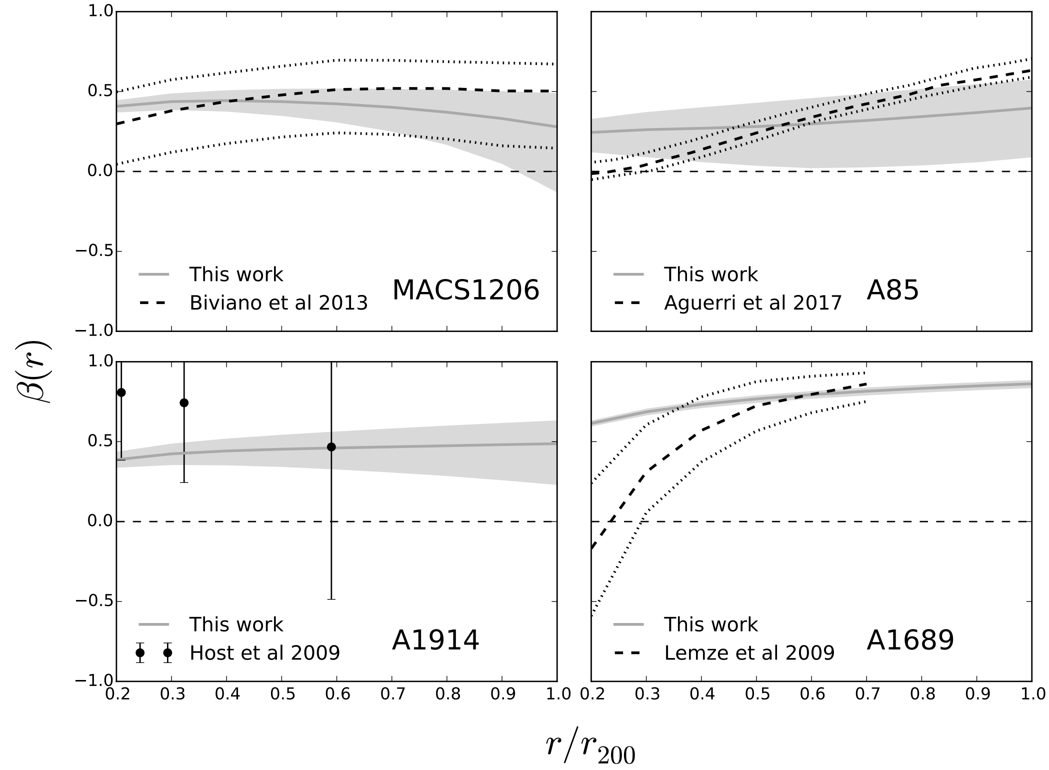

Figure 3.4: Comparison of 4 of the 35 individual β profiles with results from the literature. For all the panels, the gray band represents the 68th percentile error on β from both the uncertainty in the weak lensing mass profiles as well as the uncertainty in the line-of-sight velocity dispersion profiles. See text for details.

profile estimates, while Host et al. (2009) exclusively uses X-ray mass profiles. For all cases, in Fig. 3.4, the β we derived is shown in a gray band that represents the 68th percentile uncertainty that takes into account the uncertainty in both the line-of-sight velocity dispersion profile and the weak lensing mass profile of each respective cluster. In black (in dots or lines) we show either the median or average along with the 1σ error on β from each paper just cited. Note that in all cases our results agree, within respective uncertainties, with the previously published results. That is, galaxy orbits tend to be more radially anisotropic the farther away from the core of the cluster we go. However, our results seem to disagree with both Lemze et al. (2009)'s and Aguerri et al. (2017)'s results at smaller radii. In particular, our profiles of A1698 and A85 do not become isotropic as quickly as expected by these two other results.

For the case of A1689, we note that Lemze et al. (2009) uses a very high concentration ($c_{200} > 10$), which is $\sim$3.3 times larger than the concentration we use. The relation between concentration and β was studied in Wojtak & Łokas (2010). Their conclusion is the same as ours: a lower concentration yields a higher β.

Now, for the case of A85, while we use a very similar mass and concentration as what is used in Aguerri et al. (2017), we find that the central velocity dispersion parameter we fit is smaller than what is found by Aguerri et al. (2017) using all galaxies (that is, as opposed to using cuts in color or luminosity which can also bias the calculated line-of-sight of sight velocity dispersion). Note that a lower line-of-sight dispersion also yields a higher β. We want to highlight, however, that our β profile of A85 agrees with what is derived by Hwang & Lee (2008) (see Fig. 19, top-left panel for cluster A85, within r_{200}) but we do not overplot their results because their scatter is too large.

In Figure 3.5, we compare our radially averaged anisotropy profile to other average profiles from the literature. In this case, we only show the version that has not been corrected for the systematic bias identified using the simulations (i.e., we show the black dots from Figure 3.3). We only compare our results with previously published average profiles of β based on samples of clusters (i.e., not individual systems). We also compare our resulting β with the Millennium simulation results of Iannuzzi & Dolag (2012). Note that we do not compare our results with the work of authors who assume a constant β or specify a β only for a specific class of galaxies (such as that of Biviano & Katgert (2004)).

Our average radial anisotropy profile agrees well with the average profile of 16 clusters derived by Host et al. (2009) (see Fig. 7 of that paper). In particular, Host et al. (2009) also find a median value of β that implies radial anisotropy, such that

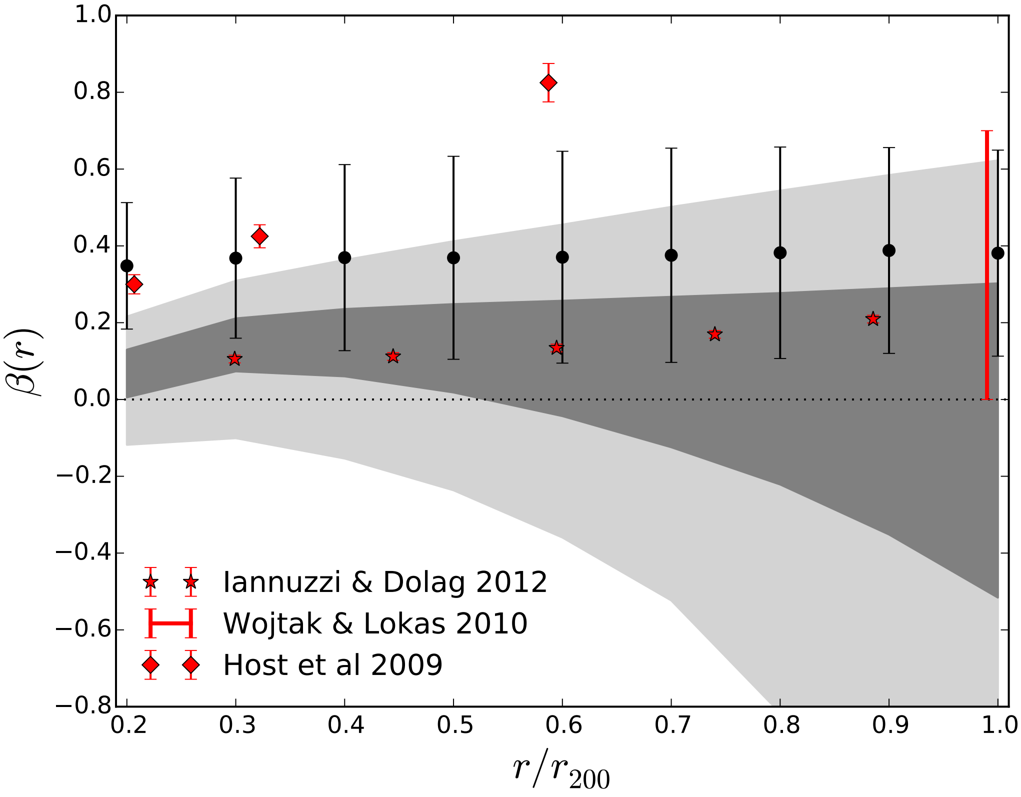

Figure 3.5: Comparison between β profiles from the literature and our work. The β calculated with Equation 3.21 (see Section 3.4) from 100 N-body simulated clusters is shown in light/dark gray bands and the β from the 35 archival data clusters is shown with black dots (same as in Fig. 3.3). In contrast to those of Fig. 3.2, the synthetic cluster results (grey bands) now take into account the uncertainty in the line-of-sight velocities as well as consider only physical results ($\beta \leq 1$). In red diamonds, we show the results of the median and 1σ error on β calculated for 16 clusters by Host et al. (2009). In the red vertical line, we show the range calculated by Wojtak & Łokas (2010) for their low concentration sample (about 30 clusters) at the virial radius. Lastly, the red stars are the averaged β for 1000 simulated clusters by Iannuzzi & Dolag (2012). Note that the 1σ error for the Iannuzzi & Dolag (2012) result is too small to show.

$\beta(r/r_{200} \geq 0.2) > 0.3$. We overplot the median β calculated by Host et al. (2009) in red diamonds, alongside our results, on Fig. 3.5.

Also, while Wojtak & Łokas (2010) does not show their radial β profiles, if we compare their calculated β's at the virial radius for their low concentration sample (see their Figure 7, for the case $c < 7$), their sample also implies radial infall at the virial radius. Taking that the virial radius is close to r_{200} ($r_{vir} \sim r_{200}$), we plot the range of β reported for their low concentration sample (about 30 clusters) in Fig. 3.5 (see red vertical line).

We also compare our results with our aforementioned 100 synthetic clusters from N-body simulations, also shown in Fig. 3.5. In particular, in contrast to the results of Fig. 3.2, we now consider the uncertainties in the measured σ_{los} (and its fits) from the synthetic cluster sample which is shown in the light gray (dark grey) bands of Fig. 3.5 which represent the 68th (90th) percentiles. Finally, we make a further comparison with simulations by comparing to the independent analysis of the β profile (from the 3D data) measured by Iannuzzi & Dolag (2012), who uses 1000 synthetic galaxy clusters. They find $\langle\beta\rangle = 0.253 \pm 0.01$ (their profile is shown with red stars in Figure 3.5). Note that we find that our simulation results (shown in the gray bands) agree well with the simulation results of Iannuzzi & Dolag (2012).

Considering that we are using the same method for both the data and the simulations, we find good agreement after we allow for systematic errors in the data. We note that the synthetic cluster sample is much lower in redshift than the real data sample. More specifically, the synthetic sample has a redshift range that is $z_c \leq 0.15$, whereas the cluster redshifts for the real data is $\langle z_c\rangle = 0.25$. As investigated in N-body simulations by Iannuzzi & Dolag (2012), we do not expect an appreciable redshift evolution of the global β parameter. We also note that our sample of 35 real data clusters have an average mass that is 4.4 times higher than the average mass of the 100 synthetic clusters. Recalling the negative correlation between mass and concentration, we might expect that a lower concentration (higher mass) yield a higher β for the data compared to the simulations. Also, recall that our fits to the line-of-sight velocity dispersion profiles are biased low with respect to the measured profile by ~ 43 km s^{-1}, which would bias our β's high.

Finally, the extrapolation of functions such as σ_{los} and the density profiles well into the core and the outskirts of galaxy clusters is definitely a weakness in this technique and others like it which depend on integration over the entire radial profiles of clusters (i.e., most Jeans-like analyses). We attempted to mitigate the effects of uncertainties in the cores of the clusters by integrating from 0.05 Mpc outward. However, this deserves further study. Furthermore, better fitting functions for σ_{los} as well as better-sampled clusters also yield better fits to the line-of-sight velocity dispersion. This could partially explain why the 35 real clusters sit on the upper end of the simulation results (compare black dots and gray bands in Fig. 3.5). Nonetheless, we emphasize that this slight disagreement is within the total systematic and statistical error we estimate.

Our work highlights a new advance in the measure of the velocity anisotropy of galaxy clusters. First, we develop a novel technique to combine the weak lensing mass information about the cluster mass profile with the observed line-of-sight velocity dispersion profile. Second, we test the accuracy and precision of this technique to realistic simulations, where the phase space data are projected onto the line-of-sight. Finally, we apply the technique to a sample of tens of clusters that have the required data. We find that within observed errors, the simulations and the data agree quite well. In particular, we find that the cluster velocity anistropy profile is flat with a value $\langle\beta\rangle = 0.35 \pm 0.28$ (stat) ± 0.15 (sys) implying that galactic orbits tend to be radially anisotropic.

CHAPTER IV

Cluster escape velocity profiles as a cosmological probe

4.1 Introduction

Following Shectman (1982), Regoes & Geller (1989a) and Regoes (1996) but also deviating significantly from their approach, Stark et al. (2016) (presented here in Chapter II) demonstrated the necessity to include a cosmological term to describe the escape velocity profile of galaxy clusters as inferred from their projected phase spaces. In particular, Stark et al. (2016) presented an analytic model based on the Poisson equation that can reproduce the projected escape velocity profiles of galaxy clusters as measured from their phase spaces. The analytical escape velocity profile prediction requires a known mass profile and a known velocity anisotropy profile $\beta(r)$. Given these and the cosmological parameters, the analytical escape velocity edge has been shown to match expectations to high precision and accuracy using N-body simulations (Miller et al., 2016).

If both weak lensing mass estimates and a measurement of β can be inferred for a galaxy cluster, we can turn this around and through analytic theory constrain cosmology by measuring edges of clusters through their phase spaces (see Diaferio & Geller (1997b); Serra et al. (2011); Geller et al. (2013); Lemze et al. (2009); Miller et al. (2016) for the various methods utilized to estimate the escape velocity "edge" from the phase space of galaxy clusters). The former can be attained from lensing shear measurements of galaxies, and the latter can be inferred from methods such as the one developed in Chapter III of this dissertation.

However, while Stark et al. (2016) demonstrated the necessity to include a cosmological and redshift-evolving term in the escape velocity profile of clusters, it did not quantify the precision with which one can constrain cosmological parameters with this observable. This is the task that this chapter takes on.

This chapter is organized as follows: in Section 4.2 we describe the theoretical observable we work with – the redshift-evolving and cosmology dependent escape velocity profile of galaxy clusters. In Section 4.3 we detail how we use the Fisher matrix formalism to quantify how well this observable can constrain cosmology given current and future systematic errors. We present the results of this analysis in Section 4.4. In Section 4.5 we present observational strategies that may be utilized to optimize cosmological constraints. In Section 4.6 we discuss our observable in relation to other probes and speculate as to how we may improve constraints in the future through joint likelihood analyses. We conclude and provide ways of extending our work in Section 4.7. In Appendix A we derive the cosmological quantities used in this chapter. The Appendices B and C detail the construction of our Fisher matrix. Lastly, in Appendix D we study the covariance of the weak lensing mass prior with cosmology.

4.2 Theoretical observable

The theoretical observable quantity we work with throughout this chapter is the projected escape velocity radial profile of galaxy clusters. Observationally, the escape velocity profile of a cluster is inferred from the phase space (v_{los} vs r space) of the cluster. More specifically, the line of sight galaxy velocity (v_{los}) vs. physical distance (r) space is constructed by measuring the redshifts of cluster galaxies (z) of a cluster at a redshift z_c and then converting them to velocities via,

$$v_{los}(r) = c\frac{(z - z_c)}{(1 + z_c)}, \tag{4.1}$$

where c is the speed of light. The physical distance from the cluster's center (r) is inferred from the angular diameter distance (d_A) and the measured angular separation (θ),

$$r = d_A(z)\theta = \left[\frac{1}{1+z}\frac{cH_0^{-1}}{\sqrt{\Omega_K}}\sin\left(\sqrt{\Omega_K}\int_0^z \frac{dz'}{E(z')}\right)\right]\theta. \tag{4.2}$$

H_0 is the Hubble constant and the redshift evolving function $E(z)$ is detailed in Eq. 4.10 below. Note that $\sin(x)$ (the non-flat closed universe case) becomes x for the flat universe case. Also detailed below is the parameter Ω_K which quantifies the openness or closedness of the universe. The escape velocity profile can then be inferred from this phase space through various techniques (see Diaferio & Geller (1997b); Serra et al. (2011); Geller et al. (2013); Lemze et al. (2009); Miller et al. (2016)).

This phase space inferred escape velocity profile can be modeled with a function of the mass distribution of a specific cluster as specified by its gravitational potential (in our case we use the Einasto profile with three free parameters: $\alpha, r_{-2}, \rho_{-2}$; see Eq. 4.6 below), and the anisotropy parameter (β) of that specific cluster (which allows us to take into account projection effects). As mentioned in the introduction, the profile is also a function of redshift z and cosmology (Ω_M, h, etc.). The escape velocity radial profile is therefore given by a function of these cosmology and cluster parameters combined,

$$v_{esc}(r, z, \Omega_M, h, \ldots, \beta, \alpha, r_{-2}, \rho_{-2}). \tag{4.3}$$

We note that while we utilize only Einasto density profiles in this chapter, in principle any parametrized mass profile can be used in our framework, as long as the parametrization is a density-potential Poisson pair (see e.g., Miller et al. (2016)).

While the mass dependence and projection effects have long been considered in studies of this observable (see for instance Diaferio & Geller (1997b)), only recently has the cosmological dependence of the escape velocity profile been considered. More specifically, the cosmological dependence of the escape velocity has been studied in relation to both observational data and simulations of standard general relativistic cosmology as well as modified theories of gravity Stark et al. (2016); Miller et al. (2016); Stark et al. (2016). These investigations found the need to include a cosmological term in order to reproduce numerical results as well as observational data.

Qualitatively, it should be unsurprising that the cosmological background within which a cosmic structure is embedded at a given epoch will create the conditions for its evolution and development. For instance, whether a gravitationally bound structure today (say, a galaxy group or galaxy cluster) can become unbound at late times in an accelerating universe is a function of both the curvature of space and the mass-energy content of the background the particular structure is embedded in Busha et al. (2003); Behroozi et al. (2013). It is therefore clear that the theoretical escape velocity profile must take into account the cosmological background.

More specifically, the cosmological dependence in the escape velocity profile in Stark et al. (2016); Miller et al. (2016); Stark et al. (2016) comes in through the "equivalence radius." In an accelerating universe, the radius out to which one has escaped a cluster's potential is a function of cosmology. This minimal radius required to escape, termed the equivalence radius (r_{eq}), decreases in an accelerating universe (see Stark et al. (2016) and references therein). The projected escape velocity profile is then given by,

$$v_{esc}(r,z) = \sqrt{\frac{1}{g(\beta)}\Big[-2\big(\Psi(r)-\Psi(r_{eq})\big) - qH^2\big(r^2 - r_{eq}^2\big)\Big]}. \tag{4.4}$$

We note that, as expected, at $r = r_{eq}$ the escape velocity is nil. The function of the equivalence radius then is to normalize the escape velocity at that point. Note that this equation is derived by integrating the acceleration equation of the effective potential that takes into account both the "negative" acceleration due to the mass of the cluster and the "positive" acceleration of the background at late-times. We therefore obviate the "negative" acceleration due to ram pressure on galaxies given that it is negligible when compared to averaged gravitational effects Faltenbacher et al. (2005). The "equivalent radius," then, is named for the condition that it sets: it is the point at which the negative (inward) acceleration due to the pull of the cluster and the positive (outward) acceleration due to the acceleration of the universe balance each other. For a derivation of Eq. 4.4 see Stark et al. (2016); Miller et al. (2016). We note also that the physical distance r in Eq. 4.4 is cosmology dependent via Eq. 4.2.

Lastly, as detailed in Stark et al. (2016), Eq. 4.4 emerges from the acceleration equation derived by Nandra et al. (2012b) in the context of a flat universe. However, in the cosmological regime we work with, the acceleration equation for a spatially flat and non-flat universe converge. See sections 5.3.1, 5.3.2, and 5.3.3 of Nandra et al. (2012b) and section 2.1 of Stark et al. (2016).

We now consider the two main components of the projected escape velocity profile function (Eq. 4.4): cluster parameters (projection effects and mass profile information) and cosmological parameters.

4.2.1 Cluster parameters

The two components of the cluster parameter set are the mass profile parameters and the anisotropy parameter β encapsulated by the function $g(\beta)$.

The anisotropy parameter β is given by $\beta(r) = 1 - \sigma_t^2/\sigma_r^2$. Where σ_t is a function of the azimuthal and tangential velocity dispersions and σ_r is the radial velocity dispersion. See Section 5.1 of Stark et al. (2016) for details. Note that while the anisotropy profile of the cluster is actually a function of radius ($\beta(r)$), the observed and simulated profile is nearly flat within 0.3 - 1 virial radii Lemze et al. (2013); Serra et al. (2011); Munari et al. (2013). Therefore, in what follows we only consider the escape velocity profile within this radial range so that we can reduce the anisotropy profile to a single value for a given cluster. Once β for a given cluster is inferred we can then use the function $g(\beta)$ to project our escape velocity profile (see Diaferio & Geller (1997b); Stark et al. (2016)). In particular this function is defined geometrically and given by,

$$g(\beta) = \frac{3-2\beta}{1-\beta}. \tag{4.5}$$

As can be implied from this equation, the effect of $g(\beta)$ on the escape velocity profile within the radial range we consider below is to suppress the profile by a constant value when compared to the 3 dimensional case ($g(\beta) = 1$). Quantitatively, the limits of this function are set by the limiting cases of the anisotropy parameter β: radial infall ($\beta = 1$), circular motion ($\beta = -\infty$) and isotropy ($\beta = 0$). For the radial range we are considering, on average, $g(\beta) \sim 3.3$. This entails that, on average, within the radial range considered below, non-projected escape velocity profiles are $\sqrt{g(\beta)} \sim 1.8$ times higher than projected profiles. As a rule of thumb, the more radial the velocity anisotropy of a cluster, the more suppressed the escape velocity profile will be. For a more thorough quantitative analysis of these projection effects see Stark et al. (2016); Serra et al. (2011).

The other component of the cluster parameters that make up our observable is the mass profile of a given cluster. Information about the mass profile of the cluster comes through the gravitational potential $\Psi(r)$. Following Stark et al. (2016); Miller et al. (2016) we pick the Einasto representation of the potential given its capacity to trace the mass distribution of galaxy clusters beyond the virial radius. The gravitational potential $\Psi(r)$, then, is a function of three free parameters: the shape parameter α, the radius where the logarithmic slope of the density profile is equal to -2 (r_{-2}) and the density at r_{-2} (ρ_{-2}). As calculated via the Poisson equation Retana-Montenegro et al. (2012), the potential as inferred from an Einasto density field is,

$$\Psi(r) = -\frac{GM}{r}\left[1 - \frac{\Gamma\big(3/\alpha, s^{\alpha}\big)}{\Gamma(3/\alpha)} + s\frac{\Gamma\big(2/\alpha, s^{\alpha}\big)}{\Gamma(3/\alpha)}\right]. \tag{4.6}$$

$\Gamma(a, x)$ is the upper incomplete gamma function. We are also utilizing the unitless scale radius s given by,

$$s = \frac{r}{r_{-2}}\left(\frac{2}{\alpha}\right)^{1/\alpha}. \tag{4.7}$$

And we re-write the total mass (M) as,

$$M = 4\pi\rho_{-2}r_{-2}^{3}F(\alpha). \tag{4.8}$$

In this last equation we have defined the function of α,

$$F(\alpha) = \Gamma(3/\alpha)\left(\frac{e^2}{8}\alpha^{3-\alpha}\right)^{1/\alpha}. \tag{4.9}$$

Note that in general we follow the definitions and specifications used in Miller et al. (2016); Stark et al. (2016). We treat the mass profiles and β as observable quantities with uncertainties. In simulations, β shows no significant evolution as a function of redshift in the range we are interested in (ie., $0 \leq z \leq 0.8$, see Fig. 2 in Iannuzzi & Dolag (2012)) and is inferred independently of cosmological assumptions Łokas et al. (2006); Benatov et al. (2006); Lemze et al. (2009); Wojtak & Łokas (2010); Biviano et al. (2013). This is not the case for the weak lensing mass profile-inferred parameters (namely α, r_{-2}, and ρ_{-2}). We analyze how systematic errors introduced by uncertainties in cosmological parameters affect weak lensing mass errors in the Section 4.2 below as well as in Appendix D.

4.2.2 Cosmological parameters

Having defined the first set of parameters of the escape velocity profile related to its mass content $(\alpha, r_{-2}, \rho_{-2})$ and projection effects (β), let us now focus on the redshift-evolving and cosmology-dependent terms in Eq. 4.4, namely, the Hubble parameter H, the deceleration parameter q, and the equivalence radius r_{eq}. We describe these terms below.

Given that we work in a regime where the radiation energy density is negligible $(z \leq 0.8)$ the Hubble parameter is given by,

$$H^2 = H_0^2 E^2(z) = H_0^2 \Big[\Omega_M (1+z)^3 + \Omega_k (1+z)^2 + \Omega_{DE} \exp\left\{ 3 \int_0^z d\ln(1+x)[1+w(x)] \right\} \Big], \tag{4.10}$$

where Ω_M and Ω_{DE} are energy densities in matter and dark energy relative to critical, $w(z)$ is the time-varying equation of state of dark energy, and the spatial curvature density parameter is $\Omega_k \equiv 1 - \Omega_M - \Omega_{DE}$. Note that throughout this chapter we work with the scaled Hubble constant h defined via $H_0 = 100h$.

Once we have the Hubble parameter as a function of redshift we can derive the corresponding deceleration parameter, $q \equiv -\ddot{a}a/\dot{a}^2$, where a is the scale factor, as a function of redshift via,

$$q = \frac{(1+z)}{H}\frac{dH}{dz} - 1. \tag{4.11}$$

Lastly, the equivalent radius (r_{eq}) is the physical distance at a given cosmic epoch, for a given cosmology, where the inward pull of gravity balances the outward pull of cosmic acceleration. It is given by Behroozi et al. (2013),

$$r_{eq} = \left(\frac{GM}{-qH^2}\right)^{1/3}. \tag{4.12}$$

This radius is what sets the normalization of the gravitational potential of our galaxy cluster, $\Psi(r_{eq})$ in Eq. 4.4 Miller et al. (2016); Stark et al. (2016). That is, beyond this equivalence radius, the effective potential of the cluster described by Eq. 4.4 ($-2\phi = v_{esc}^2(r,z)$) is normalized to 0 (See Stark et al. (2016) for a derivation). Note also that the distance at which this balance of forces occurs, that is, between cosmic acceleration and the cluster's gravitational pull, is far away enough from the cluster center that the cluster can be represented as a point mass. Lastly, this quantity can be thought of as a proxy for how sensitive $v_{esc}(r,z)$ is to cosmology. In lieu of taking analytic derivatives of Eq. 4.4 one can study the analytic derivatives of r_{eq}. We have confirmed this by looking at numerical derivatives of $v_{esc}(r,z)$ and compared them to the analytic derivatives of r_{eq} for the same cosmology, finding good agreement.

In Fig. 4.1 we show that, for a fixed cluster mass the equivalence radius is sensitive to both cosmology and redshift. More specifically, we pick a mass of $M_{200} = 4 \times 10^{14} M_{\odot}$, where M_{200} is defined as the mass enclosed by a sphere with an average density equivalent to 200 times the mean density of the universe. Note that as the cluster gets closer to the acceleration transition redshift ($q(z) = 0$) the equivalence radius shoots up to infinity. We consider the effects of this behavior on our observable below.

4.2.2.1 $v_{esc}(r,z)$ in an accelerating universe ($q < 0$)

Within the $q < 0$ regime, the escape velocity profile is described by Eq. 4.4. As shown by Stark et al. (2016), in an accelerating universe the effect on the observable generated by changing the various cosmological parameters is to modify both the amplitude and the shape of the escape velocity profile. For instance, in a flat universe, a larger dark energy density makes it easier to escape a galaxy cluster, while a larger dark matter component makes it harder to escape the cluster. This is illustrated in Fig. 4.1. Using the equivalence radius as a proxy to gauge how $v_{esc}(r,z)$ changes,

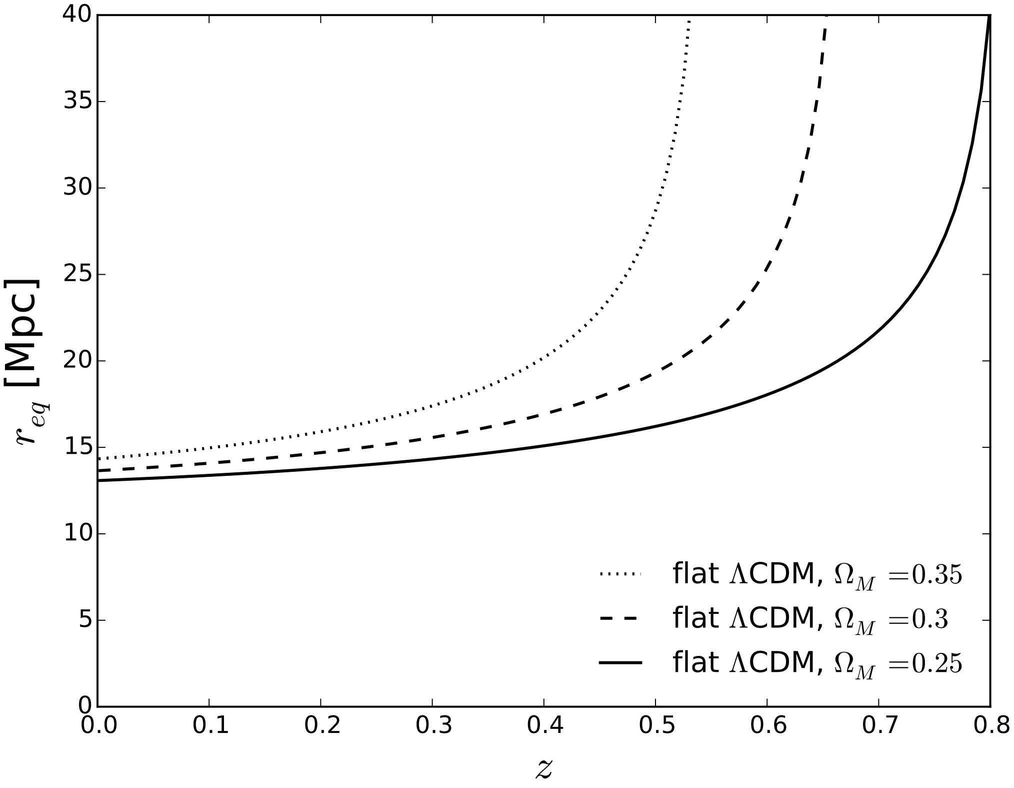

Figure 4.1: Behavior of the equivalent radius (r_{eq}) as a function of redshift (z) for a cluster with mass $M_{200} = 4 \times 10^{14} M_\odot$ for three values of Ω_M in a flat ΛCDM universe and $h = 0.7$. At the transition redshift for each given cosmology, the radius shoots up to infinity. Note how r_{eq} becomes more and more sensitive to Ω_M at higher z.

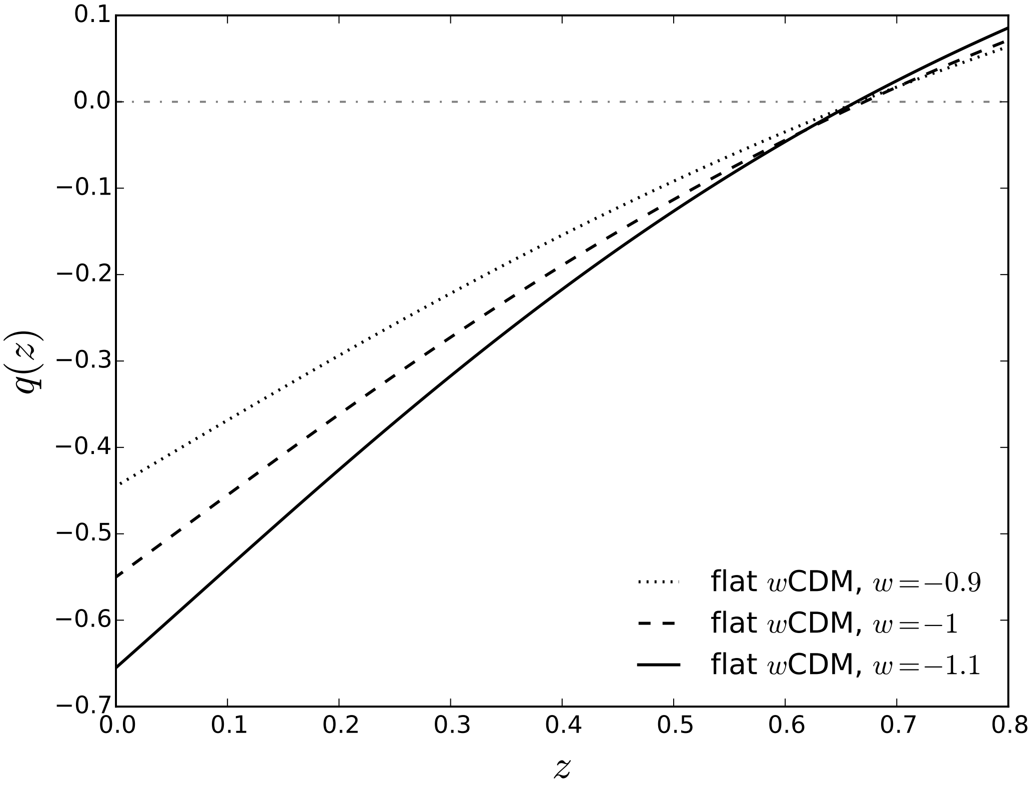

Figure 4.2: Redshift evolution of the deceleration parameter in a flat universe with fixed $\Omega_M = 0.3$ and $h = 0.7$. Notice the divergence of values of q at low redshifts when the equation of state parameter is varied.

we see that the equivalence radius blows up at the given transition redshift for that cosmology (i.e. z that yields $q(z) = 0$).

It is important to emphasize that, in the regime where $q(z) < 0$, $v_{esc}(r, z)$ is a direct measure of both expansion and acceleration, since qH^2 is a function proportional to both $H(z)$ and $dH(z)/dz$. This makes our observable a powerful probe of cosmology. For example, note the sensitivity of the deceleration parameter to the dark energy equation of state w as shown in Fig. 4.2. In particular, the variation of $q(z)$ with respect to w increases at lower redshifts. Fig. 4.3 also demonstrates the sensitivity of the observable to w by showing the fractional difference between the escape velocity for a flat ΛCDM universe at $z = 0$ and two dark energy models, quintessence-like dark energy (solid line) Tsujikawa (2013) and phantom dark energy (dotted line) Caldwell (2002). Note the ∼10% level differences between these models and Λ (dashed line). A quintessence-like dark energy, then, would increase the escape velocity profile, whereas a phantom dark energy would decrease the escape velocity (both relative to ΛCDM).

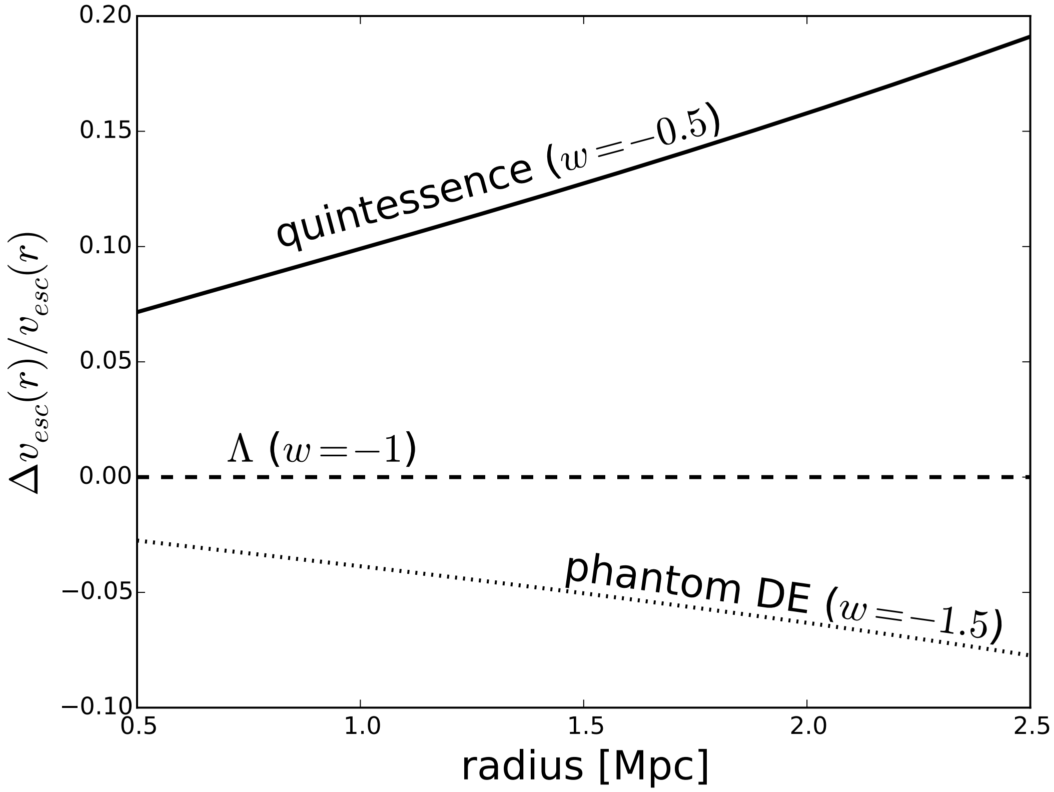

Figure 4.3: Using a single cluster with mass $M_{200} = 4 \times 10^{14} M_\odot$ at $z = 0$, we show the fractional difference between the escape velocity profile of a flat wCDM universe with dark energy equation of state $w = -1$ and two other dark energy models (quintessence in the solid line and phantom dark energy in the dotted line). More specifically, $\Delta v_{esc}(r,z)/v_{esc}(r,z) = [v_{esc}(w)/v_{esc}(w = -1)] - 1$. Quintessence therefore acts similarly to increasing the dark matter density. That is, it increases the escape velocity profile relative to the Λ case (see Fig. 1 of Stark et al. (2016)). On the other hand, the phantom dark energy suppresses the escape velocity profile relative to the Λ case. Lastly, we highlight that the fractional difference increases with radius in both cases.

4.2.2.2 $v_{esc}(r, z)$ at the transition redshift ($q = 0$)

As implied in the previous subsection, as we approach $q = 0$ the equivalence radius blows up and Eq. 4.4 is reduced to the gravitational potential described by the Einasto gravitational potential $\Psi(r)$. More explicitly,

$$\lim_{q \to 0} v_{esc}(r, z) = \sqrt{\frac{1}{g(\beta)} \bigg[-2\Psi(r) \bigg]}. \tag{4.13}$$

One immediate consequence we derive from this behavior is that the only cosmological dependence we get beyond this point is through r (see Eq. 4.2).

We now investigate what happens to our observable beyond the transition redshift or, equivalently, what happens to our observable with combinations of cosmological parameters that yield a decelerating universe (i.e. $q > 0$).

4.2.2.3 $v_{esc}(r, z)$ beyond the transition redshift ($q > 0$)

In the regime beyond the transition redshift, or when $q > 0$, it makes no sense to speak of an equivalence radius. Recall that the equivalence radius is defined in the context of a balance of forces. Given that there is no balance of forces between the mass-induced pull of gravity and the repulsive acceleration as there is in the case where $q < 0$, there is no such equivalence radius.

We note that within the virial radius, the theoretical expectation embodied in Eq. 4.4 works to high precision up to $z \sim z_t + \delta z$, where z_t is the transition redshift and δz is small. See, for example, Fig. 4 in Miller et al. (2016). Beyond the transition redshift, however, the analytic theory of Eq. 4.4 is complicated both by cluster assembly dynamics and the theoretical ambiguity of what occurs to the escape velocity profile in a universe that is approaching the Einstein-de Sitter case. When $q > 0$, the internal dynamics of a bound system like a galaxy cluster are solely governed by the Poisson equation with gravity acting to source to accelerate the member galaxies.

Given this, in the Fisher matrix analysis that follows, we pick $z = 0.8$ as the maximum redshift out to which we can realistically push our probe. Later on in the chapter we discuss the implications of defining a redshift range for the probe.

Having described both the cluster and cosmological parameter dependence of our probe, and having considered the regimes of applicability of our probe, we now quantitatively characterize, through the Fisher matrix formalism, how well our observable may be able to constrain cosmological parameters.

4.3 Fisher matrix

The Fisher matrix formalism has been vital in predicting how well a given cosmological probe can constrain any given set of cosmological parameters Tegmark et al. (1997); Heavens (2016); Coe (2009); Huterer & Turner (2001); Albrecht et al. (2006).

In this section we briefly go over the Fisher matrix formalism. We construct the Fisher matrix for our observable quantity, include parameters describing systematic errors in these observations, discuss how we apply priors on cluster and cosmological parameters, and calculate the marginalized errors on cosmological parameters.

4.3.1 Formalism

In general, the Fisher information matrix is a function of the derivatives of the log likelihood of our observable with respect to the observable's parameters (p),

$$F_{ij} = \left\langle -\frac{\partial^2 \ln \mathcal{L}}{\partial p_i \partial p_j} \right\rangle. \tag{4.14}$$

Given that the observable quantity is the escape velocity as a function of redshift and radius we have that the Fisher matrix elements are sums over clusters (index n) and radii (indices k and l),

$$F_{ij} = \sum_{nkl} \frac{\partial v_{esc}(z_n, r_k)}{\partial p_i} (C^{-1})_{kl} \frac{\partial v_{esc}(z_n, r_l)}{\partial p_j}, \tag{4.15}$$

where C is the covariance of escape velocity measurements at different radii. Here we assume that the escape velocity measurements in different clusters are uncorrelated, and that the measurement covariance for different radii in a cluster (matrix C) is independent of redshift.

After adding priors to our cluster parameters the Fisher information matrix is then given by,

$$F = F_{ij} + F_{prior}. \tag{4.16}$$

From this F we can then compute the marginalized lower bound of the uncertainty on any of our N parameters via the Cramér-Rao inequality, $\sigma_{p_i} \geq \sqrt{(F^{-1})_{ii}}$. The inverse is calculated via Gaussian elimination. We ensure that the inversion of the matrices we work with are stable by calculating the condition number for each F matrix and ensuring that it is less than $\sim 10^{12}$.

As detailed in the previous section, the parameters in our observable can be split up into two sets: cluster and cosmological parameters. Consequently, the parameters that we will be taking the derivatives with respect to (p) can be represented by the union of the following two sets:

$$p \in p_{clus} \cup p_{cosmo}. \tag{4.17}$$

The parameters describing the clusters 1 to N (i.e. three parameters for the mass profile plus one more describing the anisotropy parameter, per cluster) can then be encapsulated in the following set,

$$p_{clus} \in \{\beta_1, \alpha_1, r_{-2,1}, \rho_{-2,1}, \ldots, \beta_N, \alpha_N, r_{-2,N}, \rho_{-2,N}\}. \tag{4.18}$$

The cosmological parameter set p_{cosmo} is composed of the cosmological parameters. We detail the cosmological models we study, and the corresponding sets of p_{cosmo}, in the next section.

Considering these sets, we therefore have a N_{dim} by N_{dim} dimensional Fisher matrix F given by:

$$N_{dim} = 4 \times N_{clus} + N_{cosmo}, \tag{4.19}$$

where N_{clus} is the number of clusters and N_{cosmo} is the number of cosmological parameters. We provide a sketch of the Fisher matrix structure and explore its structure more thoroughly in Appendix C.

4.3.2 F_{ij} matrix

In this subsection we focus our attention on the components that make up the F_{ij} matrix (Eq. 4.15).

4.3.2.1 Fiducial cluster

As with any Fisher matrix analysis, the derivatives of Eq. 4.15 are calculated at a given set of fiducial values. For our fiducial cosmology we pick $p_{cosmo,fid} \in \{\Omega_M = 0.3, \Omega_\Lambda = 0.7, w_0 = -1, w_a = 0, h = 0.7\}$. For our fiducial cluster parameters we pick $p_{clus,fid} \in \{\alpha = 0.1984, \rho_{-2} = 1.0521 \times 10^{14} [M_\odot/\mathrm{Mpc}^3], r_{-2} = 0.497[\mathrm{Mpc}], \beta = 0.145\}$. The β fiducial value is around what has been estimated for galaxy clusters (see Łokas et al. (2006); Benatov et al. (2006); Lemze et al. (2009); Wojtak & Łokas (2010); Biviano et al. (2013)) and the three Einasto fiducial cluster parameters are equivalent to a cluster of mass $M_{200} = 4 \times 10^{14}$. More specifically, we use the mass-concentration relation in Sereno (2015) to map our fiducial mass M_{200} to the Einasto parameters

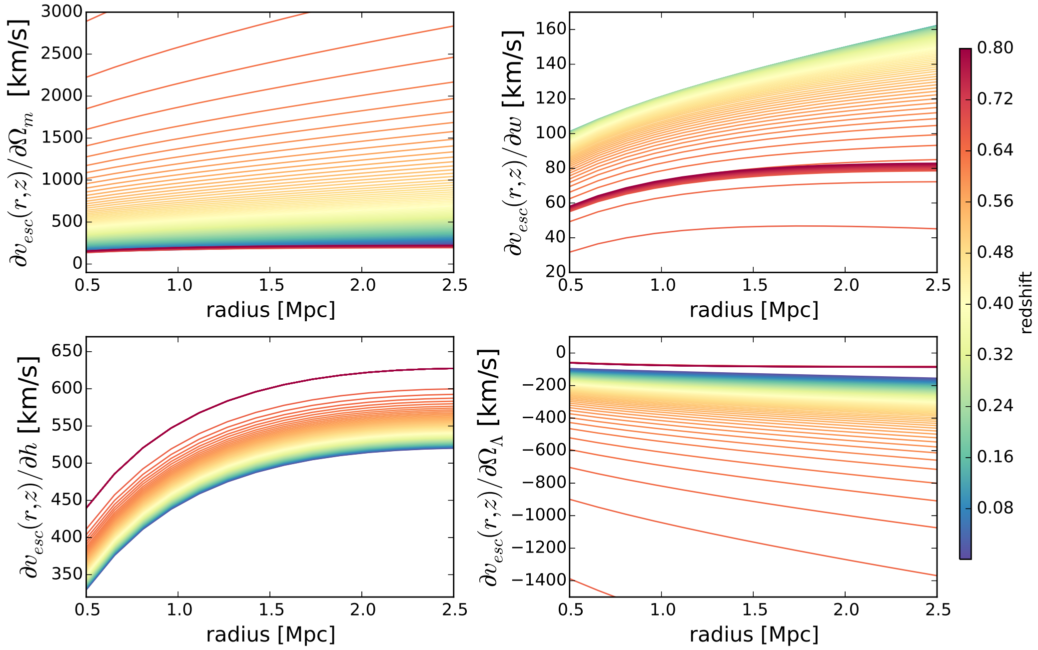

Figure 4.4: Sensitivity of the observable $v_{esc}(r, z)$ to cosmology. The partial derivatives of the escape velocity profile are calculated numerically at 100 different redshifts (z) with respect to the various cosmological parameters for our fiducial cluster. The specific redshift of a given profile can be identified through the color bar on the right-hand side of the figure. In all cases, the information grows (i.e. the observable becomes more sensitive) the farther out we go radially. Some parameters are most sensitive at higher redshifts (Ω_M, Ω_Λ and h) while others are more sensitive at lower redshifts (w). Note that beyond the transition redshift for our fiducial cosmology, the derivatives with respect to all parameters reach a limit, as implied by Section 4.2 .

at $z = 0$ by fitting the Navarro-Frenk-White (NFW) density profile to the Einasto density profile. For analytical representations of these density profiles see Sereno et al. (2016b) and references therein.

Furthermore, to calculate the derivatives of Eq. 4.15 we place our fiducial cluster along different redshifts z_n and recalculate its angular size θ with fixed r at that given redshift via Eq. 4.2. We discuss this radial range in the next sub-subsection.

In Fig. 4.4 we plot some of the derivatives for our fiducial cluster used in our Fisher matrix analysis. More specifically, we plot the radial derivatives of $v_{esc}(r, z)$ with respect to various cosmological parameters for 100 clusters of the same fiducial mass uniformly distributed in the range $0 \leq z \leq 0.8$. Fig. 4.4 is a useful way to study the sensitivity of our observable to various cosmological parameters. In particular Fig. 4.4 tells us that our observable is more sensitive to certain cosmological parameters at higher redshifts, such as Ω_M, (the red lines, which represent high redshift clusters are higher than the blue ones, which represent low redshift clusters), and more sensitive to other parameters at lower redshift, such as the dark energy equation of state parameter w. Judging from the derivatives in Fig. 4.4, our probe is most sensitive to the parameter Ω_M. Note also that for all parameters, the sensitivity increases with radius. We emphasize that beyond the transition-to-acceleration redshift ($z_t = 0.671$) in the standard ΛCDM model we no longer gain much cosmological information as encapsulated by Eq. 4.13. Beyond this redshift we still get information cosmological information via r which is a function of the angular diameter distance (Eq. 4.2).

4.3.2.2 Radial bins and covariance matrix C^{-1}

Having described the derivatives of Eq. 4.15 we now describe the covariance matrix C in that same equation. Simply put, this matrix embodies the covariance of between different measurements of our observable at a given radial bin in a cluster n.

For a perfect three-dimensional observation of the galaxy velocities, there would be no projection effects and therefore one would expect a nonzero covariance between v_{esc} at different radii. This effect is random between different radial bins, and it effectively decouples the measurements in different radial bins, reducing the bins' covariance. More specifically, this scatter arises from the fact that when observing a galaxy cluster, random galaxies along the line of sight may be included in the phase space. This drastically reduces the covariance between radial bins. Therefore, it is a good assumption that the radial covariance matrix is diagonal. That is, C^{-1} is reduced to $\sigma_{v_{esc}}^{-2}$.

Mathematically, at any given radius, the uncertainty in $v_{esc}(r, z)$ is given by the combination of the spectroscopic uncertainty, uncertainty due to the edge measurement, and any additional intrinsic uncertainties,

$$\sigma_{v_{esc}} = \sqrt{\sigma^2_{spec} + \sigma^2_{edge} + \sigma^2_{edge,int}}. \tag{4.20}$$

We choose $\sigma_{spec} = 50$ kms^{-1} to match the redshift accuracy of modern spectroscopic surveys (Bolton et al., 2012). To calculate the uncertainty on the statistically inferred edge at a given radial bin we follow Gifford et al. (2013) who used simulations to show that when viewing along a line-of-sight the edge can be recovered to high statistical precision ($\sim 5\%$ or less) when 100 or more galaxies are used in the phase spaces (see their Figure 4 – bottom right). For our fiducial cluster this corresponds to 50 kms^{-1} since the observed edge is typically around 1000 kms^{-1}. We also allow for an intrinsic scatter between the observed edge and how accurately it can recover the true underlying gravitational potential. Gifford & Miller (2013a) used simulations to quantify the statistical accuracy and precision of the cluster mass using the projected edge when the density, potential, and anisotropy are known exactly. They find that there is a statistical floor of 25% error in mass, which translates into a 12.5% error in the edge since mass scales as the square of the potential. For our fiducial cluster, this intrinsic error corresponds to ~ 125 kms^{-1}.

As in Eq. 4.20, we sum these three components in quadrature giving $\sigma_{v_{esc}} = 143.61$ kms^{-1} for our fiducial cluster. This is about a 15% total error in the measurement of the projected phase space escape velocity edge. Lastly, note that if we double the total error budget on v_{esc}, our constraints on the cosmological parameters increase by about 80%.

We next tackle the question of how many radial bins we should use for a given cluster in our Fisher matrix calculations.

Our one requirement here is to be able to resolve the shape of the velocity edge vs. radius, $v_{esc}(r)$. In all cases, we assume densely sampled phase spaces (i.e., 100-200 galaxies within the virial radius). Since more massive clusters are also larger in size, we can maximize the number of useful radial bins by choosing the most massive clusters for our analysis.

At the moment, we can typically rely on reasonably accurate weak lensing mass estimates for the highest mass systems in the universe. Therefore, for this chapter we will assume an SPT (South Pole Telescope)-like sample with $M_{200} > 3 \times 10^{14} M_\odot$ High et al. (2010). More specifically, as mentioned elsewhere in the chapter, we pick a fiducial mass of $M_{200} = 4 \times 10^{14} M_\odot$.

Furthermore, as detailed in Section 4.2, we can only work within the radial range of about 0.3 - 1 virial radii if we assume that the anisotropy profile can be reduced to a single parameter. Henceforth for our profiles and constraints we pick a radial range between $0.5 \leq r \leq 2.5$ Mpc, the outer range corresponding to about r_{200} (where the density reaches 200 × the mean value) and the inner range corresponding to about $0.3 \times r_{200}$ described above (High et al., 2010). This radial range, given $\Delta r \sim 0.1$ Mpc yields $N_{bins} = 14$ radial bins. This is what we use in our calculations throughout our chapter (see Eq. 4.21 below).

Note that if we change the number of radial bins from 14 to 7 and 21, the constraints on the cosmological parameters change by $\sim$ 20%. We can therefore in principle get better constraints than what is presented in the next section by increasing the number of radial bins. However, binning too finely is not desirable given that it can introduce additional statistical noise in the observable and may not even be possible, given the density of galaxies in the phase spaces that are observationally viable.

Given all of this, Eq. 4.15 thereby becomes,

$$F_{ij} = \sum_{n=1}^{N_{clus}} \sum_{k=1}^{N_{bins}} \frac{1}{\sigma^2_{v_{esc}}} \frac{\partial v_{esc}(r_k, z_n)}{\partial p_i} \frac{\partial v_{esc}(r_k, z_n)}{\partial p_j}. \tag{4.21}$$

and is therefore a sum over N_{clus} clusters and N_{bins} radial bins. This is the F_{ij} matrix we utilize for all of our constraints presented in section IV, in conjunction with the prior matrix which is discussed in the following subsection.

4.3.3 F_{prior} matrix

The Fisher information matrix formalism allows us to add additional independently measured information attained on certain model parameters (both cluster and cosmological) to our Fisher matrix. This is implemented via the prior information matrix F_{prior} in Eq. 4.16. The structure of this matrix is given by,

$$F_{prior} = \begin{pmatrix} C^{-1}_{cosmo} & & 0 & \\ & C^{-1}_{cluster} & & \\ & & C^{-1}_{cluster} & \\ 0 & & & \ddots \end{pmatrix}. \tag{4.22}$$

We discuss the elements of this prior information matrix below.

Cluster Parameter Uncertainties

WL mass error	σ_α	$\sigma_{\rho_{-2}}[M_\odot/\mathbf{Mpc}^3]$	$\sigma_{r_{-2}}[\mathbf{Mpc}]$	σ_β	$\sigma_{v_{esc}}$ [$\mathbf{kms}^{-1}$]
5% stat + 5% cosmo sys ("stacked")	0.0024	5.887×10^{12}	0.0314	0.02	90.14
20% stat + 20% cosmo sys ("40% mass scatter")	0.0096	23.589×10^{12}	0.1342	0.5	143.61
40% stat + 40% cosmo sys ("80% mass scatter")	0.0181	43.904×10^{12}	0.2913	0.5	143.61
40% stat ("Riess et al 2016 prior on h")	0.0096	23.589×10^{12}	0.1342	0.5	143.61

Table 4.1: Cluster parameter uncertainties that make up the F_{prior} matrix used in the various cases considered in the Constraint Forecasts section as well as the error on the edge $\sigma_{v_{esc}}$ that makes up the F_{ij} matrix. Note that in principle there is no covariance between β and the three other parameters, but we simply change the uncertainty on β for the other cases with reduced weak lensing mass scatter. Furthermore, as explained in the text, we use the weak lensing (WL) mass percent error on M_{200} as shorthand to describe uncertainties in all three Einasto parameters. In the last row we tabulate the uncertainties in the three Einasto parameters after applying a prior on h from from Riess et al. (2016). All other cluster parameter uncertainties listed contain both statistical error as inferred from weak lensing (WL) analyses and systematic error from cosmology as explained in the "Prior information" section and Appendix D.

4.3.3.1 Cluster prior information ($C^{-1}_{cluster}$)

In our case, the mass parameters (which come from weak lensing mass estimates) and the anisotropy parameter (which comes from analysis of the phase spaces of the clusters via the Jeans equations) are known to within some precision from these independent measurements. We therefore add a prior information matrix to account for this external information on the non-cosmological parameters.

More specifically, the error bars on the weak lensing mass estimates are chosen to be similar to what is reported in the literature based on recent observations. As a representative sample, see the metacatalog compiled in Sereno (2015). We particularly choose an M_{200} error range from 20% to 40% which is based on ground-based imaging. For instance, Applegate et al. (2014b) reports typical statistical errors of $\sim 20\%$ using Surprime-Cam imaging for 50 clusters to a redshift of 0.7. Similarly, Umetsu et al. (2014) primarily used Subaru/Suprime-Cam to obtain weak lensing errors at a level of $20 - 30\%$ based on the CLASH sample. Melchior et al. (2016) also reports ~40% statistical errors for four clusters using science verification data from the Dark Energy Survey on the CTIO 4m Blanco DECam imager. This is why, as our baseline, we use the upper range of 40% statistical error on the mass. In what follows we also consider 5% statistical error as a floor that can be potentially achieved through the technique of stacking galaxy clusters Becker & Kravtsov (2011b); Rozo et al. (2011).

However, there are also systematic errors that need to be considered. These can come from a variety of observational sources including the telescope point-spread function, the background redshift distribution, the intrinsic shape variations of the background galaxies, and more. Applegate et al. (2014b) reports systematic errors that are small compared to the statistical errors (7%) when the telescope optical system is well characterized.

Few researchers have allowed for cosmology to vary during the weak lensing mass estimation process. As we approach higher precision requirements, we will need to incorporate variations in cosmology when calculating the cluster masses and it could play an important role in the overall error budget. Therefore, we estimate how large the mass errors would grow when allowing cosmology to vary during the mass estimation process. We do this while keeping the nominal statistical error, which represents the current conservative end of ground-based results. As explained in the Appendix D, we find that the total (statistical + cosmological systematic) error, for example, increases from 20% to 40%. That is, considering cosmological systematics in the weak lensing analysis increases the mass error by a factor of 2. Also as detailed in the Appendix, the cosmological systematics can be undercut by applying a prior on the Hubble parameter h. We tabulate these results in Table 4.1.

Note that when in this chapter we speak of some percentage of "mass scatter" we refer to both the statistical and cosmological systematic error as tabulated in the first three rows of Table 4.1. The last row of Table 4.1 shows the uncertainties for a case in which the Hubble prior has been implemented. In that case, the 80% uncertainty on the mass is reduced to 40% after applying the prior on h from Riess et al. (2016) ($\sigma_h = 0.0174$). See Appendix D for details.

Note also that when we speak of mass scatter we refer to how the statistical uncertainties in all three cluster parameters change (α, ρ_{-2} and r_{-2}). More specifically, we use the more widely reported percent scatter on M_{200} as a shorthand to describe the uncertainties in our Einasto cluster parameters. As with the fiducial mass, we attain these uncertainties by propagating the 1σ errors on the NFW density profile to the Einasto density profile parameters by fitting the profiles out to one virial radii.

Also unless otherwise stated, and as shown in Table 4.1, for the anisotropy parameter we use an uncertainty of $\sigma_\beta = 0.5$ which is also a fairly conservative choice. For example, see uncertainties on β as derived from a Jeans' analysis in Łokas et al. (2006).

These parameter uncertainty priors come into our prior matrix only along the diagonal. This is because we are already considering covariances on the prior information between cluster and cosmological parameters through the aforementioned analysis. Note that this does not mean that we are not considering covariances between parameters. We are, these are all encapsulated in the Fisher matrix F_{ij}. We simply neglect covariance on most prior information. In this sense, our attempt to grapple with the covariances in our prior matrix (detailed in Appendix D) is only an approximation. Note, however, that some parameter uncertainties in the prior matrix are actually nil. For instance, a Jeans equation analysis inference of β is what allows us to decouple the edge uncertainty $\sigma_{v_{esc}}$, as well as other cluster parameters from σ_β. In contrast, inferring β from edge measurements as done by Stark et al. (2016) would introduce a complete covariance between edge measurements and the anisotropy parameter. The Jeans equation evades this problem given that it is a function of the derivative of the potential rather than the potential itself.

Lastly, the inverse cluster covariance matrices ($C^{-1}_{cluster}$) contain the aforementioned priors on the mass parameters as well as the prior on the cluster anisotropy parameter. We add covariance between relevant parameters of the cluster prior submatrix. In particular, we model the covariance between cluster parameters r_{-2} and ρ_{-2}. We discuss the structure of the submatrices $C^{-1}_{cluster}$ in Appendix C.

4.3.3.2 Cosmological prior information (C^{-1}_{cosmo})

In relation to the cosmological prior information matrices, we note that for most cases we are not adding any cosmological priors so that in Eq. 4.22, C^{-1}_{cosmo} is an N_{cosmo} by N_{cosmo} null matrix. Where noted, we add a diagonal prior on the C^{-1}_{cosmo} matrix from the 2.4% determination of the Hubble constant from Riess et al. (2016).

4.4 Constraint Forecasts

We now derive marginalized uncertainties on cosmological parameter p_{cosmo}, marginalized over the cluster nuisance parameters $p_{cluster}$. Note that in some cases we also marginalize over remaining cosmological parameters to generate 2-dimensional likelihoods.

We consider three cosmological models. The first two assume a flat universe ($\Omega_k = 0$) and the last case assumes a non-flat universe ($\Omega_k \neq 0$).

4.4.1 Constant equation of state w

For this case, we consider the following set of cosmological parameters,

$$p_{cosmo} \in \{\Omega_M, w, h\}. \tag{4.23}$$

Via Eq. 4.10 we find the Hubble parameter which yields

$$H^2 = H_0^2 E(z)^2 = H_0^2 \left[\Omega_M (1+z)^3 + \Omega_{DE}(1+z)^{3(1+w)} \right]. \tag{4.24}$$

And the deceleration parameter via Eq. 4.11,

$$q = \frac{1}{2} \left[\Omega_M(z) + (1+3w)\Omega_{DE}(z) \right]. \tag{4.25}$$

Here, $\Omega_M(z) = \Omega_M(1+z)^3 E(z)^{-2}$ and $\Omega_{DE}(z) = \Omega_{DE}(1+z)^{3(1+w)} E(z)^{-2}$. The combination then of the deceleration parameter and Hubble parameter that makes up the equivalent radius and our observable is given by,

$$qH^2 = \frac{H_0^2}{2} \left[\Omega_M(1+z)^3 + (1+3w)(1-\Omega_M)(1+z)^{3(1+w)} \right]. \tag{4.26}$$

Notice that the quantity $E(z)$ cancels out in this expression.

The constraints in the $\Omega_M - w$ plane, after marginalizing over h and all other cluster parameters are shown in Fig. 4.5. In particular, in black/grey (dark/light red) we plot the 68% and 95% confidence level constraints for a set of $N_{clus} = 1000(100)$ clusters uniformly distributed in the range $0 \leq z \leq 0.8$. The marginalized 1σ errors are $\sigma_{\Omega_M} = 0.007(0.025)$ and $\sigma_w = 0.138(0.431)$ for $N_{clus} = 1000$ (100). This is an extraordinarily tight constraint considering that it is achieved by the escape velocity method alone, before adding constraints from other probes.

4.4.2 w_0 and w_a

In the previous case we considered a constant dark energy of equation of state (EoS). However, in principle the dark energy EoS can evolve with redshift. A popular way to parametrize the redshift evolving dark energy EoS through the so-called Chevallier-Polarski-Linder (CPL) parametrization given by, (see Chevallier & Polarski (2001); Linder (2003))

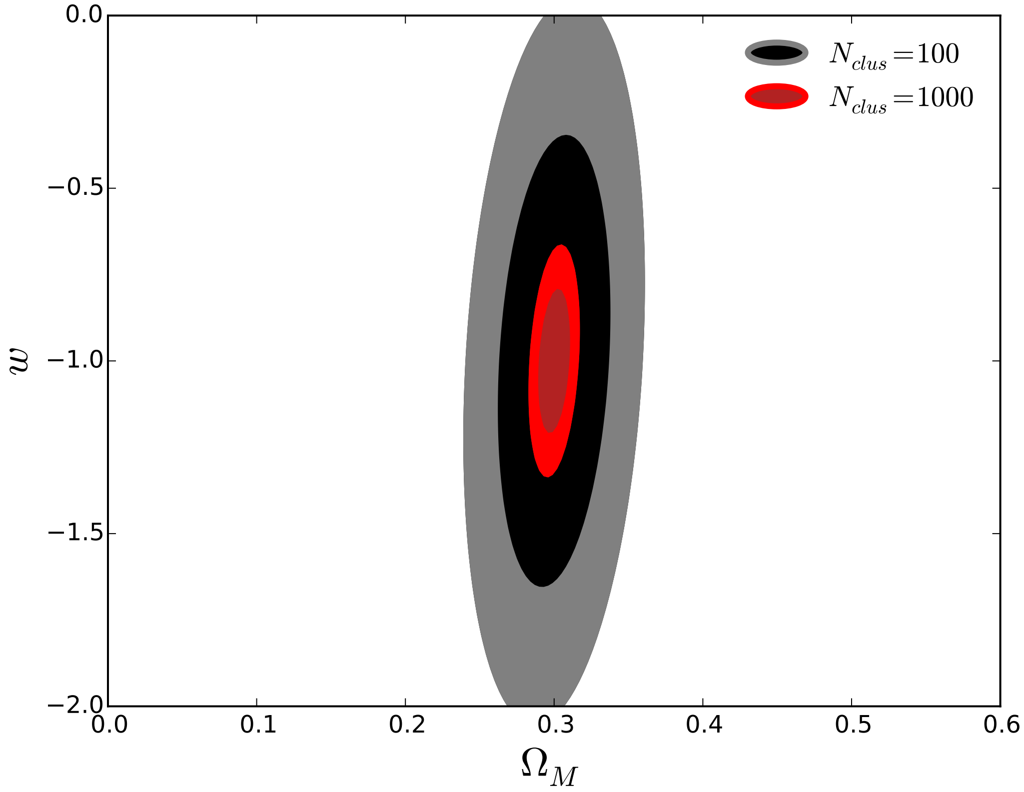

Figure 4.5: 68% and 95% confidence constraints for the flat wCDM case after marginalizing over all other parameters. We use $N_{clus} = 1000$ (100) clusters as shown in red (black) uniformly distributed in the range $0 \leq z \leq 0.8$. The priors on the Einasto parameters assume a uniform 80% weak lensing mass scatter for all redshifts (see Table 4.1). The 1σ errors are $\sigma_{\Omega_M} = 0.007(0.025)$ and $\sigma_w = 0.138(0.431)$ for $N_{clus} = 1000$ (100).

$$w(z) = w_0 + w_a \frac{z}{1+z}. \tag{4.27}$$

In this case we consider the following set of cosmological parameters,

$$p_{cosmo} \in \{\Omega_M, w_0, w_a, h\}. \tag{4.28}$$

Again we derive the Hubble parameter for this case,

$$H^2 = H_0^2 E(z)^2 = H_0^2 \left[\Omega_M (1+z)^3 + \Omega_{DE} (1+z)^{3(1+w_0+w_a)} e^{-3w_a \frac{z}{1+z}} \right]. \tag{4.29}$$

and the deceleration parameter

$$q = \frac{1}{2} \left[\Omega_M(z) + \Omega_{DE}(z) \left(1 + 3w_0 + \frac{3w_a z}{1+z} \right) \right]. \tag{4.30}$$

The redshift evolving mass and dark energy densities are given by, $\Omega_M(z) = \Omega_M(1+z)^3 E(z)^{-2}$ and $\Omega_{DE}(z) = \Omega_{DE}(1+z)^{3(1+w_0+w_a)} e^{-\frac{3w_a z}{1+z}} E(z)^{-2}$.

Again the redshift evolving energy density term $E(z)$ cancels and we are left with,

$$qH^2 = \frac{H_0^2}{2} \left[\Omega_M (1+z)^3 + (1-\Omega_M)(1+z)^{3(1+w_0+w_a)} \right.$$
$$\left. \times \exp\left\{ -\frac{3w_a z}{1+z} \right\} \left(1 + 3w_0 + \frac{3w_a z}{1+z} \right) \right]. \tag{4.31}$$

We show the resulting 2-dimensional $w_0 - w_a$ likelihood in Fig. 4.6 for a uniform set of clusters in the range $0 \leq z \leq 0.8$, after marginalizing over Ω_M, h, and all other cluster parameters. With $N_{clus} = 1000$ clusters uniformly distributed between $0 \leq z_c \leq 0.8$ with 80% (40%) weak lensing mass scatter the turquoise (purple) contours express the following marginalized uncertainties: $\sigma_{w_0} = 0.139(0.124)$ and $\sigma_{w_a} = 0.968(0.857)$.

We then reduce the number of clusters to $N_{clus} = 100$ and apply a cosmological prior on the Hubble constant from Riess et al. (2016) ($\sigma_h = 0.0174$) to yield the following marginalized 1σ errors, $\sigma_{w_0} = 0.191$ and $\sigma_{w_a} = 2.712$ (see pink contours in Fig. 4.6). Note that the pink contour is made using the same redshift range ($0 \leq z \leq 0.8$) and systematic error (40% weak lensing mass scatter and $\sigma_\beta = 0.5$) as before but with only 100 clusters. Note that this constraint on w_0 is comparable to

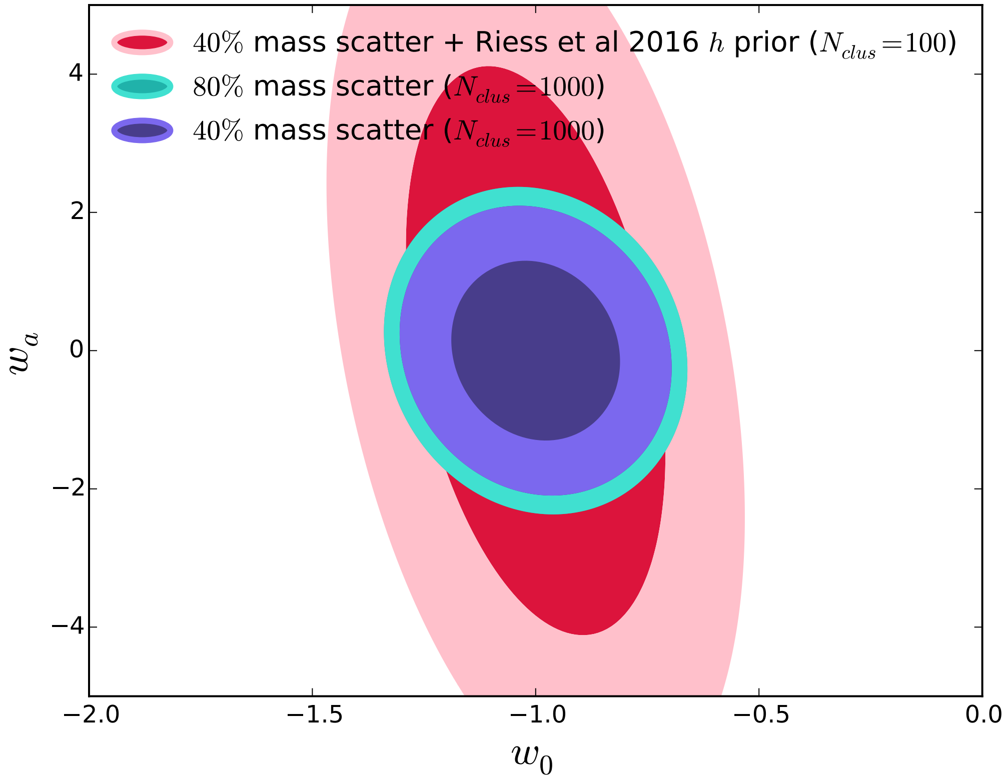

Figure 4.6: 68% and 95% contours for the dynamic dark energy case using the CPL parametrization of dark energy marginalized over Ω_M and h as well as the other cluster parameters. More specifically, we use $N_{clus} = 1000$ clusters uniformly distributed between $0 \leq z_c \leq 0.8$ with 80% (40%) weak lensing mass scatter in the turquoise (purple) contour which yields: $\sigma_{w_0} = 0.139(0.124)$ and $\sigma_{w_a} = 0.968(0.857)$. With $N_{clus} = 100$ uniformly distributed in the same redshift range as before and with 40% mass scatter but now adding a prior on the Hubble constant from Riess et al. (2016) we attain, $\sigma_{w_0} = 0.191$ and $\sigma_{w_a} = 2.712$ (pink contours).

the constraint achieved with 1000 clusters of Fig. 4.5 (red contours).

4.4.3 non-flat universe, Ω_M and Ω_Λ

So far we have only considered flat universes in our analysis. We now drop this assumption and assume the possibility of nonzero curvature, while fixing the dark energy equation of state to $w = -1$. We then have the following set of parameters to constrain,

$$p_{cosmo} \in \{\Omega_M, \Omega_\Lambda, h\} \tag{4.32}$$

For this case the Hubble parameter is given by

$$H^2 = H_0^2 E(z)^2 = H_0^2 \Bigg[\Omega_M (1+z)^3 + \Omega_\Lambda + \Omega_k (1+z)^2 \Bigg]. \tag{4.33}$$

And the deceleration parameter,

$$q = \frac{1}{2}\Omega_M(z) - \Omega_\Lambda(z). \tag{4.34}$$

Multiplying these two we have,

$$qH^2 = \Bigg[\frac{1}{2}\Omega_M (1+z)^3 - \Omega_\Lambda \Bigg] H_0^2. \tag{4.35}$$

The constraints in the $\Omega_M - \Omega_\Lambda$ plane, after marginalizing over all cluster parameters are shown in Fig. 4.7. With just $N_{clus} = 100$ uniformly distributed between $0 \leq z \leq 0.8$ we can achieve the following marginalized uncertainties $\sigma_{\Omega_M} = 0.101(0.185)$ and $\sigma_{\Omega_\Lambda} = 0.197(0.428)$ after applying the 2.4% level prior on H_0 from Riess et al. (2016) (compare green to black contours).

4.5 Observational strategies

In order for the escape velocity measurements to yield competitive cosmological constraints in both the near term and the far future, several considerations must be taken into account. In this section we particularly focus on how future surveys should target specific redshifts in order to optimize cosmological constraints. We also explore the extent to which reducing systematic uncertainties in both weak lensing mass estimates and measurements of the anisotropy parameter will yield significantly

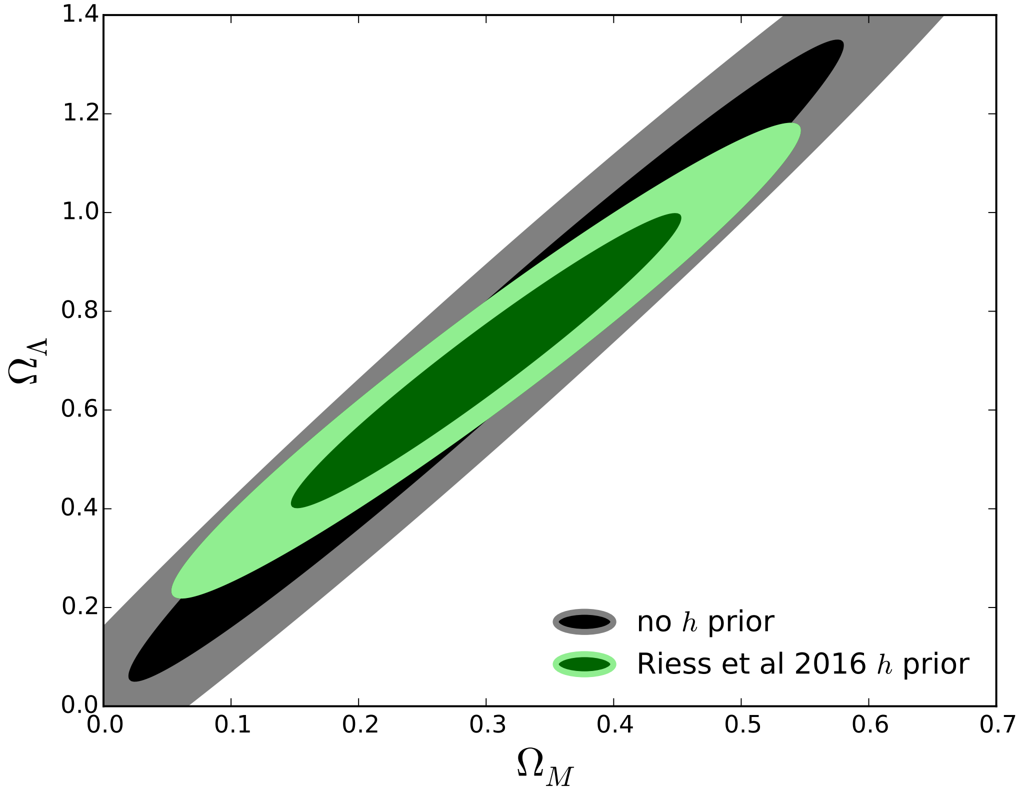

Figure 4.7: 68% and 95% contours for the non-flat ΛCDM case for $N_{clus} = 100$ uniformly distributed between $0 \leq z \leq 0.8$ with 80% mass error. Applying a prior on the Hubble constant h from Riess et al. (2016) ($\sigma_h = 0.0174$) allows us to break the degeneracy and thereby significantly improve our constraints. The marginalized 1σ constraints derived from the green (black) contours are $\sigma_{\Omega_M} = 0.101(0.185)$and $\sigma_{\Omega_\Lambda} = 0.197(0.428)$.

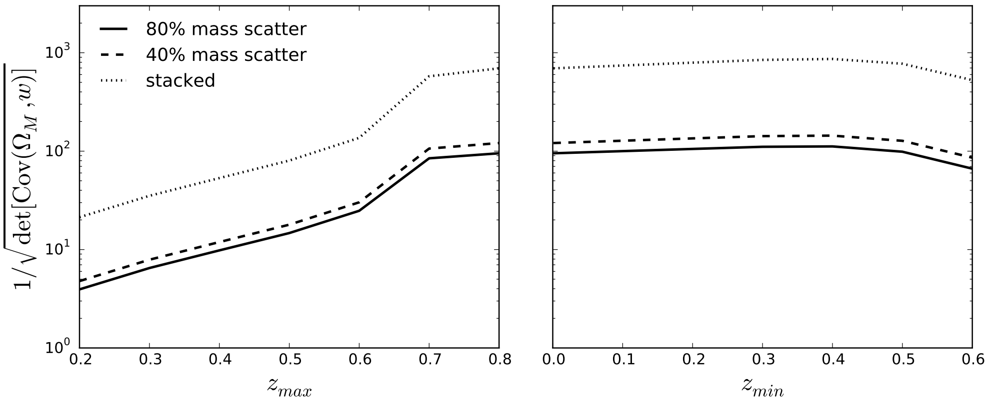

Figure 4.8: Inverse area of the Ω_M - w covariance matrix after marginalizing over all other parameters as a function of maximum (left panel) and minimum (right panel) redshift used. We assume a uniform redshift distribution of clusters in the range $0 \leq z \leq z_{max}$ (left panel) and $z_{min} \leq z \leq 0.8$ (right panel). Each calculation of the inverse area assumes a fixed number of clusters, $N_{clus} = 100$. Note that $\Omega_M - w$ constraints can be improved by reducing the mass uncertainty from 80% (solid line) to 40% (dashed line), in which case the contour area decreases by a factor of ∼1.3. The constraint can be further increased by utilizing stacked weak lensing mass estimates and stacked phase spaces, and this yields a 10% mass scatter and $\sigma_\beta = 0.02$ (see Table 4.1), decreasing the contour area by a factor of ~ 7.5 (compare solid to dotted lines). The left panel also illustrates that using clusters beyond the transition redshift leads to a gradual loss of cosmological information. While a tighter constraint can be achieved by incorporating higher redshift clusters, the right panel demonstrates that we still need low redshift clusters to achieve the tightest constraints on w. See Fig. 4.9. We conclude that as broad as possible redshift range of clusters be used (e.g. $0 \leq z \lesssim 0.8$).

better cosmological constraints when compared to simply increasing N_{clus}.

4.5.1 Redshift range

We want to investigate how the cosmological constraints vary with a change of the limits on this redshift distribution. In particular, note that the contours shown in Figures 4.5-4.7 utilize a uniform redshift distribution in the range $0 \leq z \leq 0.8$ for the cluster sample. How would these contours change if we changed the cluster redshift range used?

To quantify the effect, we calculate how the area of the 1σ contours in any given 2-dimensional cosmological parameter space changes as a function of the redshift distribution chosen. Mathematically, this entails taking the covariance matrix that contains the marginalized parameters we are interested in and calculate how its de-

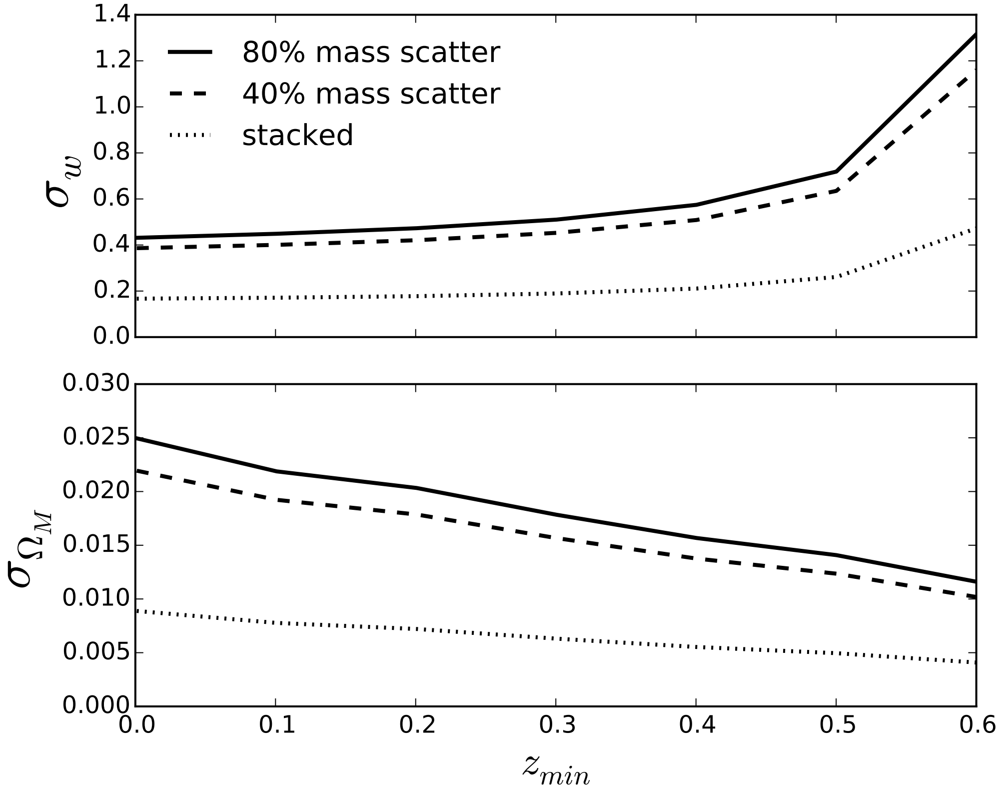

Figure 4.9: Marginalized Ω_M and w uncertainties for the flat wCDM case with 100 clusters distributed in the range $z_{min} \leq z \leq 0.8$. Note that as the minimum redshift z_{min} increases a factor of ∼1.7 improvement in σ_{Ω_M} is attained (see solid line, bottom panel). The trade-off is a significant loss of information on the dark energy equation of state parameter w at high redshift (top panel). These effects combine to make the inverse area plot as a function z_{min} relatively flat (see right-hand side panel in Fig. 4.8). Note also that a maximum factor of ~ 4 improvement in the uncertainty of these parameters may be achieved if cluster parameter uncertainties are reduced (compare solid to dotted lines).

terminant changes as a function of the maximum and minimum redshifts for a given distribution. More explicitly, the inverse area corresponding to the 2 by 2 covariance matrix for the marginalized parameters within the 1σ bound is given by (see Huterer & Turner (2001); Albrecht et al. (2006)),

$$\mathrm{A}^{-1}(p_i, p_j) = \frac{1}{\sqrt{|\det[\mathrm{Cov}(p_i, p_j)]|}}. \tag{4.36}$$

For the $w_0 - w_a$ case the inverse area is the Dark Energy Task Force "Figure of Merit" (FoM) Albrecht et al. (2006).

The result for the flat wCDM case as a function of redshift range used is shown in Fig. 4.8. It shows the inverse area for a fixed number of clusters (100 in this case) uniformly distributed in the range $0 \leq z \leq z_{max}$ (left panel) and $z_{min} \leq z \leq 0.8$ (right panel).

As the left panel of Fig. 4.8 implies, we can get the tightest constraints on this cosmological parameter subset by picking 100 clusters uniformly distributed in the range $0 \leq z \leq 0.8$. The physical reason for this can already be inferred from Fig. 4.4 which shows the derivatives of our observable with respect to the various cosmological parameters. In that figure we note that while our observable is sensitive to Ω_M at high redshifts, it is simultaneously more sensitive to w at low redshifts. Moreover, our probe is relatively more sensitive to Ω_M than to w (compare the absolute maximum of the derivatives). This immediately implies that the higher redshift clusters will end up contributing more to the joint constraint.

However, we want to emphasize that this does not mean that we should therefore only pick high redshift clusters. In Fig. 4.9 we plot the marginalized uncertainty for both w (top panel) and Ω_M (bottom panel) as a function of z_{min}. As we pick higher redshift clusters the constraint on Ω_M improves but the constraint on w is degraded. This is also shown by the relatively flat but ultimately decreasing tendency of the right panel in Fig. 4.8. As such, we emphasize that we need both high and low redshift clusters if we are going to attain a tight constraint on both Ω_M and w. This applies to other constraints as well.

Secondly, note that this particular optimized choice (ie. picking clusters uniformly distributed in the range $0 \leq z \lesssim 0.8$) arises from our fiducial cosmology which yields $z_t = 0.671$. Riess et al. (2007) for instance, finds a transition redshift of $z_t = 0.43 \pm 0.07$ based on a linear parametrization of $q(z)$. Therefore, the inferences of the transition redshift are highly model dependent Shapiro & Turner (2006). What this means is that, observationally, since the optimization of our probe is loosely based on the transition redshift, we recommend that a redshift distribution as broad as possible be used. In particular, we recommend that clusters uniformly distributed in the range $0 \leq z \leq 0.8$ be used. Picking this redshift range allows us to safely take into account current uncertainties in the transition redshift.

Lastly, note also that this upper limit ($z = 0.8$) is also set by the particular processes of cluster assembly. In other words, beyond this redshift our analytic model is unable to take into account the full complexity of cluster-formation dynamics because clusters are still assembling at that redshift for acceptable cosmologies (see Fig. 2 in Holz & Perlmutter (2012)).

4.5.2 Reducing Systematics and Stacked Clusters

We now study the effects of reducing statistical errors on the cluster parameters. Clearly, reducing statistical errors in the weak lensing mass estimates, in the inference of anisotropy parameter, and in the measurement of the edge, will improve our cosmological constraints, but by how much? For this exercise, we consider increased precision from better measurements on individual clusters, increased cluster sample sizes, and through stacking techniques. We note that stacking is not necessarily equivalent to averaging over a large sample. For additional information on stacking, we refer the reader to detailed analyses of stacking weak lensing data and stacking phase-spaces (Rozo et al., 2011; Gifford et al., 2017). To quantify the improvements, we use Eq. 4.36 with a fiducial sample of $N_{clus} = 100$ and focus on the $\Omega_M - w$ case.

Fig. 4.8 shows how constraints may be improved by decreasing the scatter on the mass parameters from 80% (solid black line) to 40% (dashed black line). The difference in the inverse area size is a relatively modest factor of ~ 1.3. However, simultaneously reducing the uncertainty of the mass parameters to 10% as well as reducing the uncertainty of the anisotropy parameter σ_β and the uncertainty on the escape velocity edge σ_{vesc} yields an area that is ~ 7.5 times smaller (compare solid lines to dotted lines). For the exact values of the uncertainties used in our matrix for this "stacked" case see Table 4.1. Fig. 4.9 follows and demonstrates how each specific marginalized error (on w and Ω_M) varies with z_{min} as we change the error on the cluster priors. Looking at Fig. 4.9, an improvement of a factor of ∼2-4 on both σ_M and σ_w may be achieved with decreased uncertainties (compare solid to dotted lines).

Currently, the only way to attain uncertainties in the mass parameters of the smallest order in Figures 4.8 and 4.9 requires a stacking analysis. For example, see cosmological constraints derived from a weak lensing analysis in Rozo et al. (2011) as well as stacked phase-space analyses in Gifford et al. (2017). Similarly, achieving

$\sigma_\beta = 0.02$ will entail stacking clusters and/or developing some other approach that has not yet been fully investigated. Thus, the dotted line in Fig. 4.8 represents not 100 clusters, but 100 cluster ensembles with high-precision mean masses and mean β's. Each "cluster ensemble" is built from a number of individual noisy weak lensing cluster profiles and poorly sampled cluster phase spaces. One thing to consider in a future stacked phase spaces analysis is that systematic uncertainties (e.g,. cluster mis-centering) must be accounted for at high precision.

From an observational perspective, it is an interesting question whether one should expend resources on increasing the sample size, or on decreasing the systematic uncertainties. Given a Planck cosmology, to $z = 0.8$ we expect to have over 40,000 clusters with $M_{200} > 4 \times 10^{14} M_\odot$ with respect to 200× the mean density of the Universe (Planck Collaboration et al., 2016b). Thus, it seems reasonable to expect that 1000 of these clusters will eventually have both weak-lensing mass estimates and well-sampled radius/velocity phase spaces. Such an effort would require photometry and spectroscopy over about 1000 square degrees of the sky. As an example, the Dark Energy Spectroscopic Instrument–DESI [1]) is targeting over 1000 square degrees of the Dark Energy Survey sky coverage (DESI Collaboration et al., 2016). Likewise, the Prime Focus Camera will provide significant multi-object spectroscopy over more than 1000 square degrees of imaging taken with the Subaru Hyper Suprime-Cam (Takada et al., 2014). There is also new PI-based instrumentation, such as the Michigan-Magellan Fiber System (M2FS) on the Magellan observatory, which can be used to specifically and efficiently target clusters with previously measured weak lensing masses (Mateo et al., 2012). Thus, it is realistic to expect 1000 clusters with densely sampled phase spaces and redshift errors ~ 50 kms^{-1} and weak lensing mass errors of 40% or less (statistical) in the near future. The technology to collect the needed spectra either exists or is being constructed with the aim to achieve redshift errors on par with existing surveys (Bolton et al., 2012) and the weak lensing mass errors of 40% or less are already being achieved with current imagers (Melchior et al., 2016; Applegate et al., 2014b). Therefore, in Figs. 4.5, 4.10 and 4.11 we show the constraints after increasing the fiducial sample size from 100 to 1000 clusters.

Lastly, it should be obvious that a combination of both more clusters and reduced systematic error would be the optimal solution which yields the tightest constraints. Our analysis in this section is premised on the assumption that both of these options may not be easily available.

---

[1] http://desi.lbl.gov/

4.6 Comparison to other probes and joint constraints

Other than by reducing statistical errors, increasing the number of clusters, and stacking, we may in principle improve the constraints through a joint likelihood analysis with other cosmological probes. In this section we discuss our constraints and their degeneracies in the context of other probes.

We note that in Fig. 4.7 an improvement in the forecasted constraints can be achieved after applying the prior on h from. Riess et al. (2016). Information on the Hubble parameter breaks numerous degeneracies in our probe. After all, our technique itself is fundamentally based on constraining qH^2 (see Sec. 4.4.1). However, by including cosmological dependencies on the radial coordinate (Eq. 4.2) the probe clearly has some power in constraining h on its own. This is evident in the derivatives shown in Fig. 4.4. If we drop this dependence and use a fixed (in Mpc) radial coordinate, Ω_Λ, w_0, and w_a all become entirely unconstrained.

Besides applying a prior on the Hubble constant, another way we may achieve a tight constraint of the $w_0 - w_a$ plane is shown in Fig. 4.10. We show both the 68% and 95% confidence constraints with $N_{clus} = 1000$ uniformly distributed in the redshift range $0 \leq z \leq 0.8$, after applying a conservative 80% mass scatter prior (in red, same as turquoise contours in Fig. 4.6) as well as both the JLA SNIa constraints of Betoule et al. (2014) (in blue) and the 2015 Planck TT likelihood constraints of Planck Collaboration et al. (2016a) (in green). A joint analysis with these probes then seems to have the potential of yielding similar constraints to what a combination of JLA data and CMB currently yields.

Now considering the flat wCDM case, in Fig. 4.11 we over-plot the JLA constraints (in blue), the 2015 Planck TT likelihood of Planck Collaboration et al. (2016a) (in green) as well as re-plot the red contours of Fig. 4.5. We find that a joint constraint of these probes alone can yield a joint $\sigma_w \sim 0.1$ and $\sigma_{\Omega_M} \sim 0.01$ constraint given that they cross through each other nearly perpendicularly.

We note that the degeneracies in our observable work out in such a way that our probe can act as a powerful cross check of systematics in other probes. As an example, note how our constraints lie perpendicular to the JLA SNIa and CMB constraints in Fig. 4.11. In part, this is due to the way degeneracies work with our observable.

As shown in Section 4.2, cosmology in our probe comes in through the quantity qH^2 which is both a function of the Hubble parameter and its derivative, $dH(z)/dz$. We emphasize this because our probe in this sense is a true dynamical probe of the expansion history of the universe, similar to the redshift drift. Compare for instance,

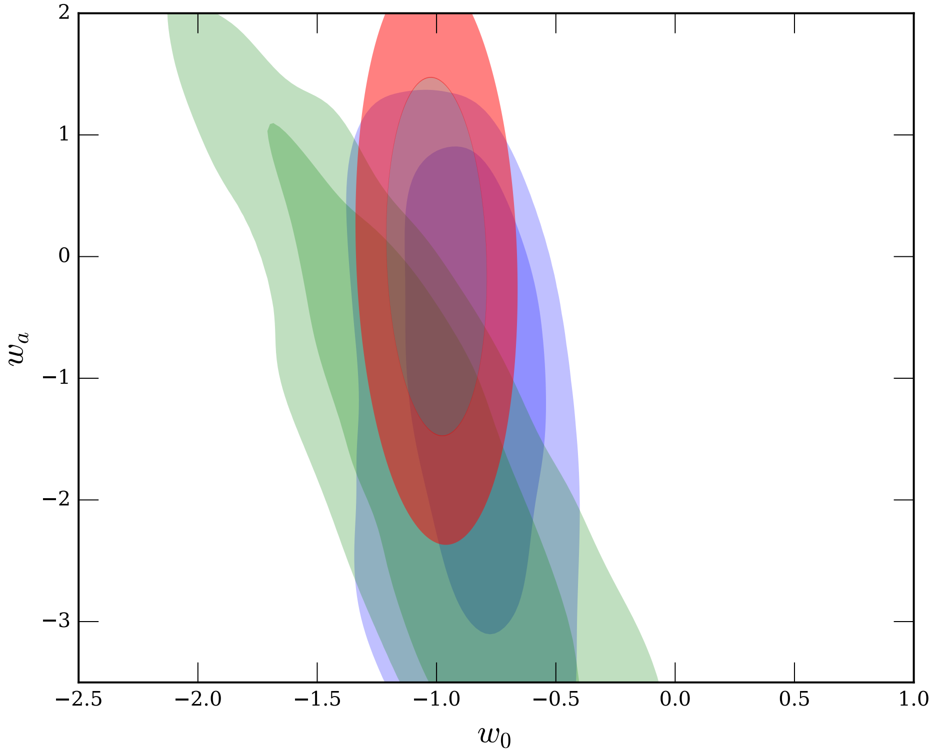

Figure 4.10: 68% and 95% contours for the dynamic dark energy case using the CPL parametrization of dark energy marginalized over Ω_M and h as well as the other cluster parameters. The blue contours are reproduced from the latest JLA SNIa constraints of Betoule et al. (2014). The green contours are reproduced from the Planck 2015 TT likelihood of Planck Collaboration et al. (2016a). In red are constraints derived from a sample of $N_{clus} = 1000$ clusters uniformly distributed in the redshift range $0 \leq z \leq 0.8$, after applying a conservative 80% mass scatter prior (same as the turquoise contours of Fig. 4.6). In all cases, no prior assumptions about the Hubble constant are used.

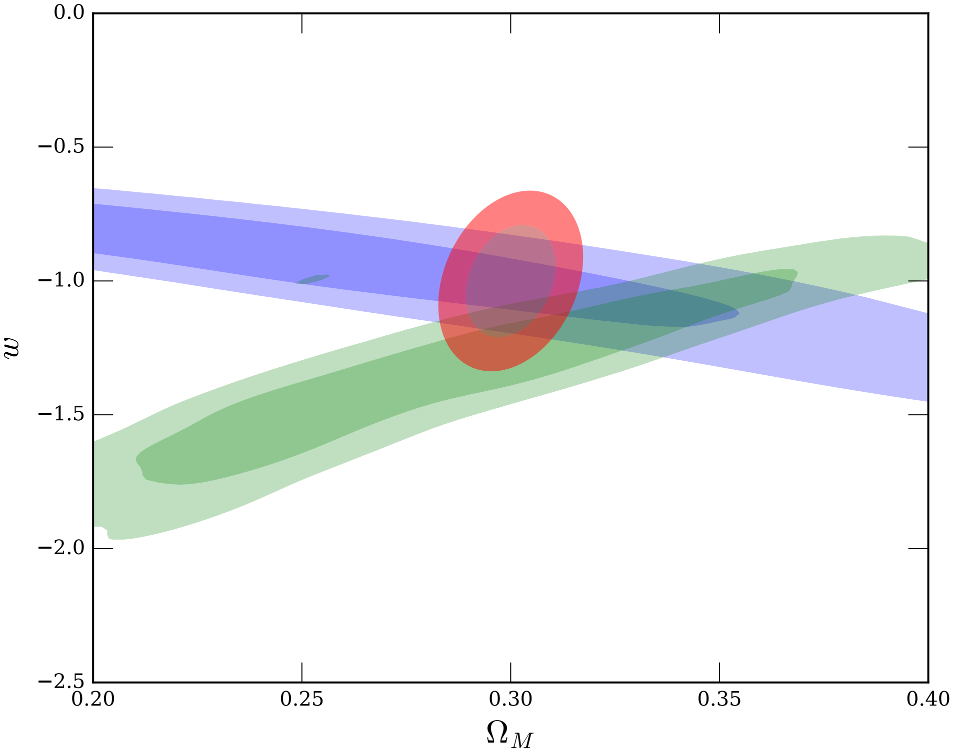

Figure 4.11: 68% and 95% contours for the flat wCDM case. The red contours are derived the same as what is shown in Fig. 4.5. The blue contours are reproduced from the latest JLA SNIa constraints shown in Betoule et al. (2014). The green contours are reproduced from the Planck 2015 TT likelihood Planck Collaboration et al. (2016a). In all cases, no prior assumptions about the Hubble constant are used.

our constraint degeneracies on the $w_0 - w_a$ plane to those of Kim et al. (2015) (in particular, see Fig. 3).

Beyond these comparisons to other probes, we may ask ourselves if we can justify our observable's sensitivity to cosmology on its own basis. As discussed before, the sensitivity of our probe can be directly inferred from both Fig. 4.4 and Fig. 4.3. Recall that on Fig. 4.3 we plot the fractional difference of the escape velocity profile between the ΛCDM model ($w = -1$) and two other dark energy models. At about the virial radius, the fractional difference amounts to $\sim 15\%$. So to a crude first approximation, we need the error budget in the observational parameters to drop below this limit in order to place constraints on w.

As explained before, and as tabulated in Table 4.1, three sources of observational error are involved: the escape velocity edge error ($\sigma_{v_{esc}}$), the anisotropy parameter uncertainty (σ_β) and the error in the inferred Einasto parameters from weak lensing (α, $\sigma_{\rho_{-2}}$,$\sigma_{r_{-2}}$). If we focus just on the $\sigma_{v_{esc}}$ we notice that this amounts to a $\sim 15\%$ error on the escape velocity edge. As such, with just one cluster we are on the verge of being able to detect deviations from the ΛCDM model. Similarly, for our fiducial cluster, the uncertainty in $\sigma_\beta = 0.5$ amounts to a difference in the escape velocity profile also of $\sim 15\%$ given that it comes in to our observable through the factor of $1/\sqrt{g(\beta)}$ (see Eq. 4.4). So again, with this systematic uncertainty we are close to being able to detect deviations from $w = -1$. Now let us consider the dominant source of error which comes in through the uncertainty in the inferred Einasto parameters from weak lensing. For 80% error on the mass, this amounts to an error on the edge of $\sim 40\%$ given that the velocity goes as the square root of the mass. With just 8 clusters we can naively decrease the weak lensing error to ($\sim 15\%$), assuming that it scales as $1/\sqrt{N_{clus}}$. Of course the above are unrealistic conditions, which is why instead we conduct a detailed Fisher Matrix analysis.

Another key factor in this probe is that unlike supernovae observations, the cluster data map a projected radial profile which increases the total amount of information per object, thereby further beating down the error. We previously addressed how the binning can affect the final predictions on the cosmological parameters. The key point is that with just a few tens of clusters, this probe becomes sensitive to 15% deviations in the dark energy equation of state exemplified in Fig. 4.3. While these are only forecasts, as a consistency check, we have compared our Fisher matrix constraints with the analysis of Stark et al. (2016) which utilized $N_{clus} = 20$ ($0 \leq z \leq 0.439$). We find that our Fisher matrix forecasts are consistent with variations of systematics studied in Stark et al. (2016).

4.7 Summary

We have presented a novel galaxy cluster-based probe of cosmology that has the potential of constraining cosmological parameters to high precision. More specifically, this cosmological probe is based on both the abstract and concrete need to include a cosmological term in the escape velocity profile of galaxy clusters as inferred from their phase spaces. This phase space-inferred escape velocity profile is modeled by cluster-specific parameters (i.e. weak lensing mass profile information and the cluster's anisotropy parameter) as well as cosmological parameters. If the first set of parameters can be independently inferred, then cosmology can be allowed to vary to fit the observed escape velocity profiles — thereby constraining cosmological models.

To assess this probe's observational viability we used the Fisher matrix formalism and carefully considered the aforementioned systematics by marginalizing over the free parameters describing the gravitational potential of each cluster separately. While constraints can be improved if systematic errors in both the weak lensing mass estimates and inferences of the anisotropy parameter are reduced, we note that the the gains are similarly improved by increasing the number of clusters N_{clus}. A combination of both of these approaches would of course be optimal. However, we note that even assuming conservative errors, competitive cosmological constraints can still be achieved in the near term.

Nonetheless, we have shown that this probe is not only able to yield high precision constraints on cosmological parameters independently of other probes but that it complements other constraints as well. Furthermore, we emphasize that these constraints can be achieved in both the near and far future. For instance, Fig. 4.6 and Fig. 4.7 only use 100 clusters with 40-80% weak lensing mass scatter which can easily be achieved in the near term; this is also the case with the black contours constraints of Fig. 4.5. Far future constraints ($N_{clus} = 1000$) are forecasted in Fig. 4.5 (red contours) as well as in the future joint constraints of Figs. 4.10-4.11.

We also note that while throughout this chapter we have assumed the general relativistic Friedmann equation, our theoretical expectations can in principle be generalized by re-working the term qH^2 to either reflect modified theories of gravity or other alternative parametrizations.

This work therefore presents a first step in the study of a promising new probe of cosmology. The cluster phase spaces, we demonstrated here, have the power to provide precision measurements of cosmological parameters in an accelerating universe, and thus provide sharp tests of the currently favored theoretical framework.

CHAPTER V

Cluster escape velocity profiles as a probe of Chameleon gravity

5.1 Introduction

In this last chapter we no longer assume that our theory of gravity is exclusively that of general relativity (GR). In particular, we present a novel test of gravity on galaxy cluster scales that strategically harnesses how the Chameleon $f(R)$ gravity screening mechanism modifies the gravitational potential of clusters of different masses. Specifically, this modified gravity (MG) model deepens the potential in the outskirts of low mass galaxy clusters with respect to GR, but leaves the potential of high mass clusters relatively unaffected. By taking the average ratio between the gravitational potential of high mass and low mass galaxy clusters, we show that one can unambiguously discern between Chameleon-like modified gravity theories and GR.

We note that our proposed test is complementary to probes of gravity on larger scales (1-10 Mpc) (Lam et al., 2012; Hellwing et al., 2014; Zu et al., 2014; Xu, 2015) and can also act as a powerful cross-check of tests in galaxy cluster scales (0.1-$1h^{-1}$Mpc) (Schmidt et al., 2009; Wojtak et al., 2011; Terukina et al., 2014; Wilcox et al., 2015; Cataneo et al., 2015; Lombriser et al., 2012b; Llinares & Mota, 2013; Schmidt, 2010). However, our test distinguishes itself in that it directly probes the gravitational potential and allows for a simple and elegant incorporation of theoretical predictions.

We carry out our proposed test of gravity using synthetic dark matter halos of cosmological N-body simulations and test its viability by comparing results with analytic theory. We then utilize simulated galaxy catalogs to incorporate realistic observational systematics, including projection effects. After vetting our analytical expectations with simulations, we show that our probe has the potential to deliver more competitive cluster-scale constraints on Chameleon *f(R)* MGs than at present.

The chapter is organized as follows: in Sec. 5.2 we review the Hu-Sawicki $f(R)$ gravity model and derive the theoretical expectations of our observable in both MG and GR. In Sec. 5.3 we describe how we obtain our observable from the phase space of galaxy clusters, and detail how we do this in N-body simulations. A brief description of the N-body simulations we used is also provided. Sec. 5.4 is devoted to putting together both our theoretical expectations and observables. More specifically, we describe how our test probes gravity in the scale of galaxy clusters. In Sec. 5.5 we address both theoretical and observational systematics, whether or not they are significant as well as how we fold them into our final analysis. Finally, in Sec. 5.6 we discuss both how our probe can set competitive constraints on MG and, more generally, can also act as a powerful test of ground-based in the scale of galaxy clusters. We conclude in Sec. 5.7 with some remarks on how our probe will leverage the observational capacities of future large-scale photometric and spectroscopic surveys.

5.2 Theoretical expectations

5.2.1 Hu-Sawicki $f(R)$ gravity

In what follows we focus on a particular model of MG: Chameleon Hu-Sawicki *f(R)* gravity (Hu & Sawicki, 2007). In *f(R)* gravity, the Einstein-Hilbert action is augmented by a free function of the Ricci scalar (*R+f(R)*). This modification introduces an additional degree of freedom which can be recast as a non-minimally coupled scalar field, $f_R \equiv \frac{df(R)}{dR}$, dubbed the *scalaron.* The functional form of $f(R)$ in the Hu-Sawicki model is as follows:

$$f(R) = -\bar{m}^2 \frac{c_1(R/\bar{m}^2)^n}{c_2(R/\bar{m}^2)^n + 1}. \tag{5.1}$$

The $\bar{m}$ parameter sets the mass scale and is given by $\bar{m}^2 = \frac{8\pi G}{3}\rho_{m0}$, where ρ_{m0} is the average density today. As such, this model is determined by three dimensionless free parameters: c_1, c_2 and n. The specific values of these free parameters can be narrowed down to those which produce expansion histories that are consistent with current cosmological constraints. In particular, these three parameters are related to the background value of the scalaron today, f_{R0}. For example, with $\Omega_M = 0.24$ and $\Omega_\Lambda = 0.76$, we have that $f_{R0} \approx nc_1/c_2^2/(41)^{n+1}$ (Hu & Sawicki, 2007). From now on, we parametrize these free parameters in terms of f_{R0} and consider models that are phenomenologically viable. We refer the reader to Hu and Sawicki (2007) for the particularities of the model and the details of the calculations shown above. We fix $n = 1$ and consider only models with background field values in the present epoch of $|\overline{f_{R0}}| = 10^{-5}$ and 10^{-6}, which will be denoted from now on as FR5 and FR6 respectively. Note that in our definition of $|\overline{f_{R0}}|$ we have set the the speed of light to unity.

5.2.2 Gravitational potential

Naturally, as a coupled scalar field, the effect of the scalaron is to mediate an additional fifth force between massive bodies. Thus, the gravitational potential which massive particles experience is no longer the usual Newtonian dynamical potential of the Poisson equation (ϕ_{GR}), but rather (Lombriser et al., 2012a):

$$\phi(r) = \phi_{GR}(r) - \frac{1}{2}\delta f_R(r). \tag{5.2}$$

Here the δ signifies that the background has been subtracted from the scalaron field: $\delta f_R = f_R - \overline{f_R}$.

The additional scalar field can be shielded in Chameleon Hu-Sawicki $f(R)$ gravity in order to recover the predictions made by GR in high density regions. In the high density "Chameleon regime," the screening mechanism ensures we recover GR by making $f_R \to 0$. As such, in this regime the scalaron's field value is:

$$\delta f_R^{cham} = -\overline{f_{R0}}. \tag{5.3}$$

The scalar field is constant in high density regions (e.g. in the core of galaxy clusters) and can mediate no additional forces. Outside of the high density core, the field can propagate and mediate a fifth force. The range of this fifth force is determined by Compton wavelength of the field, or the inverse mass of the scalar field $\lambda_c \equiv m^{-1}$, which at the background and for $z = 0$ is: $m^{-1} = 32\sqrt{\overline{f_{R0}}/10^{-4}}$ Mpc h^{-1} (Schmidt et al., 2009). In this "linear regime," the scalaron field is given by (Lombriser et al., 2012a):

$$\begin{aligned}\delta f_R^{lin}(r) = -\frac{1}{3}g(c)GM_{200}\big\{&\Gamma(0, m(r + r_s))e^{2m(r+r_s)} \\ &+ \Gamma(0, -m(r + r_s)) - \Gamma(0, -mr_s) \\ &- e^{2mr_s}\Gamma(0, mr_s)\big\}\frac{e^{-m(r+cr_s)}}{r}.\end{aligned} \tag{5.4}$$

The upper incomplete gamma function $\Gamma(s,r)$ and $g(c)$ are given by $\Gamma(s,r) = \int_r^\infty t^{s-1}e^{-t}dt$ and $g(c) = [\ln(1+c) + c/(1+c)]^{-1}$. We have also used the definition: $r_s \equiv R_{200}/c$. Eq. 5.3 is specific to the case in which the scalaron is propagating in an Navarro-Frenk-White (NFW) density field of a galaxy cluster with concentration c, mass M_{200}, and radius R_{200}. The subscript 200 implies that the mass and radii are defined to be where the density of the halo equals $\Delta_{200} = 200$ times the critical density of the day: $M_{200} = \frac{4\pi}{3}R_{200}^3\Delta_{200}\rho_{crit}$. In practice, the concentration is an NFW fitting parameter attained by fitting the cumulative mass profile (Łokas & Mamon, 2001; Navarro et al., 1997):

$$M(<r) = g(c)M_{200}\left[\ln\left(1+\frac{r}{r_s}\right) - \frac{r}{r+r_s}\right]. \tag{5.5}$$

The transition from the Chameleon (Eq. 5.3) and Linear regimes (Eq. 5.4) is efficient, so we model it as being instantaneous and match them using,

$$\delta f_R = \min(\delta f_R^{lin}, \delta f_R^{cham}). \tag{5.6}$$

As shown by Lombriser et al. (2012a), this approach agrees with the numerical solution to the scalaron equation of motion in the vicinity of an NFW density field. Note that the theoretical uncertainty is negligible when compared to observational uncertainties (thoroughly explained in the Sec. 4.5 below).

The GR potential (ϕ_{GR}) is the usual gravitational potential that satisfies the Poisson equation and therefore determines the motion of massive particles. ϕ_{GR} can be attained by solving the Poisson equation with the NFW mass profile of Eq. 5.4,

$$\phi_{GR}(r) = -g(c)\ln\left(\frac{r}{r_s}+1\right)\frac{GM_{200}}{r}. \tag{5.7}$$

5.2.3 Escaping a galaxy cluster in an accelerating universe

However, our observable, as explained in the next section, is the escape velocity profile ($v_{esc}(r)$) which is related to the potential set by both the gravity of the cluster and the expanding universe ($\Phi(r)$). This effective potential relates to the escape velocity profile as usual: $-2\Phi(r) = v_{esc}^2(r)$. Following Behroozi et al. (2013), we derive $v_{esc}(r)$ for a cluster described by an NFW density in an expanding universe with GR as its prescription for gravity,

$$\begin{aligned} -2\Phi_{GR}(r) &= v^2_{esc,GR}(r), \\ &= -2[\phi_{GR}(r) - \phi_{GR}(r_{eq})] - qH^2[r^2 - r^2_{eq}]. \end{aligned} \tag{5.8}$$

r_{eq} is the "equivalence radius", defined to be the point at which the acceleration due to the gravitational potential of the cluster and the expanding universe are equivalent: $r_{eq} \equiv (\frac{GM_{200}}{-qH^2})^{1/3}$. q is the deceleration parameter and H is the Hubble parameter. Using Eq. 5.1, in an expanding Chameleon *f(R)* gravity universe instead we have:

$$\begin{aligned} -2\Phi_{f(R)}(r) &= v^2_{esc,f(R)}(r), \\ &= v^2_{esc,GR}(r) + \left[\delta f_R(r) - \delta f_R(r_{eq})\right]. \end{aligned} \tag{5.9}$$

Eqs. 5.7 - 5.9 use NFW parameters that have been measured from the cluster density profiles. In real data, these would be measured using the observed weak lensing shear profile around clusters which is unaffected by the effects of $f(R)$ gravity (see the appendix of Arnold et al. (2014)). Our test is then built to compare the matter-inferred GR or *f(R)* gravity potential profiles to the observed dynamical escape velocity profile.

5.3 N-body simulations

We measure the escape velocity of galaxy clusters through the technique (developed in Diaferio & Geller (1997)), in which the Newtonian gravitational potential profile is reconstructed from the escape velocity "edge", identified from the cluster radius-velocity space (i.e. the "phase space"). This is a well-developed and well-tested technique and it has been used in numerous studies of the mass profiles of galaxy clusters (Gifford & Miller, 2013a; Serra et al., 2011; Lemze et al., 2012; Rines et al., 2013; Andreon & Hurn, 2010; Geller et al., 2014). The escape edge for a given halo is constructed by taking the maximum velocity in the particle phase space for each r/R_{200} bin in 0.05 intervals. In GR simulations, the observed escape edge has been shown to recover the theoretical v_{esc} to $\sim 5\%$ accuracy, depending on the model used (Miller et al., 2016).

To construct our potential profiles from the escape velocity edge we utilize the

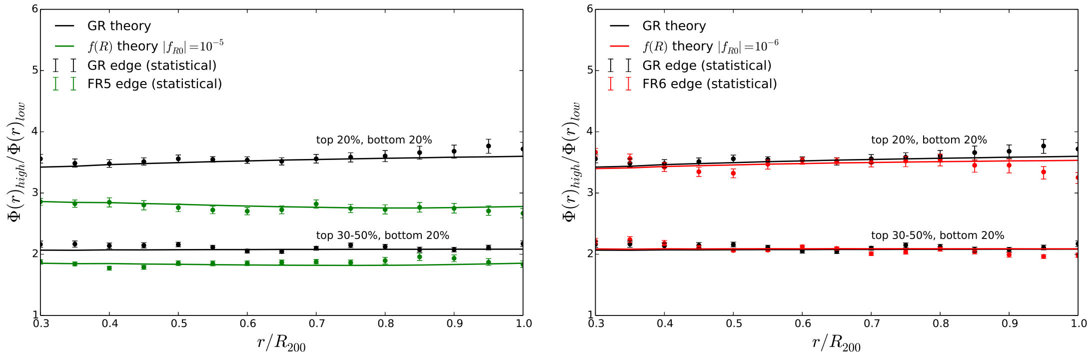

Figure 5.1: The $z = 0$ gravitational potential ratio between high and low mass bins of synthetic galaxy clusters for the GR (black), the FR5 (*left*) parametrization of $f(R)$ gravity (green), and the FR6 (*right*) parametrization (red). The points are the average of the square of the observed escape velocities for each bin in radius and mass. The errors are 1σ on the mean from boot-strap re-sampling. The solid lines represent the theoretical predictions using the NFW density parameter (Eqns. 5.7 - 5.9). Note the $\gtrsim 5\sigma$ level difference between the GR and FR5 ratios. The percentages denote how we separate the high and low mass bins. Note that the separation between GR and *f(R)* potential ratios increases with increasing separation in the mass bins.

particles in N-body simulations developed in Zhao et al. (2011a); Li et al. (2012) which have identical initial conditions, but incorporate either GR or *f(R)* as their prescriptions for gravity. The cosmological parameters used for these simulations are as follows: $\Omega_m = 0.24, \Omega_\Lambda = 0.76, h = 0.719, n_s = 0.961$ (Li et al., 2012). Here our focus is on the simulated GR, FR6, and FR5 runs. Briefly, the adaptive mesh refinement N-Body simulations take place in a 1.5 Gpc h^{-1} cube with 1024^3 resolution and a particle resolution of $6.2 \times 10^{10} M_\odot h^{-1}$. The large box size is required to provide the number of high mass clusters required in our analysis. The halos are defined by the Amiga Halo Finder or AHF (Knollmann & Knebe, 2009).

5.4 Probing gravity

To differentiate between GR and MG we probe the *ratio* of the averaged gravitational profile of high mass clusters, to the averaged gravitational potential of low mass clusters. We infer the ratio from N-body simulations through the aforementioned technique and compare our results to the aforementioned theoretical expectations for each respective theory of gravity. More specifically, our probe is encapsulated in the following equation:

$$\frac{\Phi_{high}(r)}{\Phi_{low}(r)} \equiv \frac{\langle v^2_{esc,high}(r)\rangle}{\langle v^2_{esc,low}(r)\rangle}. \tag{5.10}$$

Why separate clusters into two mass bins? The reasons are twofold. First, as shown in Falck et al. (2014) the Chameleon mechanism induces a mass dependent screening effect which leads to high mass clusters being screened and low mass clusters being increasingly unscreened. Relative to their high mass counterparts, less screened low mass clusters will exhibit higher escape velocity edges, resulting in a reduced potential ratio compared to expectations from GR. The cluster potential ratio is a smoking gun test of modified theories of gravity employing the Chameleon screening mechanism. Secondly, the ratio allows us to undercut both observational and theoretical systematics. Precisely how this ratio allows us to do so is thoroughly explained in the next section.

Now, to compare clusters in each of the three (GR, FR6, and FR5) simulations we employ one-to-one matching. We find cluster-sized over-densities at the same positions at $z = 0$ across all three simulations using a halo's center positions from an AHF-generated halo catalog (Knollmann & Knebe, 2009). We begin with 100 halos uniformly sampled in log mass between $\sim 10^{14} - 10^{15}\mathrm{M}_{\odot}h^{-1}$. The 100 halos per simulation are then binned into a *low mass bin* and a *high mass bin* each of which corresponds to selecting a percentile of the of least and most massive clusters. The specific mass bin ranges are as follows. For GR, the low mass bin is: $9.10 \times 10^{13} - 1.96 \times 10^{14} M_{\odot}h^{-1}$ and the high mass bin is: $7.48 \times 10^{14} - 1.58 \times 10^{15} M_{\odot}h^{-1}$. For FR6, the low mass bin is: $9.13 \times 10^{13} - 1.97 \times 10^{14} M_{\odot}h^{-1}$ and high mass bin is: $7.34 \times 10^{14} - 1.58 \times 10^{15} M_{\odot}h^{-1}$. For FR5, the low mass bin is: $1.16 \times 10^{14} - 1.94 \times 10^{14} M_{\odot}h^{-1}$ and the high mass bin is: $7.49 \times 10^{14} - 1.58 \times 10^{15} M_{\odot}h^{-1}$.

For each of the simulation halos, we attain both the phase space escape velocity profile through the aforementioned technique, as well as the potential profile based on matter density NFW fit (Eq. 5.5). With the former we can construct the "observed" dynamical gravitational potential profile and with the latter the prediction from GR or *f(R)* gravity. We then take the ratio between the averaged high mass edge profiles and the averaged low mass edge profiles (Eq. 5.10).

The resulting averaged profile ratios are shown in Figure 5.1. The errors are 1σ on the mean from boot-strap re-sampling with replacement. The solid lines represent the theoretical predictions using the NFW density parameter (Eqns. 5.7 - 5.10). Note that we chose to present the ratios as a function of r/R_{200} rather than r as a way to remove the side effects that arise when comparing clusters of different masses. When plotted as a function of r the potential ratio of Figure 5.1 attains a positive slope which arises as a result of different underlying mass profiles. Thus, re-scaling by each cluster's respective R_{200} flattens the profile and makes the potential ratios of Figure 5.1 a much cleaner and clearer observable: one that depends on the amplitude of the potential and not the shape of the potential profile.

As Figure 5.1 also shows, our theoretical predictions can successfully reproduce our (simulated) observable to high precision. On that figure we also plot the averaged potential ratio for different mass bins. One important conclusion from this is that the closer we bring the two mass bins, the more attenuated the difference between GR and $f(R)$ becomes. We would like to mention that dynamical differences in Fig. 5.1 are solely due to modifications to gravity and not to mass differences in the simulation. Comparing the average mass ratios: $\langle M_{200,high}\rangle/\langle M_{200,low}\rangle = 6.40, 6.39, 6.02$ for GR, FR6 and FR5 respectively, we conclude that averaged mass ratio differences are negligible when compared to the $\sim 25\%$ difference between the GR or FR6 and the FR5 potential ratios shown in Fig. 5.1.

Given our ability to precisely predict our theoretical observable (as demonstrated by Figure 5.1), we demonstrate the lower limit on how well our new probe can constrain Chameleon $f(R)$ gravity. Note, for instance, that the FR6 model, for our theoretical observable, is almost identical to GR. Furthermore, cosmic variance is the largest component of the uncertainty on the potential ratios for the small samples we examine. We study a more realistic synthetic data-set using the 2-dimensional projected phase spaces in the following sections.

5.5 Systematics

In order to assess the viability of our probe, we carefully consider relevant systematics. More specifically, we focus on: the systematic error induced by cosmic variance, statistical errors that arise from projection effects, as well as additional systematics that arise from sampling of galaxies in clusters.

One relevant systematic arises from the fact that we are using a very small sample of the clusters in the Universe to generate Figures 5.1 and 5.2. We chose this sample size as it reflects the scale of data we have today for measuring both weak-lensing profiles and also with significant spectroscopic follow-up (Rines et al., 2013; Geller et al., 2013; Hoekstra et al., 2012).

The dashed lines band as shown in Figure 5.2 incorporates the systematic uncertainty due to cosmic variance on a sample of this size (20 clusters per mass bin) which was measured to be 10% using a larger set of GR simulations (the Millennium simulations (Springel et al., 2005b)). In other words, the observed ratio $\frac{\Phi_{high}(r)}{\Phi_{low}(r)}$ can vary as much as 10% when measured for a sample size as small as ~ 20 clusters per mass bin. This is an important systematic which decreases as the sample size increases.

We also assess environmental screening, in which some fraction of the lower mass clusters in the $f(R)$ simulations could be screened due to large-scale over-densities (Zhao et al., 2011b). If this were to happen, the observed FR5 and FR6 ratios would be higher (closer to GR) than predicted by the theory. We control for random noise due to variations in the large-scale environments of the clusters by using one-to-one matching for the halos across the GR, FR5 and FR6 simulations. Also, we ensure that none of the clusters lie within the virial radii of other clusters. Finally, we can evaluate our dataset for possible effects from environmental screening using Figure 5.1, where the FR5 and FR6 predictions match our measurements to high precision. If screening were present, one would find the FR5 and FR6 measurements of the $f(R)$ simulation data to be closer to the GR simulation data. We note that the absolute accuracy of the cluster sample used in Figure 5.1 is limited by cosmic variance of order 10%. We conclude that the effects of screening on this test are smaller than systematic and statistical uncertainties on our measurements, so long as non-merging clusters are chosen for the analysis.

We use the Millennium simulations with the light cone data provided by Henriques et al. (2012) to investigate projection effects, which is likely the dominant component of the error on the potential ratio. To carry out our proposed test with physical (rather than synthetic) data, the escape velocity profile of a cluster would be inferred from the line-of-sight velocities of galaxies in that given cluster, rather than the radial component of the 3D velocity. Fortunately we can transform, roughly, the line-of-sight velocities into 3D velocities and vice versa. As shown in Diaferio (1999) the mapping between the radial 3D escape velocity profile considered above ($v_{esc}(r)$) and the line-of-sight escape velocity profile inferred from data ($v_{esc,los}(r)$) is as follows:

$$v^2_{esc,los}(r) = g^{-1}(\beta) \times v^2_{esc}(r) \tag{5.11}$$

Where $g(\beta)$ is given by $g(\beta) = 3 - 2\beta(r)/1 - \beta(r)$ and is of $\mathcal{O}(1)$. $\beta(r)$ is given by $\beta(r) = 1 - \langle v^2_\theta + v^2_\phi \rangle / 2\langle v^2_r \rangle$ (Diaferio, 1999). As such, in projected space Eq. 5.10 is instead,

$$\frac{\Phi_{high,los}(r)}{\Phi_{low,los}(r)} \equiv \frac{\langle g(\beta_{low}) \rangle}{\langle g(\beta_{high}) \rangle} \frac{\langle v^2_{esc,high}(r) \rangle}{\langle v^2_{esc,low}(r) \rangle}. \tag{5.12}$$

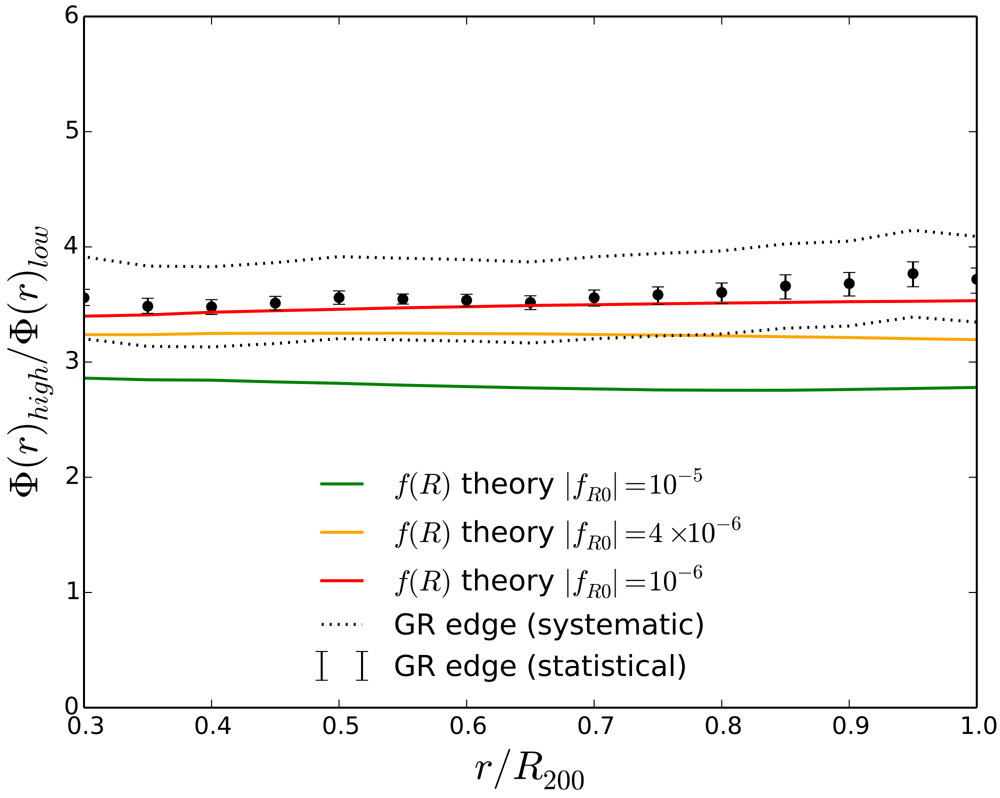

Figure 5.2: The simulated and theoretical averaged GR and $f(R)$ gravity potential ratios for the same clusters of Figure 5.1 (top 20% and bottom 20% mass bins). We have added the theoretical prediction for $|f_{R0}| = 4\times10^{-6}$ gravity (yellow) and include not only the GR statistical error on the mean (black error bars) but also the 10% systematic error due to cosmic variance (black dashed lines). This figure demonstrates how we would detect and/or constrain MG. Assuming GR as our "observation," the data is contained within the black dashed bands. We can therefore ask the question: which of the three plotted models best describes the data? We conclude our probe can, including systematics, successfully discern between GR and $|f_{R0}| = 4 \times 10^{-6}$ at 1σ.Note that this result is attained with only 40 clusters (20 in each mass bin) and the potential is inferred from 3-dimensional phase space synthetic data. We reproduce this plot for a projected DESI-like data-set in Fig. 5.4.

However, the ratio of the averaged $g(\beta)$ profiles for high and low mass systems is $\langle g(\beta_{high})\rangle/\langle g(\beta_{low})\rangle \approx 1$ and so the line-of-sight potential ratio is the same as the 3D potential ratio:

$$\frac{\Phi_{high,los}(r)}{\Phi_{low,los}(r)} \approx \frac{\Phi_{high}(r)}{\Phi_{low}(r)} \tag{5.13}$$

Therefore, our expectation is that by dividing out the averaged cluster potential profiles we eliminate the necessity to estimate the anisotropy profile. We note that another observational challenge lies in eliminating line-of-sight galaxies that may not be cluster members and will therefore contaminate our phase space.

We recognize that there exist few observational surveys containing clusters around the mean mass in our low-mass subsample. However, with new imaging and spectroscopic surveys, we expect future datasets to provide excellent weak lensing mass profiles as well as significant spectroscopic follow-up.

Therefore, we consider two cases of projection. The first uses an ensemble cluster dataset, where the weak-lensing mass profiles and the spectroscopic potential profiles are inferred from averaged or stacked datasets as would be measured using current facilities. The second uses a much larger sample of clusters based on deeper data, where the weak-lensing and spectroscopic potential profiles could be measured individually for the clusters and then averaged.

5.5.1 Stacked cluster ensembles

To build a cluster ensemble we superimpose the phase-spaces of individual clusters. In particular, we use 500 galaxies per phase space with 10 high mass and 10 low mass clusters to create a high and a low mass cluster ensemble. The masses of the clusters are chosen to match the average masses of the sample used in Figs. 5.1 and 5.2. The galaxies used to populate the phase spaces are all brighter than an r-band magnitude of 17.7 and the clusters are within $z = 0.15$ such that this is an SDSS-like stacked ensemble of clusters. As before, we compute the averaged potential ratios (Eq. 5.10) and the boot-strapped error bars. The result is shown on Fig. 5.3 (solid gray line). The scatter dots with statistical error represent the 3D inferred edge (as in Fig. 5.1 and Fig. 5.2). We find that over the range $0.4 \leq r/R_{200} \leq 0.9$, the 2D projected and the 3D ratios are statistically identical. At the same time, our constraints on $|f_{R0}|$ are robust to small (5%) corrections in the ratio as we go from 3D to 2D. This confirms the expectation detailed above which speculated that the averaged ratio of potential profiles allows us to undercut complications that arise from working with projected data. However, Fig. 5.3 also shows that the errors from projection are as

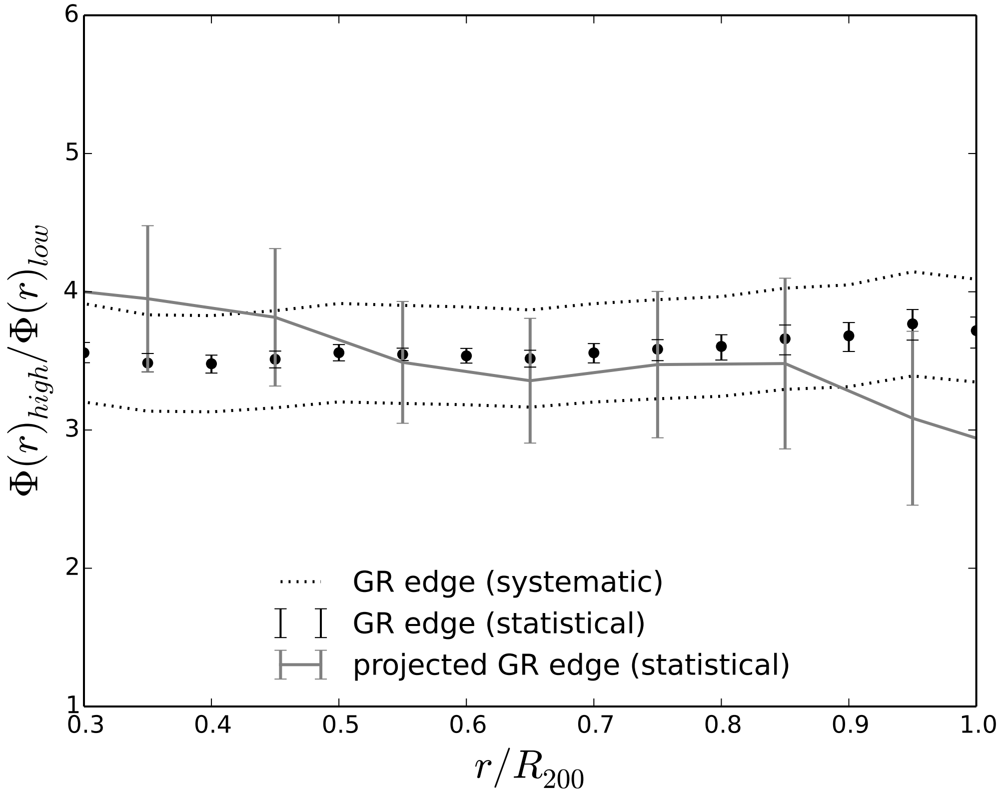

Figure 5.3: The gravitational potential ratio of Fig. 5.1 (black dots with statistical error) and the gravitational ratio as inferred from an ensemble of clusters (gray line with statistical error) from the light cone data of Henriques et al. (2012). The high and low mass cluster ensembles are made up of 5 different ensembles each with 10 clusters that include 500 galaxies each. The error bars are 1σ error on the mean from boot-strap re-sampling. This nearly flat transfer function incorporates numerous observational systematics when going from 3D to realistic observational data.

large as cosmic variance for a small sample of ∼20 clusters.

5.5.2 DESI Bright Galaxy Sample forecast

In order to decrease the errors, we investigate a much larger (by a factor of ~ 10) sample of clusters. Within the Henriques light cone (Henriques et al., 2012) we generate a Dark Energy Spectroscopic Instrument (DESI) Bright Galaxy Sample-like selection function. While for the previous studies we constrained the observed galaxy population to brighter than the SDSS main sample, we now use galaxies to an r-band magnitude limit of 19.1. We still focus on clusters within $z = 0.15$. The deeper magnitude limit increases the number of clusters with greater than 50 galaxies in the phase space to many hundreds per mass bin. This sample is an approximation to what may be observed with DESI and would allow us to probe both a wider and deeper sample of the sky, thereby undercutting the effects of cosmic variance and increasing the total number of galaxy clusters in our sample.

We re-create the mass bins chosen in the previous sample by choosing clusters with masses between $10^{14}/h < M_{200}/M\odot < 2.1 \times 10^{14}/h$ for the low mass sample, and $M_{200}/M\odot > 6 \times 10^{14}/h$ for the high mass sample. The average mass for the low and high mass sample respectively are: $1.4 \times 10^{14} M\odot/h$ and $8.2 \times 10^{14} M\odot/h$. From those two mass bins we then make a conservative cut by picking clusters that contain at least 50 galaxies between $|v_{los}| \leq 2000$ km/s within 3 Mpc from the cluster center.

To predict the potentials in this sample, we use the halo masses of each cluster and derive concentrations from the mass-concentration relation provided in Duffy et al. (2008): $c_{200}(M_{200}, z) = A_{200}(M_{200}/M_{pivot})^{B_{200}}(1+z)^{C_{200}}$. Where $A_{200} = 5.71$, $B_{200} = -0.084$, $C_{200} = -0.47$ and $M_{pivot} = 2 \times 10^{12} M_{\odot} h^{-1}$. This sample assumes that weak lensing masses are unbiased. The width of our mass bins are larger than the one sigma mass scatter in the weak lensing observable (Becker & Kravtsov, 2011). Because of the wide width of our mass bins, we can ignore weak lensing mass uncertainties when calculating the theoretical predictions.

In Figure 5.4, we show the averaged potential ratio between the two mass bins (Eq. 5.10) with both statistical (boot-strapped as before) and systematic error (cosmic variance) for the aforementioned DESI-like sample. As before, we also show the theoretical predictions for both GR and $f(R)$ gravity. Several conclusions regarding systematics affecting our probe may be drawn from Figure 5.4:

- Our GR 3D theory (solid black line) can accurately predict the potential ratio generated with projected synthetic data. This confirms that we can successfully divide out projection effects by taking the ratio of averaged potentials (as implied by Eqns. 5.12 and 5.13).

- Projection effects increase the statistical error relative to the unrealistic 3D ratio. This is expected and discussed in Gifford & Miller (2013b). In particular, compare the few percent statistical error on the 3D ratio of Figs 5.1-5.2 with the $\sim 8\%$ statistical error of Fig. 5.4. However, while projection increases the statistical error on the ratio, the cosmic variance of a larger sample goes down as the square root of the fractional increase in the sample size, which for a DESI-like sample is ~10 times as many clusters as used in our previous results (Figures 5.1, 5.2, and 5.3.)

- The phase spaces only need to be moderately populated with 50 galaxies between $|v_{los}| \leq 2000$ km/s within 3 Mpc from the cluster center. This is necessary in order to measure the escape velocity edge. By selecting the 50 brightest galaxies to create the phase spaces, the test is immune to color bias, at least to the level probed by the simulated galaxy catalog. We also find that if we underpopulate the phase space, we can bias our low mass cluster potential profiles. This is a known effect and studied in detail in Gifford & Miller (2013a).

We also investigate whether the assumed mass-concentration relation affects our potential ratios. We examine a range of uncertainties in the parameters which describe the relation and find that the potential ratio profiles vary less than 1%. This is because all mass-concentrations relations are quite flat at the cluster masses we study here and also because the mass difference between the high and low mass sub-samples is quite small.

Generally, we note that the utilization of the ratio of potentials mitigates systematic effects of the observables and theory beyond the aforementioned projection effects. For instance, Miller et al. (2016) found that NFW density profiles predict NFW potentials that are biased high by 10-20%. Einasto profiles on the other hand show <5% biases. However, they also showed that there is no difference between the predicted and observed phase space escape velocities as a function of halo mass. We tested that by comparing the GR prediction from Eq. 5.10 using NFW density fits to the more accurate Einasto density profile fits. We find that the ratios agree to within a percent. In other words, while the NFW mass profile systematically overestimates the cluster potential profiles, the ratio of NFW potentials is unbiased. Similar arguments can be made about other possible systematics, including line-of-sight effects, velocity bias, and velocity anisotropies as mentioned in the bullet points above (Svensmark et al., 2015; Gifford & Miller, 2013a; Lemze et al., 2012).

5.6 Statistical Constraints on $f(R)$ gravity

Given our analysis of systematics detailed above, we can provide a robust estimate of how well our probe will be able to constrain MG on the two different cluster samples we simulate. To differentiate between GR and $f(R)$ gravity, we assume that we live in a GR universe with a ΛCDM cosmology, and calculate the χ^2 between this measurement and the theoretical expectations of the various $f(R)$ gravity models. The error on the GR measurements arises from two sources: (1) the statistical error from boot-strap re-sampling of the mean and (2) the systematic error that takes into account the cosmic variance. Therefore, the variance used in our χ^2 calculation in what follows is taken to be these combined statistical and systematic errors added in quadrature.

We first compare against a stacked ensemble of clusters. In particular, we assume an SDSS-like cluster sample with 10 stacked clusters per ensemble and 5 cluster ensembles per mass bin. Recall that individually the clusters are too poorly sampled in their spectroscopy. However, the two ensemble clusters would have a high signal-to-noise weak lensing mass profile as well as a well-determined escape velocity profile. In this case, the cosmic variance term dominates the error budget. More specifically, we take the gray error bands on Figure 5.3 and we calculate what value of $|\overline{f_{R0}}|$ would yield a ratio profile (assuming the same GR masses) that is 2σ away via the χ^2 test mentioned in the previous paragraph. What we find is that we can differentiate GR from $|\overline{f_{R0}}| = 5.5 \times 10^{-6}$ at 2σ.

By increasing the sample size we can improve these constraints. In particular, as shown in Fig. 5.4, we show that with the DESI-like sample of galaxy clusters, we can constrain $|\overline{f_{R0}}| = 4 \times 10^{-6}$ (2×10^{-6}) at $> 5\sigma$ $(> 2\sigma)$ by doing the same aforementioned χ^2 calculation but now using the black dots (and errors) shown in Fig. 5.4 as our "measurement."

These are competitive forecasts compared with the two most recent galaxy cluster-scale constraints. For example, Wilcox et al. (2015) presents an analysis of 58 clusters in the XMM sample that constrains $|\overline{f_{R0}}| < 6 \times 10^{-5}$ at the 95% confidence level (CL). Similar to the potential ratio test presented here, Wilcox et al. (2015) focuses only on cluster scales, i.e., within the virialized region of clusters. Using stacking on only 50 clusters per mass bin and after including both statistical and systematic uncer-

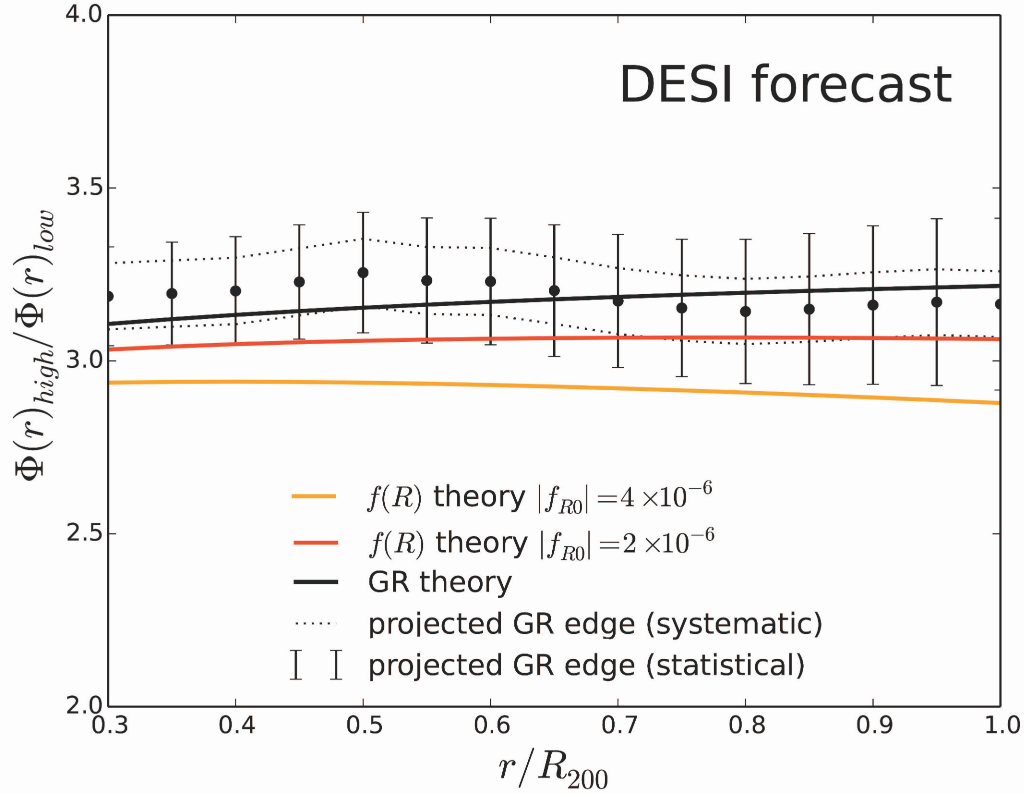

Figure 5.4: The projected gravitational potential ratio for a DESI-like galaxy cluster sample (black dots and bootstrap error on the mean) as inferred from synthetic galaxy clusters from the light cone provided by Henriques et al. (2012). Compared to Fig.5.2 (where the ratio is inferred from a 3D phase space) we see that projection significantly increases the statistical error. The DESI sample is significantly larger as it contains 9.6 times many more clusters and so the systematic error is significantly reduced (286 low mass clusters and 96 high mass clusters). From this we can determine which gravitational theory best matches the "observation." To visualize this, we plot both the GR theoretical prediction (black line) and two $f(R)$ theoretical predictions (orange-red and yellow). We conclude that our probe can differentiate between GR and $|\overline{f_{R0}}| = 4 \times 10^{-6}$ (2×10^{-6}) at $> 5\sigma$ $(> 2\sigma)$.

tainties on the observable, our potential ratio test can achieve an order-of-magnitude improvement over observational constraints set by Wilcox et al. (2015). The most competitive cluster-scale constraint is set by Cataneo et al. (2015) with a cluster abundance analysis. They find that $|\overline{f_{R0}}| < 1.62 \times 10^{-5}$ at 95% CL. With the the DESI-like sample, our test should be able to differentiate $|\overline{f_{R0}}| = 1.62 \times 10^{-5}$ and GR at $>> 5\sigma$.

5.7 Summary

In this chapter, we propose a new test of gravity within galaxy clusters that leverages the ways in which modifications to gravity alter the dynamical potential while leaving the weak-lensing inferred potential profile unchanged. We take the ratio of the squared escape velocity profile for high and low mass clusters as our observable. We do this for two reasons: 1) it leverages the fact that Chameleon screening leaves the dynamics of the high mass clusters unaffected compared to the low mass clusters and 2) it removes any systematic that is present in both samples, such as velocity bias and velocity anisotropy. While this test can be applied generally to any new model for gravity which has this property, we test it against Chameleon $f(R)$ gravity.

We first use simulations to show that particles, as tracers of the dynamical gravitational potential within galaxy clusters, do have enhanced escape velocity profiles compared to expectations from their non-dynamical (i.e. particle) masses. We then use mock galaxy catalogs to understand the role of systematics in quantifying how well we can rule out $f(R)$ gravity. We study two cases. The first utilizes a realistic but rather small number of clusters which we stack to create 2 cluster ensembles with different mass bins. We also study a second dataset which is much larger and more representative of what we expect from future surveys. In the former, cosmic variance dominates the systematic error budget, while in the latter 2D projection effects dominate. In either case, we find that our probe is more sensitive, by an order of magnitude, over current cluster-based tests for Chameleon $f(R)$ gravity. More specifically, we have quantified our prediction for a DESI Bright Galaxy Sample-like set of clusters to push down current constraints to $|\overline{f_{R0}}| < 2 \times 10^{-6}$ at $> 2\sigma$.

CHAPTER VI

Openings

This dissertation proposes and tests a new way to model the projected escape velocity profile of galaxy clusters by including the effects of our accelerating universe. From this model, we have argued that if the projected escape velocity profiles can be de-projected through an independent measurement of the anisotropy parameter β, then we could utilize the cosmology dependence as a novel probe of cosmology. We have developed such an approach to derive β profiles. Moreover, with the Fisher information matrix formalism we have calculated how well this theoretical observable can constrain relativistic cosmological models. Lastly, dropping the presupposition that general relativity is the only way to theorize gravity, we have developed a novel probe of Chameleon $f(R)$ gravity that utilizes the escape velocity profile's sensitivity to changes in the gravitational potential.

In these closing remarks we attempt to briefly sketch out some possible openings and lines of research that this dissertation has made evident. More specifically, we provide some critical reflections (some more specific than others) as well as speculate on possible ways of continuing to grapple with some of the problems and possibilities posed by this work.

6.1 The cosmology and redshift dependent v_{esc}

As presented in Chapter IV, our cosmological probe can currently constrain accelerating cosmologies to high precision. However, the balance of forces argument with which we derive our theoretical expectation for the escape velocity profile (see Chapter II) is not directly applicable in a non-accelerating universe. In particular, as z approaches the deceleration-to-acceleration transition redshift, we recover the non-cosmology dependent result (ie. the result derived from integrating the acceleration equation to infinity rather than to the equivalent radius). As such, more theoretical work needs to be done to be able to make the theoretical observable sensitive to cosmology at epochs beyond the deceleration-to-acceleration transition redshift.

We note that beyond that redshift (which is, of course, cosmology dependent) clusters are just forming and therefore the probe could not be practically used beyond it. Furthermore, an extensive constellation of cosmological probes all provide independent lines of evidence that $q_0 > 0$. Given these two reasons one could ask: why would we propose that this be further investigated?

For one, as shown in Chapter II, one of the consequences of our model is that at high z, the escape velocity profiles increases. See for instance Fig. 2.1 – increasing the Ω_M parameter at a fixed redshift increases the escape velocity profile. This behavior is equivalent to placing the cluster in an epoch where Ω_M is higher (namely, at higher z). While we have implicitly corroborated our theoretical observable works with both N-body simulations and archival cluster data we have not studied the behavior of neither the escape velocity edge of clusters (neither synthetic nor real) at (or near) the transition redshift for different cosmologies.

In short, our model predicts that a very high redshift cluster would have a higher escape velocity than a cluster of the same mass at a lower redshift. We should be able to test this prediction more directly than we have in this dissertation– especially given the proliferation of deep and high quality spectroscopic measurements from observational programs such as the Dark Energy Spectroscopic Instrument (DESI) as well as the proliferation of suites of N-body simulations with different cosmologies.

6.2 Probing modified theories of gravity: redshift dependence and radius

As we argued in the previous chapter, the test of gravity we propose in this thesis is designed to leverage the next generation large-scale photometric and spectroscopic surveys (e.g., the Dark Energy Survey (Diehl et al., 2014) and the Dark Energy Spectroscopic Instrument–DESI) that will provide high quality weak-lensing mass profiles of clusters as well as deep and plentiful spectroscopic follow-up of the cluster phase spaces. Furthermore, while we focus on scales within the virial sphere, we note that the difference between the GR and $f(R)$ gravity ratio increases as we go out to larger radii. This is due to the scalaron's fifth force being more effective in the outskirts of clusters where the density is lower. We also note that the difference between the GR and $f(R)$ gravity decreases with increasing redshift. We have not yet included these effects in our statistical analysis, but we expect that they will prove useful in setting even tighter constraints. In short, we hope that these expectations will be probed in a future effort.

6.3 To stack or not to stack?

In both Chapter IV and Chapter V we grapple with the possibilities and challenges of two different observational strategies that could roughly be reduced to the following question: should we stack galaxy clusters or not? Put differently, should our observational strategy be focused on obtaining deep spectroscopy of individual clusters (i.e. have well-sampled phase spaces with a high level of completeness to clearly determine the escape velocity edges) or on attaining less well-sampled individual cluster phase spaces (perhaps with a broader redshift range) in order to stack them by mass (or richness)? Recall that for both of our probes, the phase space catalogs would have to be cross-correlated with weak lensing mass profile catalogs. For the case of the individual cluster observational strategy, therefore, this would require observing clusters in such a way to attain both a well-sampled phase space and a high signal-to-noise weak lensing shear profile. What we want to highlight, then, is that for both the cosmology and modified gravity probes, given the current horizon of observational programs, the stacked analysis may be the most viable option to set the tightest constraints.

As an example, take a recent publication (Rines et al., 2017) which significantly extends the Hectospec Cluster Survey of red-sequence selected cluster (HeCS) sample that is cross-correlated with the redMaPPer catalog (Rykoff et al., 2014). This catalog, even though it is composed of clusters with very well-sampled phase spaces, is low redshift ($z \leq 0.25$). A similar situation happens with DESI, as is discussed in the preceding chapters. As such, in the short-term, creating a cluster sample of $N = 1000$ in a broad redshift range ($0 \leq z \leq 0.7$) with well-sampled phase spaces and high-to-noise weak lensing mass profiles may imply that, for now, stacking is the only solution to achieve competitive constraints.

However, stacking (both in terms of cluster phase spaces and weak lensing signals) has its own complications. In relation to the latter, problems related to miscentering (which especially affects cluster cores and thereby the inferred cluster concentration parameter) and purity are two of the dominant systematics. See, for example, Becker & Kravtsov (2011b) and Rozo et al. (2011) and references therein to appreciate how these systematics affect the inferred weak lensing masses and how their effects can be undercut. In relation to the former, Gifford et al. (2017) has studied different ways of stacking galaxy cluster phase spaces and throughly quantified the systematics at work.

As such, we expect that work which attempts to further develop the probes presented in this dissertation in the context of the aforementioned systematics related to stacking may prove to be fruitful in setting tight constraints of both relativistic cosmologies and modified theories of gravity in the near future.

6.4 Toward a global galaxy cluster velocity anisotropy

While our specific derivation of the cluster velocity anisotropy profile (via the Jeans equation formalism, as shown in Chapter III) is shown to be either weakly dependent or independent from the chosen potential-density pair, this is only because we have chosen to avoid the inner-most core region of the galaxy cluster. If we had not done that, both the density and the spatial derivatives of the potential diverge both deep in the core and in the outskirts of clusters. In particular, the NFW potential-density pair model is higher in both the core and the outskirts than the results attained with the Einasto model. This model-dependence should also be further studied in the context of the mass-dependence of β. Furthermore, we note that if there is indeed a mass dependence, it could introduce a small bias in our probe of Chameleon gravity, given that this probe depends precisely on the assumption that β for high masses is about the same as β for low masses.

Lastly, we want to emphasize that until this work, only one other work (that of Wojtak & Łokas (2010)) utilized a statistically robust sample ($N \gtrsim 30$) to derive a "global" anisotropy parameter value with currently available data. Our approach to derive β's is dependent on joint dynamical and weak lensing measurements of galaxy clusters. Therefore, we hope that the proliferation of measurements on this front will put even tighter constraints on the global anisotropy profile value.

6.5 Something always escapes

The core of the argument worked out in this dissertation is just a mere coming to terms with the dynamical character of our cosmos in the scale of galaxy clusters– from which we then draw conclusions for our cosmological models and gravitational theories. While today it is "common sense" that the universe is accelerating, the consequences of this had neither been brought to bear with the dynamics of clustered galaxies nor with the theoretical observable we work with through this thesis – the escape velocity of galaxy clusters. The exception, as mentioned in Chapter II, has been the seminal work of Regoes (1996) and Regoes & Geller (1989b) which attempted to investigate the cosmological dependence of the caustics through the spherical collapse model.

In these works, as well as in ours, we sense a certain vacillation between the relativistic intuition of gravitation as the curvature of space and the Newtonian intuition of forces at a distance acting between massive bodies. Galaxy clusters then, in some sense, exist in a regime where the Newtonian intuition still makes sense but must be complemented by that of relativistic cosmology. We speculate that this is perhaps symptomatic of our epoch–which still thinks in the wake of the shift of paradigm that general relativity represented but has not fully come to terms with its consequences. We also emphasize that this is a self-criticism that challenges the presuppositions at work in this dissertation (for instance, in multiple instances, such as in the definition of the equivalence radius, we still speak of "forces"). Perhaps coming to terms with the consequences of this shift, and what this implies for our so called "eternal" laws of nature is still a task that faces us.

Modified theories of gravity such as the one studied in this dissertation are an attempt to do just that. While we agree that these theories are simply "toy models" and not fully developed theories, they may still nonetheless point to the ways in which a full theory may be developed. In particular, these theories implicitly make the case that perhaps our so called "laws of nature" are not eternal and unchanging but emerge from the contingent character of our universe. And yet, our dynamical universe demonstrates a tremendous degree of regularity and repetition.

So, in that sense, this work is an attempt to continue to inhabit the patterns and regularities that necessarily emerge out of the radical contingency and dynamical character of our cosmos which, despite our best attempts to capture its dynamics, continues to escape even our most convincing characterizations.

APPENDICES

APPENDIX A

Derivation of qH^2 for various cosmological cases

In what follows we derive the Hubble and deceleration parameters for cosmologies of interest, used in Chapter V, via the general expression,

$$H^2 = H_0^2 E^2(z) = H_0^2 \left[\Omega_M(1+z)^3 + \Omega_k(1+z)^2 + \Omega_{DE} \exp\left\{ 3 \int_0^z \frac{dz}{(1+z')}[1+w(z')] \right\} \right]. \tag{A.1}$$

Where the spatial curvature density parameter is as usual, $\Omega_k = 1 - \Omega_M - \Omega_{DE}$. Furthermore, once we have the Hubble parameter as a function of redshift we can derive the corresponding deceleration parameter, $q \equiv -\ddot{a}a/\dot{a}^2$, as a function of redshift via,

$$q = \frac{(1+z)}{H}\frac{dH}{dz} - 1. \tag{A.2}$$

As such, finding q is just a matter of taking derivative with respect to z.

Constant equation of state w

The Hubble parameter for this flat case is straightforward,

$$H^2 = H_0^2 E(z)^2 = H_0^2 \left[\Omega_M(1+z)^3 + \Omega_{DE}(1+z)^{3(1+w_0)} \right] \tag{A.3}$$

And so are the derivatives,

$$\frac{dH}{dz} = \frac{H_0}{2} \frac{3\Omega_M(1+z)^2 + \Omega_{DE}(3(1+w_0))(1+z)^{3(1+w_0)-1}}{\sqrt{\Omega_M(1+z)^3 + \Omega w_0(1+z)^{3(1+w_0)}}} \tag{A.4}$$

But we can identify the denominator as $E(z)$, and from there we can find $q(z)$,

$$\frac{1+z}{H}\frac{dH}{dz}-1=\frac{1+z}{H_0E(z)}\frac{H_0}{2}\frac{3\Omega_M(1+z)^2+\Omega_{DE}(3(1+w_0))(1+z)^{3(1+w_0)-1}}{E(z)}-1 \tag{A.5}$$

Multiplying and dividing by $E^2(z)$,

$$q=\frac{1}{E^2(z)}\left[\frac{3}{2}\Omega_M(1+z)^3+\frac{3}{2}\Omega_{DE}(1+w_0)(1+z)^{3(1+w_0)}-\Omega_M(1+z)^3-\Omega_{DE}(1+z)^{3(1+w_0)}\right] \tag{A.6}$$

And so we have,

$$q=\frac{1}{2}\Bigg(\Omega_M(z)+(1+3w_0)\Omega_{DE}(z)\Bigg) \tag{A.7}$$

w_0 and w_a

For the case of dynamic dark energy we utilize the generalized Hubble term in terms of the scale factor to make the integration more straightforward,

$$H^2(a)=H_0^2\left[\Omega_M a^{-3}+\Omega_k a^{-2}+\Omega_{DE}\exp\left\{3\int_a^1\frac{da'}{a'}[1+w(a')]\right\}\right] \tag{A.8}$$

Where $\Omega_k=1-\Omega_M-\Omega_{DE}$. But here we consider the flat case. As such, $\Omega_k=0$.

Now, assuming the CPL parametrization of dark energy,

$$\begin{aligned} w(a)=&w_0+w_a(1-a)\\ w(z)=&w_0+w_a\frac{z}{1+z} \end{aligned} \tag{A.9}$$

We calculate the term in the exponential for the Hubble parameter above,

$$\begin{aligned} \int_a^1\frac{da'}{a'}[1+w(a')]=&\int_a^1\frac{da'}{a'}[1+w_0+w_a-w_aa'))]\\ =&(1+w_0+w_a)\int_a^1\frac{da'}{a'}-w_a\int_a^1 da'\\ =&-(1+w_0+w_a)\ln(a)-w_a[1-a] \end{aligned} \tag{A.10}$$

Taking the exponential,

$$\exp\Bigg\{-3(1+w_0+w_a)\ln(a)-3w_a[1-a]\Bigg\}=a^{-3(1+w_0+w_a)}e^{-3w_a(1-a)} \tag{A.11}$$

Turning the term back into redshift, using $a = (1+z)^{-1}$ and $1 - a = z/(1+z)$, we get:

$$\exp\left\{3\int_a^1 \frac{da'}{a'}[1 + w(a')]\right\} = (1+z)^{3(1+w_0+w_a)}e^{-3w_a z/(1+z)} \tag{A.12}$$

And so for the flat universe dynamic dark energy we have,

$$\begin{aligned} H^2(z) =& H_0^2 E(z)^2 \\ =& H_0^2\left[\Omega_M(1+z)^3 + \Omega_{DE}(1+z)^{3(1+w_0+w_a)}e^{-3w_a z/(1+z)}\right] \end{aligned} \tag{A.13}$$

Now we need to also calculate the acceleration parameter which is non-trivial. It is not just a matter of replacing w with $w(z)$. As such, we utilize the following general expression for the deceleration parameter shown above,

$$q = \frac{(1+z)}{H(z)}\frac{dH(z)}{dz} - 1 \tag{A.14}$$

Taking the derivatives of $H(z)$ shown above with $\Omega_k = 0$ and using the CPL parametrization of $w(z)$,

$$\begin{aligned} \frac{dH}{dz} =& \frac{3H_0(z+1)e^{-\frac{3w_a z}{z+1}}\left(\Omega_{DE}(w_0 z + w_0 + w_a z + z + 1)(z+1)^{3(w_0+w_a)} + \Omega_M(z+1)e^{\frac{3w_a z}{z+1}}\right)}{2\sqrt{\Omega_{DE}e^{-\frac{3w_a z}{z+1}}(z+1)^{3(w_0+w_a+1)} + \Omega_M(z+1)^3}} \\ =& \frac{3}{2}\frac{H_0}{E(z)}\left(\Omega_M(1+z)^2 + \Omega_{DE}\big(w_0 z + w_0 + w_a z\big)(1+z)^{3(w_0+w_a)+1}e^{\frac{-3w_a z}{z+1}}\right) \\ =& \frac{3}{2}\frac{H_0}{E(z)}\left(\Omega_M(1+z)^2 + \Omega_{DE}\left[1 + w_0 + \frac{w_a z}{1+z}\right](1+z)^{3(w_0+w_a)+2}e^{-\frac{3w_a z}{1+z}}\right) \end{aligned} \tag{A.15}$$

Where in the last step we have used the following factorization,

$$\begin{aligned}1+z+w_0z+w_0+w_az =&(1+z)\left[1+\frac{1}{1+z}(w_0z+w_0+w_az)\right]\\ =&(1+z)\left[1+\frac{1}{1+z}(w_0(1+z)+w_az)\right]\\ =&(1+z)\left[1+w_0+\frac{w_az}{1+z}\right]\end{aligned} \tag{A.16}$$

Now multiplying,

$$\begin{aligned}q =&\frac{1+z}{H_0E(z)}\frac{3}{2}\frac{H_0}{E(z)}\left(\Omega_M(1+z)^2+\Omega_{DE}\left[1+w_0+\frac{w_az}{1+z}\right](1+z)^{3(w_0+w_a)+2}e^{-\frac{3w_az}{1+z}}\right)-1\\ =&\frac{3}{2}\frac{1}{E^2(z)}\left(\Omega_M(1+z)^3+\Omega_{DE}\left[1+w_0+\frac{w_az}{1+z}\right](1+z)^{3(1+w_0+w_a)}e^{-\frac{3w_az}{1+z}}\right)-1\\ =&\frac{1}{2}\frac{\Omega_M(1+z)^3}{E^2(z)}+\frac{1}{E(z)^2}\Omega_{DE}(1+z)^{3(1+w_0+w_a)}e^{-\frac{3w_az}{1+z}}\left(\frac{3}{2}\left[1+w_0+\frac{w_az}{1+z}\right]-\frac{2}{2}\right)\\ =&\frac{1}{2E^2(z)}\left[\Omega_M(1+z)^3+\Omega_{DE}(1+z)^{3(1+w_0+w_a)}e^{-\frac{3w_az}{1+z}}\left(1+3w_0+\frac{3w_az}{1+z}\right)\right]\end{aligned} \tag{A.17}$$

Re-writing the redshift-evolving energy densities, we now have,

$$q=\frac{1}{2}\left[\Omega_M(z)+\Omega_{DE}(z)\left(1+3w_0+\frac{3w_az}{1+z}\right)\right] \tag{A.18}$$

Non-flat universe, Ω_M and Ω_Λ

We follow the same approach as before and write down the Hubble parameter for this case,

$$H^2=H_0^2E(z)^2=H_0^2\left[\Omega_M(1+z)^3+\Omega_\Lambda+\Omega_k(1+z)^2\right] \tag{A.19}$$

Taking the derivative,

$$\frac{dH}{dz}=\frac{H_0}{2}\frac{1}{E(z)}\left[3(1+z)^2\Omega_M+2\Omega_k(1+z)\right] \tag{A.20}$$

Now solving to get $q(z)$ and following the steps as before (ie multiplying and dividing by $E^2(z)$ in the second term and so on),

$$\begin{aligned}\frac{1+z}{H}\frac{dH}{dz} - 1 =& \frac{(1+z)}{H_0 E(z)}\frac{H_0}{2}\frac{3(1+z)^2\Omega_M + 2\Omega_k(1+z)}{E(z)} - 1 \\ =& \frac{1}{E(z)^2}\left[\frac{3}{2}(1+z)^3\Omega_M + \Omega_k(1+z)^2 - \Omega_M(1+z)^3 - \Omega_\Lambda - \Omega_k(1+z)^2\right] \\ =& \frac{1}{E(z)^2}\left[\frac{1}{2}(1+z)^3\Omega_M - \Omega_\Lambda\right]\end{aligned} \tag{A.21}$$

And so we have,

$$q = \frac{1}{2}\Omega_M(z) - \Omega_\Lambda(z) \tag{A.22}$$

APPENDIX B

Fisher matrix derivation

In the following pages, we derive the Fisher matrix (F_{ij}) discussed in Chapter V. Generally, the Fisher information is given by the second order term of the Taylor expansion of the likelihood evaluated around the peak,

$$F_{ij} = \left\langle -\frac{\partial^2 \ln \mathcal{L}}{\partial p_j \partial p_j} \right\rangle \tag{B.1}$$

Where the likelihood ($\mathcal{L}$) is assumed to be gaussian. Furthermore, the errors on the edge (σ_v^2) are all independent and taken to be constant (covariance is nil) and so we have simply:

$$\begin{aligned} \ln \mathcal{L} &= -\frac{\chi^2}{2} \\ &= -\frac{1}{2} \sum_{j,k} \frac{1}{\sigma_v^2} (v^{th}(r) - v^{obs}(r))^2 \end{aligned} \tag{B.2}$$

Where we are summing over both j clusters as well as k radial bins. In what follows, for simplicity, we drop the radial function nomenclature and denote the addition over both j and k simply as n. Now, putting this into the derivatives above,

$$\begin{aligned} F_{ij} =& \frac{1}{2}\frac{\partial^2}{\partial p_i \partial p_j}\left(\sum_n \frac{1}{\sigma_v^2}(v^{th} - v^{obs})^2\right) \\ =& \frac{1}{2\sigma_v^2}\frac{\partial^2}{\partial p_i \partial p_j}\left(\sum_n (v^{th} - v^{obs})^2\right) \\ =& \frac{1}{2\sigma_v^2}\sum_n \frac{\partial^2}{\partial p_i \partial p_j}\left((v^{th})^2 - 2v^{th}v^{obs} + (v^{obs})^2\right) \end{aligned} \tag{B.3}$$

Immediately we notice that the derivatives of v^{obs} are zero given that these are just constant numbers. Let us calculate the remaining derivatives for the first and middle terms respectively. For the first term we have,

$$\begin{aligned} \frac{\partial}{\partial p_i}\left(\frac{\partial}{\partial p_j}\left((v^{th})^2\right)\right) =& \frac{\partial}{\partial p_i}\left(2v^{th}\frac{\partial v^{th}}{\partial p_j}\right) \\ =& 2\frac{\partial v^{th}}{\partial p_i}\frac{\partial v^{th}}{\partial p_j} + 2v^{th}\frac{\partial^2 v^{th}}{\partial p_i \partial p_j} \end{aligned} \tag{B.4}$$

Now for the second (ie. the ”middle”) term,

$$\frac{\partial}{\partial p_i}\left(\frac{\partial}{\partial p_j}\left(-2v^{th}v^{obs}\right)\right) = -2\frac{\partial}{\partial p_i}\left(\frac{\partial v^{th}}{\partial p_j}v^{obs} + v^{th}\frac{\partial v^{obs}}{\partial p_j}\right) \tag{B.5}$$

As before, the second term which contains the derivative of the constant velocities goes to zero,

$$\begin{aligned} -2\frac{\partial}{\partial p_i}\left(\frac{\partial v^{th}}{\partial p_j}v^{obs} + 0\right) =& -2\left(\frac{\partial^2 v^{th}}{\partial p_i \partial p_j}v^{obs} + \frac{\partial v^{th}}{\partial p_j}\frac{\partial v^{obs}}{\partial p_i}\right) \\ =& -2\frac{\partial^2 v^{th}}{\partial p_i \partial p_j}v^{obs} \end{aligned} \tag{B.6}$$

Combining these results and returning to the Fisher matrix,

$$\begin{aligned} F_{ij} &= \frac{1}{\sigma_v^2}\sum_n \frac{\partial v^{th}}{\partial p_i}\frac{\partial v^{th}}{\partial p_j} + v^{th}\frac{\partial^2 v^{th}}{\partial p_i \partial p_j} - \frac{\partial^2 v^{th}}{\partial p_i \partial p_j} v^{obs} \\ &= \frac{1}{\sigma_v^2}\sum_n \frac{\partial v^{th}}{\partial p_i}\frac{\partial v^{th}}{\partial p_j} + \frac{\partial^2 v^{th}}{\partial p_i \partial p_j}(v^{th} - v^{obs}) \end{aligned} \tag{B.7}$$

On average, given no systematic bias, the second term drops off and we're left with,

$$F_{ij} = \frac{1}{\sigma_v^2}\sum_n \frac{\partial v^{th}}{\partial p_i}\frac{\partial v^{th}}{\partial p_j} \tag{B.8}$$

APPENDIX C

Fisher matrix structure

In these sections we detail the structure of both the F_{ij} and F_{prior} matrices presented in Chapter V.

F_{ij} matrix structure

A schematic of the F_{ij} matrix and its submatrices is shown in Fig. C.1. As indicated by the figure, there are three main component submatrices to the F_{ij} matrix: the "cosmo-cosmo" submatrix (orange), the "cluster-cosmo" submatrices (red), and the "cluster-cluster" submatrices (green). The zeros indicate that the "off-diagonal" terms are nil. We describe the components of these submatrices in the following three subsections.

Cosmo-cosmo submatrix structure. In the top left of the matrix (see Fig. C.1) we have an N_{cosmo} by N_{cosmo} submatrix which is composed exclusively of the derivatives of our observable with respect to cosmological parameters. Let's consider the flat wCDM case, $p_{cosmo} \in \{\Omega_M, w, h\}$, and take a look at some terms. For this case, the first term in this submatrix is then,

$$F_{00} = \frac{1}{\sigma^2_{v_{esc}}} \sum_{n,k} \frac{\partial v_{esc}(z_n, r_k)}{\partial \Omega_M} \frac{\partial v_{esc}(z_n, r_k)}{\partial \Omega_M}. \tag{C.1}$$

The off-diagonal term in the first column second row is simply,

$$F_{01} = \frac{1}{\sigma^2_{v_{esc}}} \sum_{n,k} \frac{\partial v_{esc}(z_n, r_k)}{\partial \Omega_M} \frac{\partial v_{esc}(z_n, r_k)}{\partial w}. \tag{C.2}$$

Therefore, we are adding information on some cosmological parameter (or a combination, as in the off diagonal term) both across n clusters and k radial bins. As we

$$F_{ij} = \begin{pmatrix} \left[\text{cosmo - cosmo}\right] & \left[\text{cluster 1-cosmo}\right]^T & \dots & \left[\text{cluster N - cosmo}\right]^T \\ \left[\text{cluster 1 - cosmo}\right] & \left[\text{cluster 1- cluster 1}\right] & 0 & 0 \\ \vdots & 0 & \ddots & 0 \\ \left[\text{cluster N - cosmo}\right] & 0 & 0 & \left[\text{cluster N- cluster N}\right] \end{pmatrix}$$

Figure C.1: Structure of the $N_{dim} \times N_{dim}$ (see Eq. (4.19)) F_{ij} matrix. The "cosmo-cosmo" submatrix (orange) has dimensions $N_{cosmo} \times N_{cosmo}$ and contains the information solely of the cosmological parameters and their inverse covariances. The "cosmo-cluster" submatrices (red) lie along the first row and column of the F_{ij} matrix and are composed of the cross-correlated information between cluster parameters and cosmological parameters. Note that along the first column these submatrices have dimension $N_{clus} \times N_{cosmo}$, and along the first row, the matrices are transposed and therefore have dimensions $N_{cosmo} \times N_{clus}$. Lastly, the "cluster-cluster" submatrices (green) lie along the diagonal and have dimensions $N_{clus} \times N_{clus}$. Note that zeros populate the off-diagonal spaces given that there is no correlation between clusters, so that the derivatives cancel out.

detail in the next two sections, this is not the case for all other elements in the F_{ij} matrix.

Cosmo-cluster submatrices structure. Now let us take a look at the "cosmo-cluster" submatrices of Fig. C.1 (shown in red). Staying in the first row but now looking at the fourth column, we are now looking at the cross information attained from cosmology and cluster parameters. In this case, the anisotropy parameter for cluster 1 (β_1), the matrix element is,

$$\begin{aligned} F_{03} &= \frac{1}{\sigma^2_{v_{esc}}} \sum_{n,k} \frac{\partial v_{esc}(z_n, r_k)}{\partial \Omega_M} \frac{\partial v_{esc}(z_n, r_k)}{\partial \beta_1} \\ &= \frac{1}{\sigma^2_{v_{esc}}} \sum_{k} \frac{\partial v_{esc}(z_1, r_k)}{\partial \Omega_M} \frac{\partial v_{esc}(z_1, r_k)}{\partial \beta_1} + \\ &\quad \frac{1}{\sigma^2_{v_{esc}}} \sum_{k} \frac{\partial v_{esc}(z_2, r_k)}{\partial \Omega_M} \cancelto{0}{\frac{\partial v_{esc}(z_2, r_k)}{\partial \beta_1}} + \dots \end{aligned} \tag{C.3}$$

Immediately we notice that the second term of the second sum (i.e. the derivative with respect to β_1 for the second cluster z_2), is nil. Therefore, unlike the "cosmo-cosmo" submatrices, in these submatrices we only sum over the kth radial bin of the cluster corresponding to that column. This is the case for subsequent columns and rows (by symmetry). For instance, if $N_{cosmo} = 3$ then, F_{0j}, F_{1j}, F_{2j} where $j = \{3, 4, 5, \ldots, N_{dim}\}$. Symmetry yields the same for F_{i0}, F_{i1}, F_{i2} where $i = \{3, 4, 5, \ldots, N_{dim}\}$. The structure is the same for the "cluster-cosmo" submatrices along the first column, where the submatrices are simply transposed, as evoked by the superscript T in Fig. C.1.

Cluster-cluster submatrices structure. Lastly, let us now take a look at the "cluster-cluster" submatrices of Fig. C.1 (green). These submatrices express simply the covariance between cluster parameters for a given cluster. Taking a look at the first element of the first submatrix on the diagonal (the "cluster 1-cluster 1" submatrix of Fig. C.1),

$$
\begin{aligned}
F_{33} = \frac{1}{\sigma^2_{v_{esc}}} \sum_{n,k} \frac{\partial v_{esc}(z_n, r_k)}{\partial \beta_1} \frac{\partial v_{esc}(z_n, r_k)}{\partial \beta_1} \\
= \frac{1}{\sigma^2_{v_{esc}}} \sum_{k} \frac{\partial v_{esc}(z_1, r_k)}{\partial \beta_1} \frac{\partial v_{esc}(z_1, r_k)}{\partial \beta_1} + \\
\frac{1}{\sigma^2_{v_{esc}}} \sum_{k} \cancelto{0}{\frac{\partial v_{esc}(z_2, r_k)}{\partial \beta_1} \frac{\partial v_{esc}(z_2, r_k)}{\partial \beta_1}} + \ldots
\end{aligned}
\tag{C.4}
$$

We see that the second term and on will yield 0 given that they are the derivatives of clusters $z_{n \neq 1}$ with respect to β_1. This simply demonstrates that there is no cross correlation between clusters, as expected. Therefore, along the diagonal of F_{ij} we have 4×4 matrices of the various cluster parameters with respect to a given cluster, from cluster 1 to cluster N_{dim}.

Let us take a look now at some of the off diagonal submatrices, say between cluster 1 and cluster 2. The first element is,

$$
\begin{aligned}
F_{73} = \frac{1}{\sigma^2_{v_{esc}}} \sum_{n,k} \frac{\partial v_{esc}(z_n, r_k)}{\partial \beta_2} \frac{\partial v_{esc}(z_n, r_k)}{\partial \beta_1} \\
= \frac{1}{\sigma^2_{v_{esc}}} \sum_{k} \cancelto{0}{\frac{\partial v_{esc}(z_1, r_k)}{\partial \beta_2}} \frac{\partial v_{esc}(z_1, r_k)}{\partial \beta_1} + \\
\frac{1}{\sigma^2_{v_{esc}}} \sum_{k} \frac{\partial v_{esc}(z_2, r_k)}{\partial \beta_2} \cancelto{0}{\frac{\partial v_{esc}(z_2, r_k)}{\partial \beta_1}} + \ldots
\end{aligned}
\tag{C.5}
$$

Note that the first term in the sum over the radial bins of the first cluster ($n = 1$) is nil, and so is the second term of the sum over the radial bins of the second cluster ($n = 2$). By induction, all other terms are also nil. Therefore, these off diagonal terms are all zero given that there is no cross correlation between cluster parameters of different clusters. All of these terms are aptly represented by "0"'s in Fig. C.1.

F_{prior} matrix sub-structure

In this section we describe the structure of the prior matrix found in Eq. (4.16). In particular, we focus on the structure of the submatrix elements of the F_{prior} matrix in Eq. (4.22). The covariance submatrices that lie along the diagonal of Eq. (4.22) are given by,

$$C_{cluster} = \begin{bmatrix} \sigma_\beta^2 & 0 & 0 & 0 \\ 0 & \sigma_\alpha^2 & 0 & 0 \\ 0 & 0 & \sigma_{r_{-2}}^2 & -0.7\sigma_{\rho_{-2}}\sigma_{r_{-2}} \\ 0 & 0 & -0.7\sigma_{\rho_{-2}}\sigma_{r_{-2}} & \sigma_{\rho_{-2}}^2 \end{bmatrix}. \tag{C.6}$$

Note that the only non-zero terms off the diagonal is the covariance between r_{-2} and ρ_{-2}. Specific values for these matrix elements and the code used to produce the matrices from which we derive the constraints on cosmological parameters can be found online at `https://github.com/alejostark/phase_space_cosmo_fisher`.

APPENDIX D

Weak lensing mass covariance with cosmology

In this section, we consider how uncertainties in the cosmological parameters affect the weak lensing mass uncertainties, which, recall, are in turn featured in our prior information matrix $C_{cluster}$ (see Chapter V).

To do this, we carry out a quantitative investigation utilizing the Cluster-Lensing code of Ford (2016). We start out by building a $\Sigma(r)$ surface density shear profile for one fiducial cluster with $M_{200} = 4 \times 10^{14} M_{\odot}$. We first create this profile assuming fixed, fiducial values of the cosmological parameters. We assume the profile has Gaussian errors of such size to ensure that we recover a 20% statistical error on the cluster mass after performing a simple χ^2 analysis.

We then allow the cosmological parameters to vary, and conduct a Markov Chain Monte Carlo (MCMC) analysis with *emcee* to sample the posterior distribution and examine the likelihood of the inferred mass M_{200} Foreman-Mackey et al. (2013). The likelihood model is given by

$$\ln \mathcal{L}(\Sigma | r_k, z, \Theta) = -\frac{1}{2} \sum_k \frac{\Big(\Sigma(r_k, z, \Theta_{fid}) - \Sigma(r_k, z, \Theta) \Big)^2}{\sigma_\Sigma^2}. \tag{D.1}$$

Assuming the flat wCDM model, our parameter set is given by $\Theta = \{\Omega_M, w, h, M_{200}\}$. Note that the cluster profile information is reduced to a single parameter, M_{200}, because the Cluster-Lensing code uses a mass-concentration relation to create the $\Sigma(r)$ profile Ford (2016). For a single mock $\Sigma(r)$ profile, after marginalizing over all other parameters we find that the total error in the cluster mass scale increases from 20% to 40%. That is, if cosmological parameters are allowed to vary, the weak lensing

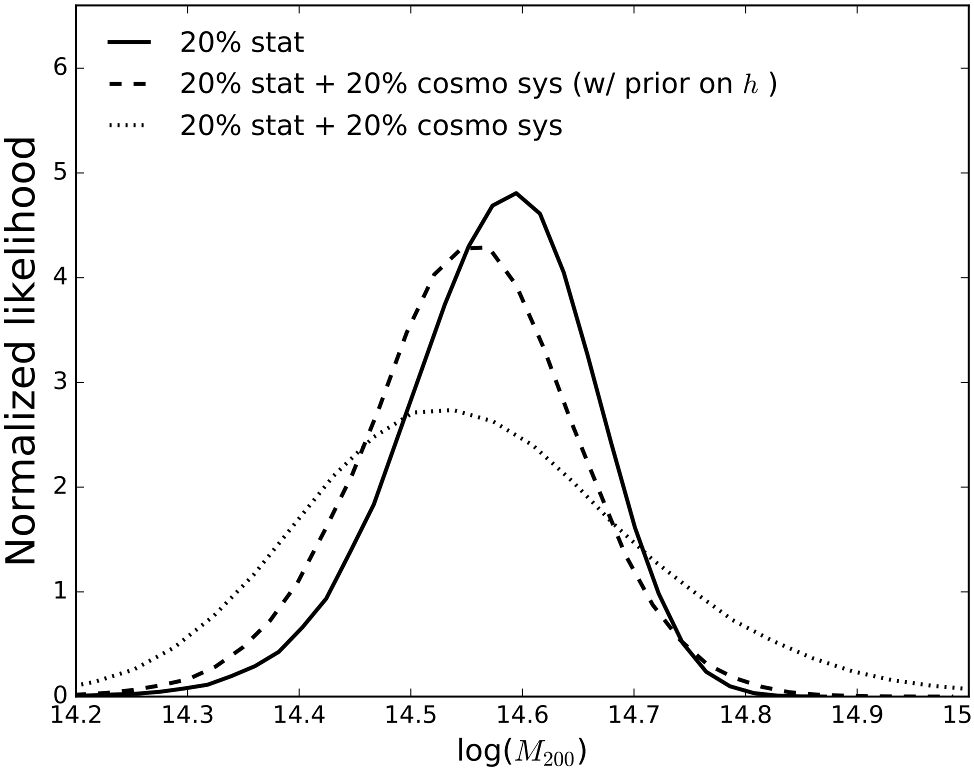

Figure D.1: Marginalized likelihood of the inferred mass of our fiducial cluster ($M_{200} = 4 \times 10^{14} M_\odot$) from the weak lensing surface density shear profile $\Sigma(r)$. The total uncertainty in the inferred mass increases by a factor of ~ 2 if no prior on the cosmological parameters is introduced; however, a reasonable prior on the Hubble parameter h from Riess et al. (2016) recovers most of the lost information on M_{200}.

mass error increases by a factor of two. We confirm this using statistical errors of 5% and also 40%.

We show the marginalized posterior likelihood in Fig. D.1. Three different prior likelihoods are shown: a strong prior, basically fixing cosmology (represented by the solid black line), a prior only on h (dashed line), and no prior (dotted line). Note how the 20% systematic error likelihood is broadened if cosmological parameters are allowed to vary, but that we can almost totally reduce the cosmological systematic error simply by applying a reasonable prior on the Hubble parameter of Riess et al. (2016) ($\sigma_h = 0.0174$). We tabulate the resulting uncertainties in the Einasto cluster parameters in Table 4.1. As stated in the previous subsection, the code used to produce these results can be found online. Lastly, we note that since the bias in the recovered mass (dotted and dashed) is small, and we do not factor it into our analysis.

BIBLIOGRAPHY

BIBLIOGRAPHY

Aguerri, J. A. L., Agulli, I., Diaferio, A., & Dalla Vecchia, C. 2017, MNRAS, 468, 364

Agulli, I., Aguerri, J. A. L., Sánchez-Janssen, R., et al. 2016, MNRAS, 458, 1590

Albrecht, A., Bernstein, G., Cahn, R., et al. 2006, ArXiv Astrophysics e-prints, astro-ph/0609591

Andreon, S., & Hurn, M. A. 2010, Monthly Notices of the Royal Astronomical Society, 404, 1922

Annunziatella, M., Mercurio, A., Biviano, A., et al. 2016, A&A, 585, A160

Applegate, D. E., von der Linden, A., Kelly, P. L., et al. 2014a, MNRAS, 439, 48

—. 2014b, MNRAS, 439, 48

Arnold, C., Puchwein, E., & Springel, V. 2014, MNRAS, 440, 833

Bayliss, M. B., Zengo, K., Ruel, J., et al. 2017, ApJ, 837, 88

Becker, M. R., & Kravtsov, A. V. 2011a, ApJ, 740, 25

—. 2011b, ApJ, 740, 25

Becker, M. R., & Kravtsov, A. V. 2011, The Astrophysical Journal, 740, 25

Becker, M. R., McKay, T. A., Koester, B., et al. 2007, ApJ, 669, 905

Behroozi, P. S., Loeb, A., & Wechsler, R. H. 2013, J. Cosmology Astropart. Phys., 6, 019

Benatov, L., Rines, K., Natarajan, P., Kravtsov, A., & Nagai, D. 2006, MNRAS, 370, 427

Bertschinger, E. 1985, ApJS, 58, 39

Betoule, M., Kessler, R., Guy, J., et al. 2014, A&A, 568, A22

Binney, J., & Mamon, G. A. 1982, MNRAS, 200, 361

Binney, J., & Tremaine, S. 1987, Galactic dynamics

Biviano, A., & Katgert, P. 2004, A&A, 424, 779

Biviano, A., Rosati, P., Balestra, I., et al. 2013, A&A, 558, A1

Bloomfield, J., anna . Flanagan, Park, M., & Watson, S. 2013, Journal of Cosmology and Astroparticle Physics, 2013, 010

Bolton, A. S., Schlegel, D. J., Aubourg, É., et al. 2012, AJ, 144, 144

Busha, M. T., Adams, F. C., Wechsler, R. H., & Evrard, A. E. 2003, ApJ, 596, 713

Caldwell, R. R. 2002, Physics Letters B, 545, 23

Carlberg, R. G., Yee, H. K. C., Ellingson, E., et al. 1997, ApJ, 485, L13

Cataneo, M., Rapetti, D., Schmidt, F., et al. 2015, Phys. Rev. D, 92, 044009

Chevallier, M., & Polarski, D. 2001, International Journal of Modern Physics D, 10, 213

Clowe, D., Luppino, G. A., Kaiser, N., & Gioia, I. M. 2000, ApJ, 539, 540

Coe, D. 2009, ArXiv e-prints, arXiv:0906.4123

Creminelli, P., D'Amico, G., Norea, J., & Vernizzi, F. 2009, Journal of Cosmology and Astroparticle Physics, 2009, 018

Cypriano, E. S., Sodré, Jr., L., Kneib, J.-P., & Campusano, L. E. 2004, ApJ, 613, 95

Dehnen, W. 1993, MNRAS, 265, 250

Demarco, R., Gobat, R., Rosati, P., et al. 2010, ApJ, 725, 1252

DESI Collaboration, Aghamousa, A., Aguilar, J., et al. 2016, ArXiv e-prints, arXiv:1611.00037

Diaferio, A. 1999, MNRAS, 309, 610

Diaferio, A. 1999, Monthly Notices of the Royal Astronomical Society, 309, 610

Diaferio, A., & Geller, M. J. 1997a, ApJ, 481, 633

—. 1997b, ApJ, 481, 633

Diaferio, A., & Geller, M. J. 1997, The Astrophysical Journal, 481, 633

Diehl, H. T., Abbott, T. M. C., Annis, J., et al. 2014, in Proc. SPIE, Vol. 9149, Observatory Operations: Strategies, Processes, and Systems V, 91490V

Diemer, B., & Kravtsov, A. V. 2014, ApJ, 789, 1

—. 2015, ApJ, 799, 108

Duffy, A. R., Schaye, J., Kay, S. T., & Dalla Vecchia, C. 2008, MNRAS, 390, L64

Duffy, A. R., Schaye, J., Kay, S. T., & Dalla Vecchia, C. 2008, Monthly Notices of the Royal Astronomical Society: Letters, 390, L64

Durrer, R., & Maartens, R. 2008, ArXiv e-prints, arXiv:0811.4132

Edwards, L. O. V., & Fadda, D. 2011, AJ, 142, 148

Einasto, J. 1965, Trudy Astrofizicheskogo Instituta Alma-Ata, 5, 87

Ellingson, E., Yee, H. K. C., Abraham, R. G., et al. 1997, ApJS, 113, 1

Evrard, A. E. 1986, ApJ, 310, 1

Evrard, A. E., Bialek, J., Busha, M., et al. 2008, ApJ, 672, 122

Falck, B., Koyama, K., bo Zhao, G., & Li, B. 2014, Journal of Cosmology and Astroparticle Physics, 2014, 058

Falco, M., Hansen, S. H., Wojtak, R., & Mamon, G. A. 2013, MNRAS, 431, L6

Faltenbacher, A., Kravtsov, A. V., Nagai, D., & Gottlöber, S. 2005, MNRAS, 358, 139

Farahi, A., Evrard, A. E., Rozo, E., Rykoff, E. S., & Wechsler, R. H. 2016, MNRAS, 460, 3900

Fillmore, J. A., & Goldreich, P. 1984, ApJ, 281, 1

Foëx, G., Soucail, G., Pointecouteau, E., et al. 2012, A&A, 546, A106

Ford, J. 2016, cluster-lensing: v0.1.2, doi:10.5281/zenodo.51370

Foreman-Mackey, D., Hogg, D. W., Lang, D., & Goodman, J. 2013, PASP, 125, 306

Gavazzi, R., Adami, C., Durret, F., et al. 2009, A&A, 498, L33

Geller, M. J., Diaferio, A., Rines, K. J., & Serra, A. L. 2013, ApJ, 764, 58

Geller, M. J., Hwang, H. S., Diaferio, A., et al. 2014, ApJ, 783, 52

Geller, M. J., Hwang, H. S., Diaferio, A., et al. 2014, The Astrophysical Journal, 783, 52

Gifford, D., Kern, N., & Miller, C. J. 2017, ApJ, 834, 204

Gifford, D., Miller, C., & Kern, N. 2013, ApJ, 773, 116

Gifford, D., & Miller, C. J. 2013, ApJ, 768, L32

Gifford, D., & Miller, C. J. 2013a, The Astrophysical Journal Letters, 768, L32

—. 2013b, The Astrophysical Journal Letters, 768, L32

Girardi, M., Barrena, R., Boschin, W., & Ellingson, E. 2008, A&A, 491, 379

Girardi, M., Mercurio, A., Balestra, I., et al. 2015, A&A, 579, A4

Gunn, J. E., & Gott, III, J. R. 1972, ApJ, 176, 1

Guo, Q., White, S., Boylan-Kolchin, M., et al. 2011a, MNRAS, 413, 101

—. 2011b, MNRAS, 413, 101

Hansen, S. H. 2009, The Astrophysical Journal, 694, 1250

Heavens, A. 2016, Entropy, 18, 236

Hellwing, W. A., Barreira, A., Frenk, C. S., Li, B., & Cole, S. 2014, Phys. Rev. Lett., 112, 221102

Henriques, B. M. B., White, S. D. M., Lemson, G., et al. 2012, MNRAS, 421, 2904

High, F. W., Stalder, B., Song, J., et al. 2010, ApJ, 723, 1736

Hoekstra, H., Herbonnet, R., Muzzin, A., et al. 2015, MNRAS, 449, 685

Hoekstra, H., Mahdavi, A., Babul, A., & Bildfell, C. 2012, Monthly Notices of the Royal Astronomical Society, 427, 1298

Holz, D. E., & Perlmutter, S. 2012, ApJ, 755, L36

Host, O., Hansen, S. H., Piffaretti, R., et al. 2009, ApJ, 690, 358

Hu, W., & Sawicki, I. 2007, Phys. Rev. D, 76, 064004

Huterer, D., & Turner, M. S. 2001, Phys. Rev. D, 64, 123527

Hwang, H. S., & Lee, M. G. 2008, ApJ, 676, 218

Iannuzzi, F., & Dolag, K. 2012, MNRAS, 427, 1024

Jee, M. J., Dawson, K. S., Hoekstra, H., et al. 2011, ApJ, 737, 59

Joyce, A., Jain, B., Khoury, J., & Trodden, M. 2015, Phys. Rep., 568, 1

Joyce, A., Jain, B., Khoury, J., & Trodden, M. 2015, Physics Reports, 568, 1 , beyond the cosmological standard model

Joyce, A., Lombriser, L., & Schmidt, F. 2016, ArXiv e-prints, arXiv:1601.06133

Kaiser, N. 1986, MNRAS, 222, 323

Khoury, J., & Weltman, A. 2004a, Phys. Rev. D, 69, 044026

—. 2004b, Phys. Rev. Lett., 93, 171104

Kim, A. G., Linder, E. V., Edelstein, J., & Erskine, D. 2015, Astroparticle Physics, 62, 195

Knollmann, S. R., & Knebe, A. 2009, The Astrophysical Journal Supplement Series, 182, 608

Koyama, K. 2016, Reports on Progress in Physics, 79, 046902

Koyama, K. 2016, Reports on Progress in Physics, 79, 046902

Kravtsov, A. V., & Borgani, S. 2012a, ARA&A, 50, 353

—. 2012b, ARA&A, 50, 353

Lam, T. Y., Nishimichi, T., Schmidt, F., & Takada, M. 2012, Phys. Rev. Lett., 109, 051301

Lemze, D., Broadhurst, T., Rephaeli, Y., Barkana, R., & Umetsu, K. 2009, ApJ, 701, 1336

Lemze, D., Wagner, R., Rephaeli, Y., et al. 2012, ApJ, 752, 141

Lemze, D., Postman, M., Genel, S., et al. 2013, ApJ, 776, 91

Li, B., Zhao, G.-B., Teyssier, R., & Koyama, K. 2012, Journal of Cosmology and Astroparticle Physics, 2012, 051

Linder, E. V. 2003, Physical Review Letters, 90, 091301

Llinares, C., & Mota, D. F. 2013, Phys. Rev. Lett., 110, 161101

Łokas, E. L., & Mamon, G. A. 2001, Monthly Notices of the Royal Astronomical Society, 321, 155

Łokas, E. L., Wojtak, R., Gottlöber, S., Mamon, G. A., & Prada, F. 2006, MNRAS, 367, 1463

Lombriser, L., Koyama, K., Zhao, G.-B., & Li, B. 2012a, Phys. Rev. D, 85, 124054

Lombriser, L., Schmidt, F., Baldauf, T., et al. 2012b, Phys. Rev. D, 85, 102001

Lombriser, L., & Taylor, A. 2015, Phys. Rev. Lett., 114, 031101

Mateo, M., Bailey, J. I., Crane, J., et al. 2012, in Proc. SPIE, Vol. 8446, Ground-based and Airborne Instrumentation for Astronomy IV, 84464Y

Maurogordato, S., Cappi, A., Ferrari, C., et al. 2008, A&A, 481, 593

Medezinski, E., Umetsu, K., Okabe, N., et al. 2016, ApJ, 817, 24

Melchior, P., Gruen, D., McClintock, T., et al. 2016, ArXiv e-prints, arXiv:1610.06890

Merritt, D. 1987, ApJ, 313, 121

Miller, C. J., Stark, A., Gifford, D., & Kern, N. 2016, ApJ, 822, 41

Miller, C. J., Nichol, R. C., Reichart, D., et al. 2005, AJ, 130, 968

Miller, N. A., Oegerle, W. R., & Hill, J. M. 2006, AJ, 131, 2426

Moran, S. M., Ellis, R. S., Treu, T., et al. 2007, ApJ, 671, 1503

More, S., Diemer, B., & Kravtsov, A. V. 2015, ApJ, 810, 36

More, S., Miyatake, H., Takada, M., et al. 2016, ApJ, 825, 39

Munari, E., Biviano, A., Borgani, S., Murante, G., & Fabjan, D. 2013, MNRAS, 430, 2638

Munari, E., Biviano, A., & Mamon, G. A. 2014, A&A, 566, A68

Nandra, R., Lasenby, A. N., & Hobson, M. P. 2012a, MNRAS, 422, 2931

—. 2012b, MNRAS, 422, 2931

Natarajan, P., & Kneib, J.-P. 1997, MNRAS, 287, 833

Navarro, J. F., Frenk, C. S., & White, S. D. M. 1996, ApJ, 462, 563

—. 1997, ApJ, 490, 493

Navarro, J. F., Frenk, C. S., & White, S. D. M. 1997, The Astrophysical Journal, 490, 493

Ochsenbein, F., Bauer, P., & Marcout, J. 2000, A&AS, 143, 23

Oemler, Jr., A., Dressler, A., Kelson, D., et al. 2009, ApJ, 693, 152

Okabe, N., & Smith, G. P. 2015, ArXiv e-prints, arXiv:1507.04493

Okabe, N., Takada, M., Umetsu, K., Futamase, T., & Smith, G. P. 2010, PASJ, 62, 811

Okabe, N., & Umetsu, K. 2008, PASJ, 60, 345

Owers, M. S., Nulsen, P. E. J., & Couch, W. J. 2011a, ApJ, 741, 122

—. 2011b, ApJ, 741, 122

Owers, M. S., Randall, S. W., Nulsen, P. E. J., et al. 2011c, ApJ, 728, 27

Pedersen, K., & Dahle, H. 2007, ApJ, 667, 26

Perlmutter, S., Aldering, G., Goldhaber, G., et al. 1999, ApJ, 517, 565

Planck Collaboration, Ade, P. A. R., Aghanim, N., et al. 2016a, A&A, 594, A13

—. 2016b, A&A, 594, A13

Regoes, E. 1996, A&A, 308, 368

Regoes, E., & Geller, M. J. 1989a, AJ, 98, 755

—. 1989b, AJ, 98, 755

Retana-Montenegro, E., van Hese, E., Gentile, G., Baes, M., & Frutos-Alfaro, F. 2012, A&A, 540, A70

Riess, A. G., Filippenko, A. V., Challis, P., et al. 1998, AJ, 116, 1009

Riess, A. G., Strolger, L.-G., Casertano, S., et al. 2007, ApJ, 659, 98

Riess, A. G., Macri, L. M., Hoffmann, S. L., et al. 2016, ApJ, 826, 56

Rines, K., Diaferio, A., & Natarajan, P. 2008, ApJ, 679, L1

Rines, K., Geller, M. J., Diaferio, A., & Kurtz, M. J. 2013, ApJ, 767, 15

Rines, K., Geller, M. J., Diaferio, A., & Kurtz, M. J. 2013, The Astrophysical Journal, 767, 15

Rines, K., Geller, M. J., Kurtz, M. J., & Diaferio, A. 2003, AJ, 126, 2152

Rines, K. J., Geller, M. J., Diaferio, A., Hwang, H. S., & Sohn, J. 2017, ArXiv e-prints, arXiv:1712.00212

Rozo, E., Wu, H.-Y., & Schmidt, F. 2011, ApJ, 735, 118

Rozo, E., Wechsler, R. H., Rykoff, E. S., et al. 2010, ApJ, 708, 645

Rykoff, E. S., Rozo, E., Busha, M. T., et al. 2014, ApJ, 785, 104

Sánchez-Portal, M., Pintos-Castro, I., Pérez-Martínez, R., et al. 2015, A&A, 578, A30

Saro, A., Mohr, J. J., Bazin, G., & Dolag, K. 2013, ApJ, 772, 47

Schmidt, F. 2010, Phys. Rev. D, 81, 103002

Schmidt, F., Vikhlinin, A., & Hu, W. 2009, Phys. Rev. D, 80, 083505

Sereno, M. 2015, MNRAS, 450, 3665

Sereno, M., Fedeli, C., & Moscardini, L. 2016a, J. Cosmology Astropart. Phys., 1, 042

—. 2016b, J. Cosmology Astropart. Phys., 1, 042

Serra, A. L., Diaferio, A., Murante, G., & Borgani, S. 2011, MNRAS, 412, 800

Shapiro, C., & Turner, M. S. 2006, The Astrophysical Journal, 649, 563

Shectman, S. A. 1982, ApJ, 262, 9

Smail, I., Ellis, R. S., Dressler, A., et al. 1997, ApJ, 479, 70

Solanes, J. M., & Salvador-Sole, E. 1990, A&A, 234, 93

Springel, V., White, S. D. M., Jenkins, A., et al. 2005a, Nature, 435, 629

—. 2005b, Nature, 435, 629

Stark, A., Miller, C. J., & Gifford, D. 2016, ApJ, 830, 109

Stark, A., Miller, C. J., & Halenka, V. 2017, ArXiv e-prints, arXiv:1711.10018

Stark, A., Miller, C. J., & Huterer, D. 2017, Phys. Rev. D, 96, 023543

Stark, A., Miller, C. J., Kern, N., et al. 2016, Phys. Rev. D, 93, 084036

Svensmark, J., Wojtak, R., & Hansen, S. H. 2015, Monthly Notices of the Royal Astronomical Society, 448, 1644

Takada, M., Ellis, R. S., Chiba, M., et al. 2014, PASJ, 66, R1

Tegmark, M., Taylor, A. N., & Heavens, A. F. 1997, ApJ, 480, 22

Terukina, A., Lombriser, L., Yamamoto, K., et al. 2014, Journal of Cosmology and Astroparticle Physics, 2014, 013

Tinker, J., Kravtsov, A. V., Klypin, A., et al. 2008, ApJ, 688, 709

Tran, K.-V. H., Franx, M., Illingworth, G. D., et al. 2007, ApJ, 661, 750

Tsujikawa, S. 2013, Classical and Quantum Gravity, 30, 214003

Tyler, K. D., Rieke, G. H., & Bai, L. 2013, ApJ, 773, 86

Umetsu, K., Medezinski, E., Nonino, M., et al. 2012, ApJ, 755, 56

—. 2014, ApJ, 795, 163

Umetsu, K., Sereno, M., Medezinski, E., et al. 2015, ApJ, 806, 207

Vikhlinin, A., Kravtsov, A. V., Burenin, R. A., et al. 2009, ApJ, 692, 1060

Weinberg, D. H., Mortonson, M. J., Eisenstein, D. J., et al. 2013, Physics Reports, 530, 87 , observational Probes of Cosmic Acceleration

Weinberg, D. H., Mortonson, M. J., Eisenstein, D. J., et al. 2013, Phys. Rep., 530, 87

Wilcox, H., Bacon, D., Nichol, R. C., et al. 2015, Monthly Notices of the Royal Astronomical Society, 452, 1171

Wojtak, R., Hansen, S. H., & Hjorth, J. 2011, Nature, 477, 567

Wojtak, R., & Łokas, E. L. 2010, MNRAS, 408, 2442

Wu, H.-Y., Hahn, O., Evrard, A. E., Wechsler, R. H., & Dolag, K. 2013, MNRAS, 436, 460

Xu, L. 2015, Phys. Rev. D, 91, 063008

Zhao, G.-B., Li, B., & Koyama, K. 2011a, Phys. Rev. D, 83, 044007

—. 2011b, Phys. Rev. Lett., 107, 071303

Zitrin, A., Rosati, P., Nonino, M., et al. 2012, ApJ, 749, 97

Zu, Y., Weinberg, D. H., Jennings, E., Li, B., & Wyman, M. 2014, MNRAS, 445, 1885

Zwicky, F. 1937, ApJ, 86, 217